

Chapter

5 Modelling of the $XY\theta_Z$ micro-motion stage

In Chapter 4 three modelling methods, the 2-D FEM, SCHM and PRBM, were presented and used to derive kinematic and dynamic models of the 3RRR compliant mechanism. In this chapter the 3RRR compliant mechanism models are combined with a linear piezo-actuator model to give complete $XY\theta_Z$ micro-motion stage models. The workspace, static-coupling and natural frequency predicted by the models is then presented.

5.1 Piezo-actuator behaviour

When a voltage is applied to a piezo-actuator it generates displacement and/or force. If no external force is applied to the piezo-actuator a maximum displacement is achieved when the maximum voltage is applied. Figure 5-1 shows the relationship between displacement and voltage for the piezo-actuator used in this study when there is no external force. If the piezo-actuator is restrained in an infinitely rigid restraint so that no displacement is possible then a maximum force, the blocked force, is achieved when the maximum voltage is applied. The operational region of the piezo-actuator is the achievable combination of displacement and force that can occur between these two extremes. The force vs. displacement characteristics for the

piezo-actuator used in this study are shown in Figure 5-2. The top portion of Figure 5-2 shows the maximum boundary of the operational region, which occurs when the applied voltage is 150V. The operational region is the area under this curve.

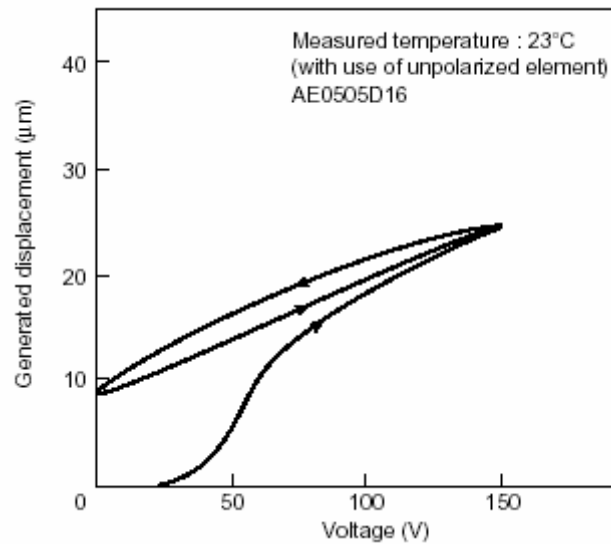


Figure 5-1 - Generated displacement vs. applied voltage characteristics for Tonkin AE0505D16 stack piezo-actuator [Tonkin, 2001].

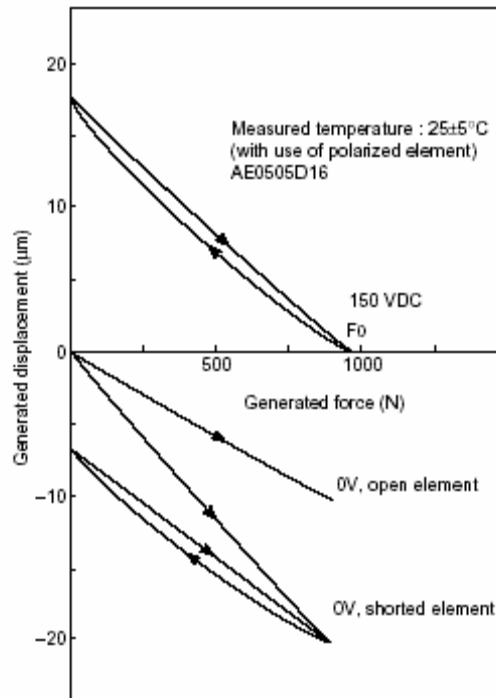


Figure 5-2 - Generated force vs. generated displacement characteristics for Tonkin AE0505D16 stack piezo-actuator [Tonkin, 2001].

It can be observed from Figures 5-1 and 5-2 that the piezo-actuator displays non-linear hysteresis behaviour. It also displays non-linear creep behaviour.

5.1.1 Piezo-actuator stiffness

For most materials the stiffness depends on the Young's modulus of the material and is expressed in terms of the spring constant, k_T , which is defined by equation (5.1).

$$k_T = F / \Delta L \quad (5.1)$$

However, for piezo-actuators this simple definition has limited application. The stiffness of the piezo-actuator depends on the operating state. Static, dynamic, large-

The Modelling and Optimal Design of a 3-DOF XYθ_Z Micro-Motion Stage

signal and small-signal operation with shorted and open electrodes, all have different stiffness. This can be observed in the lower portion of Figure 5-2. This is due to the polarisation of the piezo-ceramic. The poling process leaves the ceramic with a remnant strain, which is affected by the magnitude of polarisation. The polarisation is affected by both the applied voltage and the external force. When an external force is applied to the piezo-ceramic its displacement depends on both its stiffness and the change in remnant strain. Equation (5.1) is valid only for small forces and small-signal conditions.

5.2 Linear piezo-actuator model

The non-linear behaviour of the piezo-actuator does not have a very significant impact on stage performance characteristics such as workspace size, natural frequency and coupling. Therefore, it is proposed that a linear model be used to give a first approximation of the piezo-actuator behaviour. Thus, the non-linear hysteresis and creep will be ignored in the $XY\theta_z$ micro-motion stage model. This type of linear modelling approach has been previously applied with success [Chang et al., 1999] [Goldfarb and Celanovic, 1999]. In this approach the piezo-actuator is modelled as a simple mass-spring-damper system. This type of model is shown schematically in Figure 5-3.

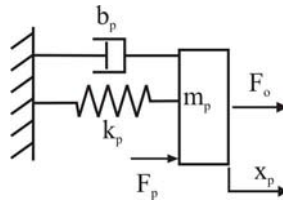


Figure 5-3 - Linear dynamic model of a piezo-actuator.

The quasi-static relationship between displacement and force has also been approximated by a linear relationship [Goldfarb and Celanovic,1999]. The approximate linear static relationship between piezo-actuator displacement, x_p , stiffness, k_p , and output force, F_o , is shown schematically in Figure 5-4. This figure also shows the linear approximation of the operational region of the piezo-actuator.

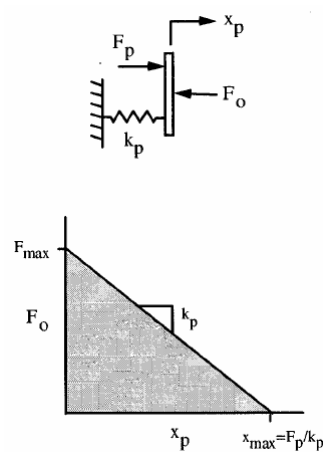


Figure 5-4 - (top) Quasi-static model of stack piezo-actuator and (bottom) region of operation [Goldfarb and Celanovic,1999].

When coupled to a compliant mechanism the piezo-actuator experiences a spring load, K_s , that affects the operational region of the piezo-actuator, by reducing its displacement as shown in Figure 5-5.

NOTE: This figure is included on page 142 of the print copy of the thesis held in the University of Adelaide Library.

Figure 5-5 - Schematic showing the effect on piezo-actuator displacement of a spring load [Physik Instrumente, 2006].

Equation (5.2) [Physik Instrumente, 2006] can be used to approximately determine the displacement of the loaded piezo-actuator, ΔL_{load} , given its displacement when no-load is applied, $\Delta L_{no-load}$, its stiffness, k_p and the spring load from the compliant mechanism, K_s .

$$\Delta L_{load} \approx \Delta L_{no-load} \left(\frac{k_p}{k_p + K_s} \right) \quad (5.2)$$

This effect on piezo-actuator displacement has a significant effect on the XYθ_z stage kinematic behaviour. Therefore, equation (5.2) has been incorporated into the micromotion stage model to give a more accurate prediction of the achievable displacement of the stage. The value of k_p used in the XYθ_z stage model will be calculated from the Young's modulus of the piezo-ceramic provided by Tonkin (2001).

The properties of the piezo-actuator used in this study are given in Table 5-1.

Material Properties for Tonkin AE0505D16 Piezo-actuator	
Un-loaded displacement ($\Delta L_{no-load}$) @100V	11.6±2.0μm
Length	20mm
Cross-section	5x5mm
Young's Modulus	4.4e10 N/μm
Stiffness, k_p	55N/μm

Table 5-1- Properties of the piezo-actuator used in this study.

5.2.1 Incorporating the piezo-actuator model into the 3RRR compliant mechanism model

The piezo-actuator is incorporated into the 3RRR compliant mechanism as shown in Figure 5-6. The piezo-actuator is modelled as a linear spring fixed at one end to a rigid support and at the other end attached to the compliant mechanism via a rotational joint. The maximum displacement of the piezo-actuator is determined from equation (5.2). The mass of the piezo-actuator is relatively small compared to the mass of the 3RRR compliant mechanism and end-effector, and therefore this will be ignored in the model. The spring load acting on the piezo-actuator is provided by the stiffness of the compliant mechanism at the point of contact with the piezo-actuator, which is denoted by k_{in} . The output force of the piezo-actuator, F_o , is equivalent to the input force acting on the compliant mechanism at the point of piezo-actuator contact, F_{in} . In this model the displacement of the input-links, ΔD_i ($i=1,2,3$), is assumed equal to the elongation of the piezo-actuators, ΔL_i .

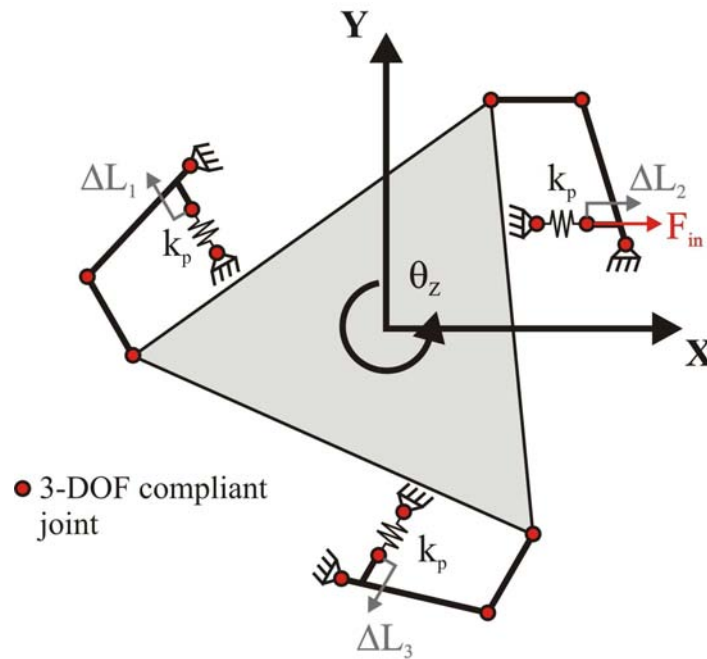


Figure 5-6 - Schematic of 3RRR compliant mechanism and linear piezo-actuator model.

5.2.2 Limitations of this modelling Approach

It is recognised that this modelling approach does not accurately model the interface between the piezo-actuator and the compliant mechanism. The interface will depend on the type of actuator used and the method of assembly. For the prototypes considered in this thesis the piezo-actuator is held in the compliant mechanism via a preload compression force. This means that the piezo-actuator can only apply a pushing force on the compliant mechanism, but not a pulling force. Therefore there is nonlinearity in the interface between the piezo-actuator and compliant mechanism. This nonlinearity may affect the dynamic modelling of the stage. However, the ANSYS modal analysis routine uses a linear method and ignores any non-linear behaviour, and therefore this can not be taken into consideration when calculating the natural frequency.

5.2.3 Stiffness of the 3RRR compliant mechanism and piezo-actuator displacement under load

The stiffness of the 3RRR compliant mechanism predicted by the 2-D FEM, SCHM and PRBM was presented in Chapter 4. Table 4-14 gave the stiffness at the point of actuator input, k_{in} . These results are given again in Table 5-2.

Using these values of k_{in} and equation (5.2), the piezo-actuator displacements under load are predicted, as given in Table 5-2. As the 3RRR compliant mechanism model is symmetrical and the same model piezo-actuators are used, for each model all three piezo-actuators will have the same maximum displacement $\Delta L_{max,load}$.

3RRR Model	2-D FEM	SCHM	PRBM
k_{in} (N/m)	1.58e7	2.04e7	3.08e7
k_p (N/m)	55e6	55e6	55e6
$\Delta L_{max,no-load}$ (μm)	11.6	11.6	11.6
$\Delta L_{max,load}$ (μm)	9.0	8.5	7.4

Table 5-2 -Stiffness of the 3RRR compliant mechanism at the point of piezo-actuator input predicted by the 2-D FEM, SCHM and PRBM and the displacement under load of the piezo-actuator.

5.3 Workspace of $XY\theta_Z$ micro-motion stage

The workspace area of a $XY\theta_Z$ micro-motion stage using the 3RRR compliant mechanism has been presented previously in [Handley, 2004]. A more thorough investigation of the workspace will be presented in this section.

The end-effector workspace of the $XY\theta_z$ micro-motion stage is dependent upon both the 3RRR compliant mechanism Jacobian and the piezo-actuator displacement under load. In these models, it is assumed that all the piezo-actuator elongation is transferred to the compliant mechanism input-links and thus ΔD equals ΔL . Using equation (5.3) a point in the workspace can be determined for any given combination of piezo-actuator input displacements. The origin of the workspace is the point corresponding to zero input from all three actuators.

$$\begin{bmatrix} X \\ Y \\ \theta_z \end{bmatrix} = \begin{bmatrix} J_{11} & J_{12} & J_{13} \\ J_{21} & J_{22} & J_{23} \\ J_{31} & J_{32} & J_{33} \end{bmatrix} \begin{bmatrix} \Delta L_1 \\ \Delta L_2 \\ \Delta L_3 \end{bmatrix} \quad (5.3)$$

Each point in the workspace is defined by an X, Y axis coordinate and a rotation, θ_z .

The Jacobian for the first prototype 3RRR compliant mechanism was predicted by the 2-D FEM, SCHM and PRBM in Chapter 4. The Jacobians are given again in Table 5-3.

2-D FEM			SCHM			PRBM		
-1.13	2.27	-1.14	-1.15	2.31	-1.16	-1.61	3.22	-1.61
1.97	-0.01	-1.96	2.01	-0.01	-2.00	2.79	0.00	-2.79
-41.69	-41.80	-41.77	-42.77	-42.52	-42.78	-59.69	-59.66	-59.69

Table 5-3 - Jacobians for the prototype-one 3RRR compliant mechanism predicted by the 2-D FEM, SCHM and PRBM.

5.3.1 Reachable workspace

The reachable workspace of the $XY\theta_Z$ micro-motion stage contains all points that can be reached by the end-effector when the piezo-actuators displace through their maximum range, from 0 to $\Delta L_{\max,load}$.

By using equation (5.3) and applying all combinations of the extreme piezo-actuator input displacements, as given in Table 5-4, the eight vertices describing the extremities of the reachable workspace can be determined.

Vertex Number	Piezo-Actuator Input Displacement		
	ΔL_1	ΔL_2	ΔL_3
1	0	0	0
2	0	0	$\Delta L_{\max,load}$
3	0	$\Delta L_{\max,load}$	0
4	0	$\Delta L_{\max,load}$	$\Delta L_{\max,load}$
5	$\Delta L_{\max,load}$	0	0
6	$\Delta L_{\max,load}$	0	$\Delta L_{\max,load}$
7	$\Delta L_{\max,load}$	$\Delta L_{\max,load}$	0
8	$\Delta L_{\max,load}$	$\Delta L_{\max,load}$	$\Delta L_{\max,load}$

Table 5-4 - Input displacement of piezo-actuators to give vertices of workspace.

The reachable workspace predicted by the 2-D FEM, SCHM and PRBM was derived using the respective Jacobians given in Table 5-3 and the respective maximum displacement of the piezo-actuators under load, $\Delta L_{\max,load}$, as given in Table 5-2.

Figures 5-7 to 5-10 show plots of the reachable workspace for the $XY\theta_Z$ micro-motion stage predicted by the 2-D FEM, SCHM and PRBM. The constant-

orientation workspace is also shown on these plots as an opaque yellow area. Figure 5-7 shows the vertex numbers as given in Table 5-3. It can be seen that the reachable workspace is a cube like shape.

In these plots the rotation of the stage, θ_Z , is plotted on the z-axis. The maximum rotation of the stage, $\theta_{Z,\max}$, occurs when all three piezo-actuators are at a maximum displacement, and is given by equation (5.4).

$$\theta_{Z,\max} = \Delta L_{\max,\text{load}} J_{31} + \Delta L_{\max,\text{load}} J_{32} + \Delta L_{\max,\text{load}} J_{33} \quad (5.4)$$

In this case the end-effector has no displacement in the X- or Y- axis. This point is defined by vertex number 8.

5.3.2 Constant-orientation workspace

For many applications, such as the positioning of a sample in the scanning electron microscope, it is necessary to keep the end-effector orientation constant. For each possible orientation of the end-effector there is a corresponding workspace area which the end-effector can reach. Inspection of Figures 5-7 and 5-8 can help to clarify this. At the extreme orientations, defined by vertex 1 and 8, the possible workspace area is only a single point. As the orientation moves away from these extremes, the workspace area becomes triangular. At orientations between vertices 2-3-5 and 4-6-7 the workspace becomes a hexagon. The shape of the hexagon varies

depending upon the orientation, as can be seen by comparing Figures 5-7 and 5-8.

The maximum constant-orientation workspace area occurs when the end-effector rotation is half of the maximum rotation, as given in equation (5.5).

$$\theta_{Z,const} = \theta_{Z,max} / 2 \quad (5.5)$$

For this orientation the workspace is a symmetrical hexagon, as shown in Figure 5-8. The maximum constant-orientation workspace area is smaller than the reachable workspace area. The piezo-actuator inputs that give the vertices describing the constant-orientation workspace are given in Table 5-5. The model Jacobians and equation (5.6) to (5.8) are used to determine the required input displacements $\Delta L_{1(\theta_{const})}$, $\Delta L_{2(\theta_{const})}$ and $\Delta L_{3(\theta_{const})}$.

$$\Delta L_{1(\theta_{const})} = (\theta_{Z,const} - (\Delta L_{3,max,load} J_{33} + \Delta L_{2,max,load} J_{32})) / J_{31} \quad (5.6)$$

$$\Delta L_{2(\theta_{const})} = (\theta_{Z,const} - (\Delta L_{1,max,load} J_{31} + \Delta L_{3,max,load} J_{33})) / J_{32} \quad (5.7)$$

$$\Delta L_{3(\theta_{const})} = (\theta_{Z,const} - (\Delta L_{1,max,load} J_{31} + \Delta L_{2,max,load} J_{32})) / J_{33} \quad (5.8)$$

Vertex Number	Piezo-Actuator Input Displacement		
	ΔL_1	ΔL_2	ΔL_3
9	$\Delta L_{\max,load}$	0	$\Delta L_{3(\theta_{Z,const})}$
10	$\Delta L_{\max,load}$	$\Delta L_{2(\theta_{Z,const})}$	0
11	0	$\Delta L_{\max,load}$	$\Delta L_{3(\theta_{Z,const})}$
12	$\Delta L_{1(\theta_{Z,const})}$	$\Delta L_{\max,load}$	0
13	0	$\Delta L_{2(\theta_{Z,const})}$	$\Delta L_{\max,load}$
14	$\Delta L_{1(\theta_{Z,const})}$	0	$\Delta L_{\max,load}$

Table 5-5 - Input displacement of piezo-actuators to give vertices of constant orientation workspace.

Figures 5-7 to 5-10 show the constant-orientation workspace predicted by the 2-D FEM, SCHM and PRBM, superimposed on the reachable workspace. The constant-orientation workspace is plotted as an opaque yellow area. It can be seen that the maximum constant-orientation workspace is a symmetrical hexagon. The centre of the hexagon is at $X=0$, $Y=0$. The input displacements that give this point are $\Delta L_1 = \Delta L_2 = \Delta L_3 = \Delta L_{\max,load}/2$.

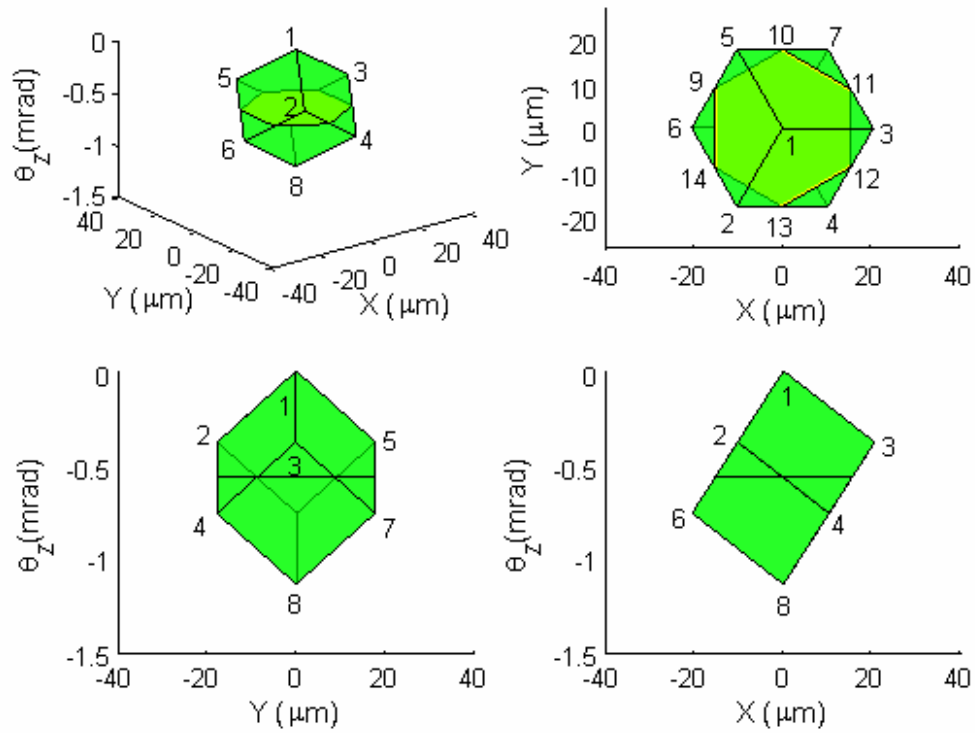


Figure 5-7 - Plots of reachable and maximum constant-orientation workspace predicted by 2-D FEM of the first prototype $XY\theta_z$ stage.

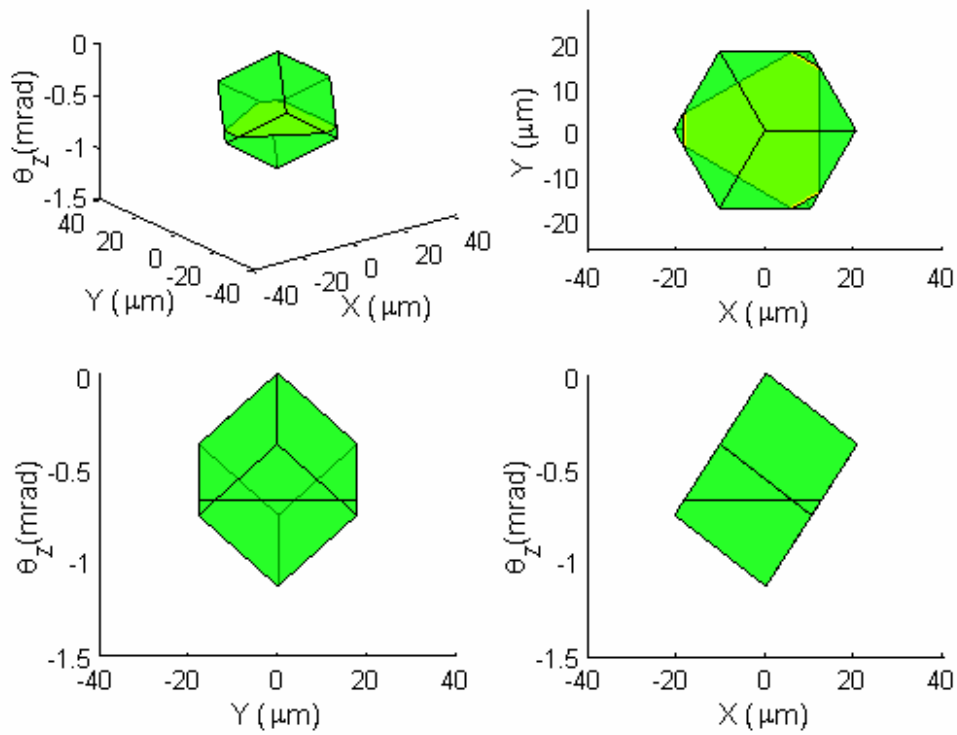


Figure 5-8 - Plots of reachable and, a less than maximum, constant-orientation workspace predicted by 2-D FEM of the first prototype $XY\theta_z$ stage.

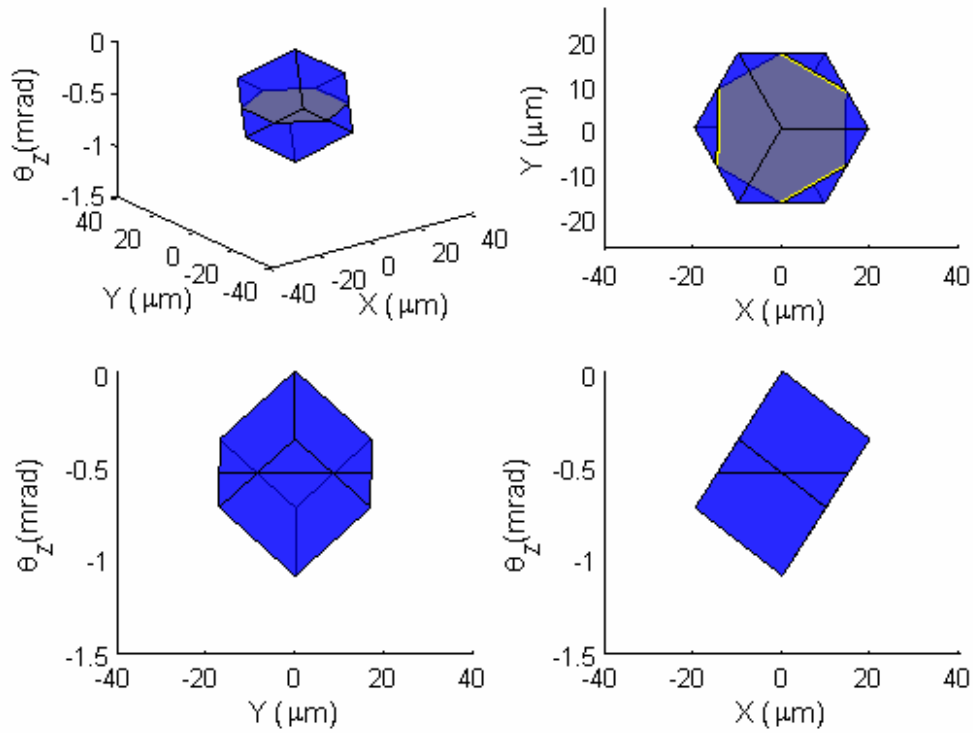


Figure 5-9 - Plots of reachable and maximum constant-orientation workspace predicted by SCHM, using $K_{\text{analytical}}$, of the first prototype $XY\theta_z$ stage.

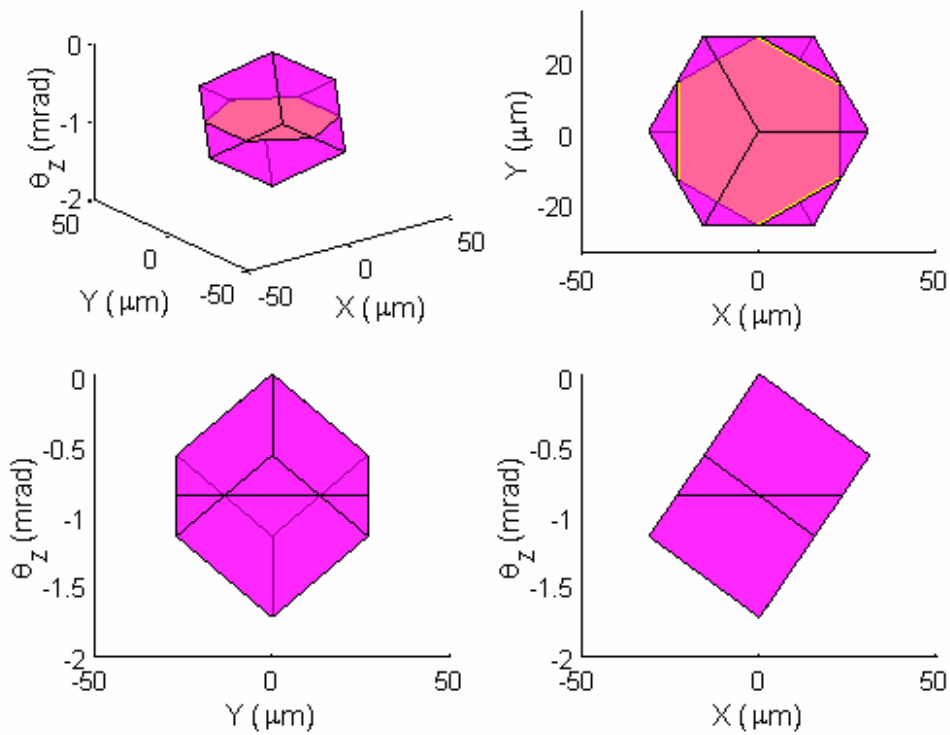


Figure 5-10 - Plots of reachable and maximum constant-orientation workspace predicted by PRBM, using $K_{\text{analytical}}$, of the first prototype $XY\theta_z$ stage.

5.3.3 Comparison of workspace

To give a comparison of the workspace areas the maximum constant-orientation workspaces of the 2-D FEM, SCHM and PRBM are plotted together in Figure 5-11.

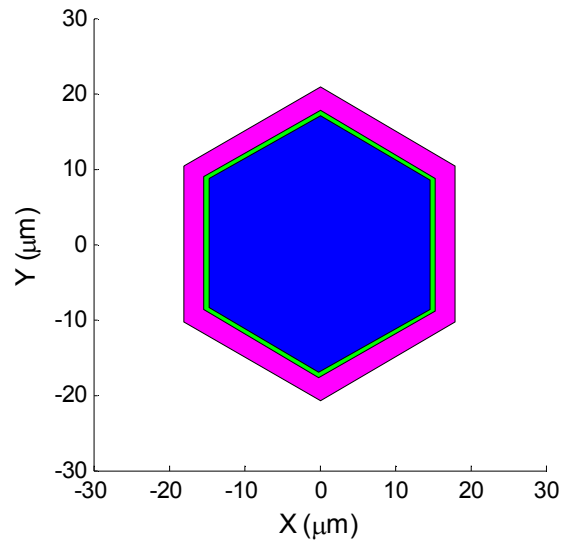


Figure 5-11 - Superimposed plots of constant orientation workspace predicted by the 2-D FEM (Green), SCHM (Blue) and PRBM (Magenta) for the first prototype $XY\theta_z$ stage.

5.3.3.1 Workspace width

Both the reachable workspace and constant-orientation workspace are symmetrical hexagons when viewed in the X-Y plane, as can be seen in Figure 5-12.

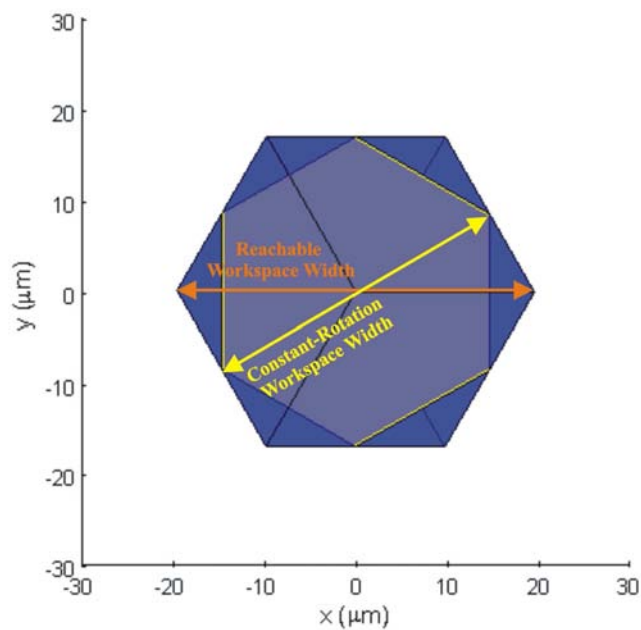


Figure 5-12 – Reachable and maximum constant-orientation workspace widths for the first prototype $XY\theta_z$ stage predicted by the SCHM.

A simple measure to compare the size of the workspace X-Y areas is the workspace width, as shown in Figure 5-12. Table 5-6 gives the reachable and maximum constant-orientation workspace width for the 2-D FEM, SCHM and PRBM.

	2-D FEM	SCHM	% diff.	PRBM	% diff.
Reachable Workspace Width (μm)	40.9	39.1	4.4	48.1	-17.6
Maximum Constant-Orientation Workspace Width (μm)	35.4	33.9	4.2	41.6	-17.5

Table 5-6 - Reachable and maximum constant-orientation workspace widths for the first prototype $XY\theta_z$ stage predicted by the 2-D FEM, SCHM and PRBM, and difference of SCHM and PRBM compared to the 2-D FEM.

From Figure 5-12 and Table 5-6 it can be seen that the 2-D FEM and the SCHM predict similar workspaces, while the PRBM predicts a considerably larger reachable and maximum constant-orientation workspace. All models predict workspaces with the same shape, proportions and orientation.

5.4 Natural frequency

A modal analysis was performed in ANSYS to determine the natural frequencies of the $XY\theta_z$ micro-motion stage predicted by the 2-D FEM, SCHM and PRBM. The 2-D FEM used the Block Lanczos mode extraction method, while the PRBM and SCHM used the reduced mode extraction method. The first three modes were determined. These modes correspond to two translational modes in the x-, y- plane and one rotational mode about the z-axis. Table 5-7 gives the natural frequencies of the first prototype $XY\theta_z$ stage predicted by the 2-D FEM, SCHM and PRBM, and gives the difference of the SCHM and PRBM compared to the 2-D FEM.

Mode	2-D FEM	SCHM				PRBM			
		$K_{\text{analytical}}$		K_{FEA}		$K_{\text{analytical}}$		K_{FEA}	
		ω_n	% diff	ω_n	% diff	ω_n	% diff	ω_n	% diff
1st translation	1002	1166	-16.4	1112	-11.0	1345	-34.2	1299	-29.7
2nd translation	1002	1166	-16.4	1112	-11.0	1345	-34.2	1299	-29.7
1st rotation	1509	2549	-68.9	2424	-60.6	2871	-90.2	2769	-83.5

Table 5-7 – Natural frequencies for the first prototype $XY\theta_z$ stage predicted by the 2-D FEM, SCHM and PRBM, and difference of SCHM and PRBM compared to the 2-D FEM.

From Table 5-7 it can be seen that all models predict two translational modes with the same frequency, and the rotational mode at a higher frequency. The SCHM and PRBM predictions differ significantly from one another. The SCHM prediction is closer to the 2-D FEM. For both the SCHM and PRBM the models using K_{FEA} give a prediction closer to the 2-D FEM by 5%. The SCHM and PRBM prediction for the rotational mode is very far from to the 2-D FEM prediction. This is due to inaccurate modelling of the end-effector.

Comparing Table 5-7 to Table 4-15 it can be observed that the 3RRR compliant mechanism and the $XY\theta_Z$ stage models predict significantly different natural frequencies. The 2-D FEM models predict the $XY\theta_Z$ stage natural frequency to be 50% higher than the 3RRR compliant mechanism. An increase in natural frequency is expected as the addition of the piezo-actuators increases the stiffness of the stage. It can also be noted that the difference in prediction between the PRBM and 2-D FEM is much greater for the $XY\theta_Z$ stage than for the 3RRR compliant mechanism. The reason for this is not clear.

5.5 Static-Coupling

Static-coupling describes the interference between actuators caused by the transmission of forces through the mechanism from one input-link to another. This was defined in Chapter 4. The static-coupling is significantly affected by the presence of the piezo-actuators and therefore static-coupling has been determined for the $XY\theta_Z$ stage.

	2-D FEM	SCHM				PRBM			
		$K_{\text{analytical}}$		K_{FEA}		$K_{\text{analytical}}$		K_{FEA}	
		% diff.	% diff.	% diff.	% diff.	% diff.	% diff.	% diff.	% diff.
Static-Coupling 1/2	-0.002	-0.003	-26.9	-0.003	-33.8	-0.009	-291.4	-0.008	-242.2
Static-Coupling 3/2	-0.002	-0.003	-26.9	-0.003	-33.8	-0.009	-291.4	-0.008	-242.2

Table 5-8 - Static-coupling for the first prototype $XY\theta_Z$ stage predicted by the 2-D FEM, SCHM and PRBM.

From Table 5-8 it can be observed that static-coupling 1/2 and 3/2 are identical. This is due to the symmetry of the compliant mechanism and piezo-actuators. It can also be observed that the 2-D FEM and SCHM predict significantly different static-coupling and, when K_{FEA} is used, the result is further from the 2-D FEM, which is unexpected. The PRBM prediction of static-coupling is very far from the 2-D FEM.

Comparison of Table 5-8 with Table 4-18, reveals that the 3RRR compliant mechanism and the $XY\theta_Z$ stage static-coupling differ significantly. The 2-D FEM predicts that the compliant mechanism coupling will be 5 times greater than that of the $XY\theta_Z$ stage.

5.6 Discussion

The results presented in this chapter indicate how the piezo-actuator and compliant mechanism affect each other. It can be seen that the compliant mechanism affects the piezo-actuator behaviour, reducing its elongation. While the piezo-actuator affects the compliant mechanism behaviour, increasing the natural frequency and reducing static-coupling. Thus, this demonstrates the importance of modelling both the compliant mechanism and piezo-actuator to give a more complete $XY\theta_Z$ stage model.

Furthermore, these results, using the $XY\theta_Z$ stage model, have given a detailed picture of the workspace of the $XY\theta_Z$ stage. The reachable and constant-orientation

workspaces were clearly identified. This understanding of workspace shape, size and orientation is useful knowledge for the stage designer.

From these results the difference between the SCHM and PRBM can again be clearly seen. For this particular geometry of $XY\theta_z$ stage the SCHM gives predictions for kinematic and dynamic behaviour far closer to the 2-D FEM than the PRBM. It can also be noted that the differences between the PRBM and the 2-D FEM is more significant for the $XY\theta_z$ stage than for the 3RRR compliant mechanism.

Chapter

6 Parametric study of the $XY\theta_Z$ micro-motion stage

In chapter 4 a computationally efficient, yet relatively accurate compliant mechanism modelling method, the SCHM, was developed. Using the SCHM a model of the 3RRR compliant mechanism was constructed. In chapter 5 the 3RRR compliant mechanism model was combined with a linear piezo-actuator model to give the $XY\theta_Z$ micro-motion stage model. The model using the SCHM is well suited for use in optimal design as it is computationally efficient. Prior to performing design optimisation a parametric sensitivity study will be conducted. In this study one design parameter at a time will be varied and the output characteristics of the mechanism observed. The output characteristics of interest are reachable workspace-width, maximum stage rotation, natural frequency and static-coupling. The study will give an understanding of how each parameter affects the output characteristics. The results of this study may suggest some design rules that can be used to help the optimisation process. The study will give a better understanding of the design space of the optimisation problem. It may then be possible to simplify the optimisation

problem by establishing relationships between parameters so that the number of independent design variables is reduced.

The same study will also be conducted using a SCHM and PRBM of the 3RRR compliant mechanism alone, so that a direct comparison can be given between the SCHM and the PRBM of the 3RRR compliant mechanism. All the models are constructed in ANSYS.

The output characteristics for each parameter are all affected to a small degree by the choice of the other parameters. The results given in this chapter show the effects of changing just one parameter at a time. The significant trends shown in the plots are the same regardless of the choice of parameters. The material properties were kept the same throughout the study.

6.1 3RRR Compliant Mechanism Parameters

The parameters defining the 3RRR mechanism are shown in Figures 6-1, 6-2 and 6-3, and are tabulated in Table 6-1. The material properties for the mechanism and piezo-actuator are given in Table 6-2.

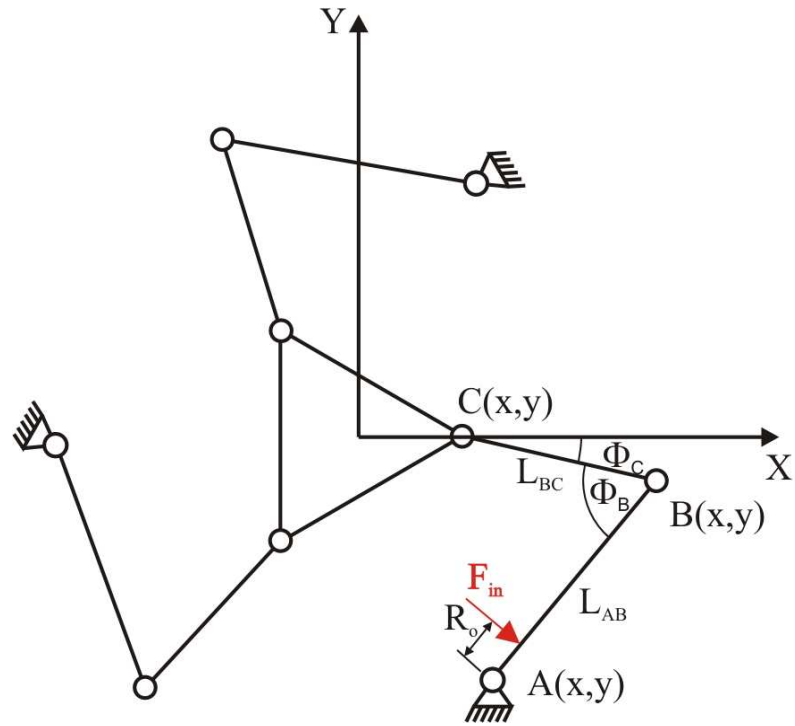


Figure 6-1 - Schematic of the 3RRR compliant mechanism showing linkage parameters.

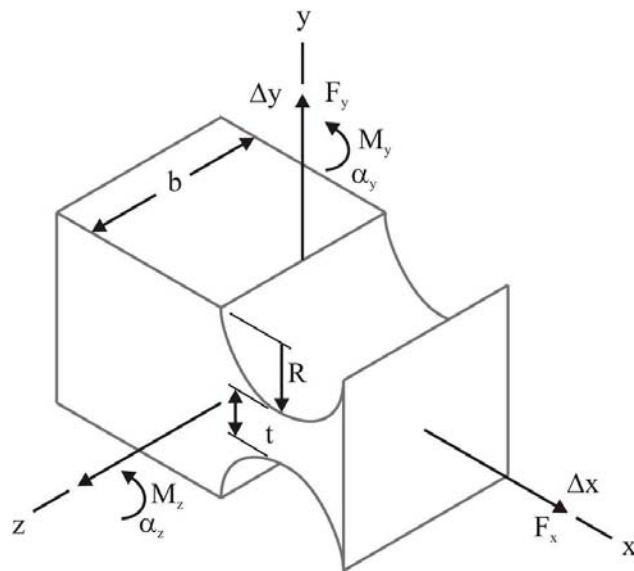
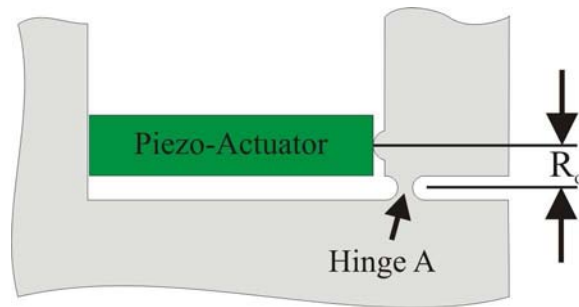


Figure 6-2 - Schematic of a circular flexure hinge showing hinge parameters.


 Figure 6-3 - Schematic of the piezo-actuator and hinge A showing parameter R_o .

3RRR Parameter	Range
End-effector size (C_x, C_y)	Fixed - $C_x=20\text{mm}$, $C_y=0\text{mm}$
Mechanism thickness (b)	Fixed - 12.8mm
Link Width (h)	Fixed - 10mm
Link _{AB} Length (L_{AB})	10 to 100 mm
Link _{BC} Length (L_{BC})	10 to 100 mm
ϕ_B	10° to 180°
ϕ_C	-100° to 100°
$R_{A, B \text{ and } C}$	1 to 10 mm
$t_{A, B \text{ and } C}$	0.3 to 3 mm
R_o	2 to 10mm (3.5mm unless stated otherwise)

Table 6-1– 3RRR compliant mechanism parameters.

Material Properties for 7075-T6 Aluminium plate	
Young's Modulus (E)	72GPa
Shear Modulus (G)	27.1GPa
Proportional limit (σ_p)	503MPa
Material Properties for Tonkin AE0505D16 Piezo-actuator	
Un-loaded displacement ($\Delta L_{\text{no-load}}$) @100V	$11.6 \pm 2.0 \mu\text{m}$
Stiffness, $K_{\text{piezo-actuator}}$	$55\text{N}/\mu\text{m}$
Length	20mm

Table 6-2 - Material properties of compliant mechanism and piezo-actuator.

6.2 Output Characteristics

The output characteristics returned by the model are reachable workspace width, maximum stage rotation, $\theta_{z,\max}$, first mode natural frequency, ω_n , which corresponds to a translational mode, and static-coupling. These characteristics have been discussed in Chapter 5.

Figures 6-4 to 6-8 show plots of each output characteristic versus the geometric parameter of interest. Comments on the results for each parameter are also given.

6.3 Effect of Geometric Parameter Variations

6.3.1 Variation of L_{AB}

The first parameter to be varied is the length of link_{AB} (L_{AB}). The plots of linkage configurations and output characteristics are given in Figure 6-4.

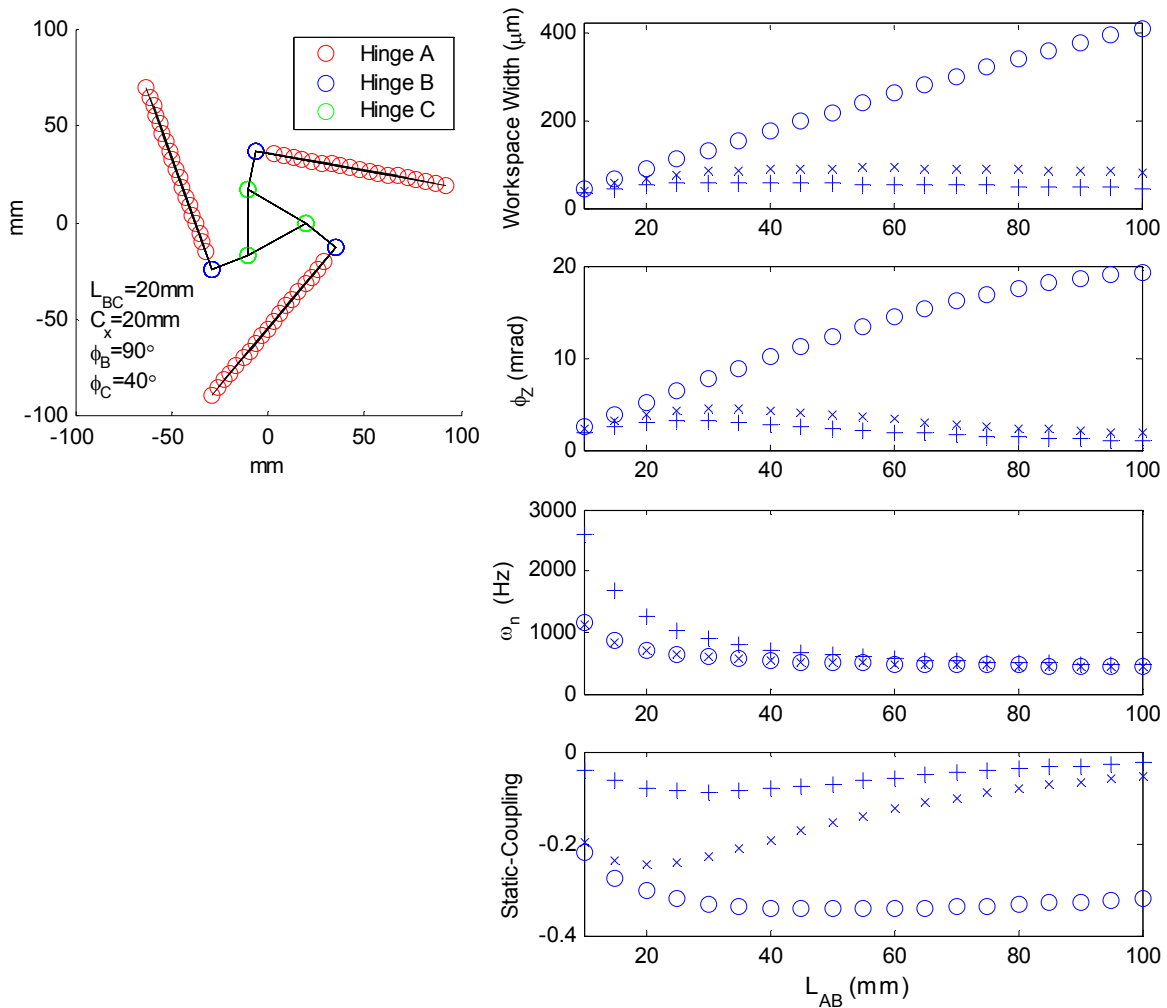


Figure 6-4 - Linkage configuration (left) and output characteristics (right) of SCHM of $XY\theta_Z$ stage (+), SCHM of 3RRR (x), and PRBM of 3RRR (O), when L_{AB} is varied ($R_o=3.5\text{mm}$, $t_{A,B,C}=0.94\text{mm}$, $R_{A,B,C}=1.5\text{mm}$).

Workspace width and maximum rotation, $\theta_{Z,\max}$

The PRBM of the 3RRR predicts a significant and proportional increase of both workspace width and $\theta_{Z,\max}$ with increase of L_{AB} . The SCHM of the 3RRR and $XY\theta_Z$ stage predicts a non-linear increase that tends to horizontal at approximately 30mm. The SCHM of the $XY\theta_Z$ stage predicts a slightly smaller workspace width and $\theta_{Z,\max}$ than the SCHM of the 3RRR.

Natural Frequency, ω_n

All models predict that increasing L_{AB} decreases the ω_n in a non-linear way. The PRBM and SCHM of the 3RRR give similar predictions of ω_n , while the SCHM of the $XY\theta_Z$ stage predicts significantly higher ω_n .

Static-Coupling

The three models give significantly different predictions of static-coupling trends. The SCHM of the $XY\theta_Z$ stage predicts that changing L_{AB} has a minor effect on the static-coupling, while the SCHM and PRBM of the 3RRR both predict a more significant effect. The PRBM predicts very significant coupling as L_{AB} increases, while the SCHM predicts that coupling becomes less significant as L_{AB} increases.

6.3.2 Variation of L_{BC}

The second parameter to be varied is the length of link_{BC} (L_{BC}). The plots of linkage configurations and output characteristics are given in Figure 6-5.

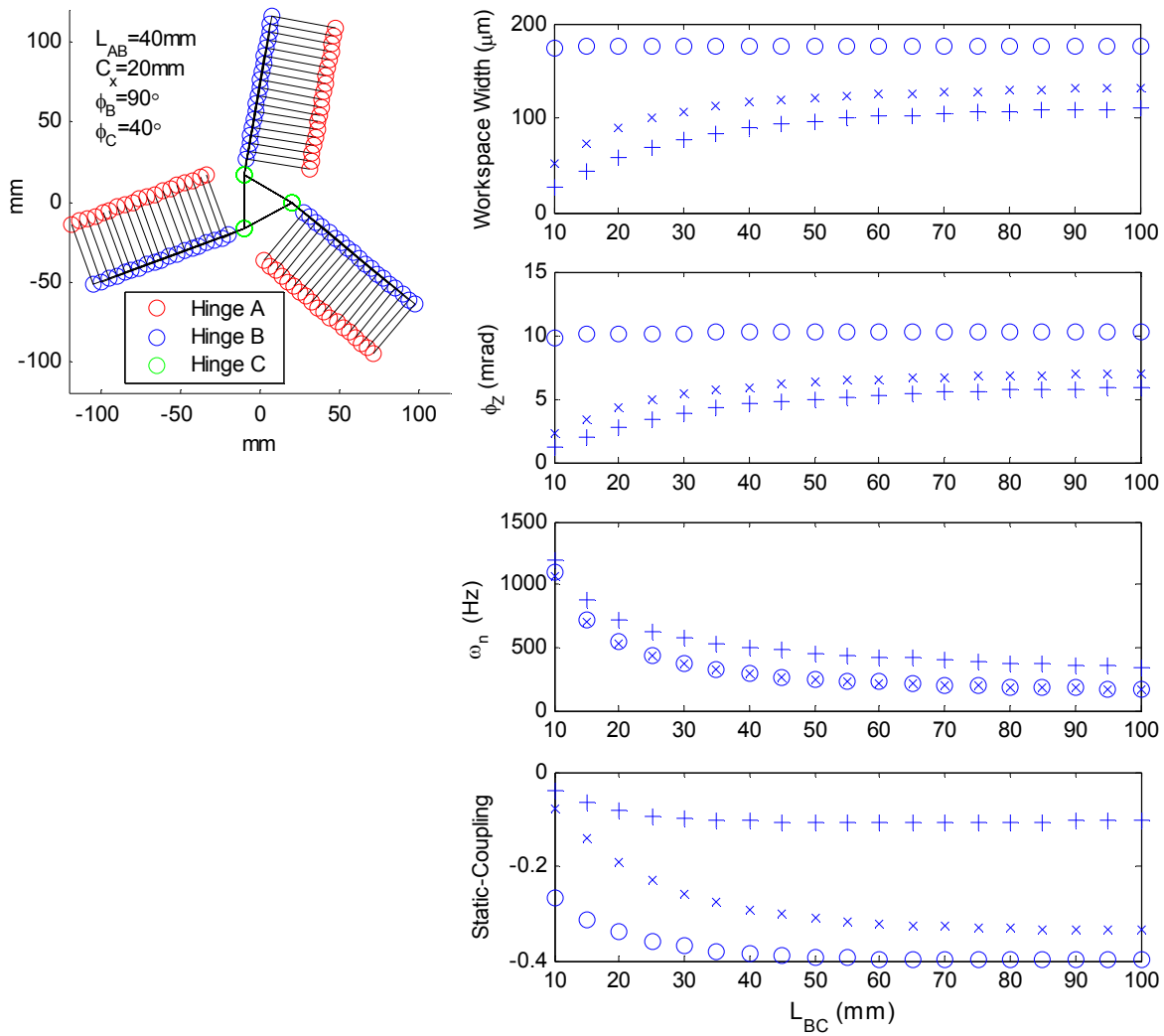


Figure 6-5 - Linkage configuration (left) and output characteristics (right) for SCHM of $XY\theta_Z$ stage (+), SCHM of 3RRR (x) and PRBM of 3RRR (O), when L_{BC} is varied ($R_o=3.5\text{mm}$, $t_{A,B,C}=0.94\text{mm}$, $R_{A,B,C}=1.5\text{mm}$).

Workspace width and maximum rotation, $\theta_{Z,\max}$

The SCHM of the $XY\theta_Z$ stage and 3RRR both predict a non-linear increase of workspace width and $\theta_{Z,\max}$ that tends to horizontal as $L_{BC} > L_{AB}$. The SCHM of the $XY\theta_Z$ stage predicts a significantly smaller workspace width and $\theta_{Z,\max}$ than the SCHM of the 3RRR. The PRBM of the 3RRR predicts that the workspace width and $\theta_{Z,\max}$ are not affected by changing L_{BC} .

Natural Frequency, ω_n

All models predict that increasing L_{BC} decreases the ω_n in a non-linear way. The PRBM and SCHM of the 3RRR give very similar predictions of ω_n , while the SCHM of the $XY\theta_Z$ stage predicts significantly higher ω_n .

Static-Coupling

All models predict that increasing L_{BC} increases the magnitude of static coupling. The SCHM of the $XY\theta_Z$ stage predicts that changing L_{BC} has only a minor effect on the static-coupling, while the SCHM and PRBM of the 3RRR both predict a more significant effect. The plots are significantly different.

6.3.3 Variation of ϕ_B

The third parameter to be varied is the angle between links 1 and 2 at hinge B (ϕ_B).

The plots of linkage configurations and output characteristics are given in Figure 6-6.

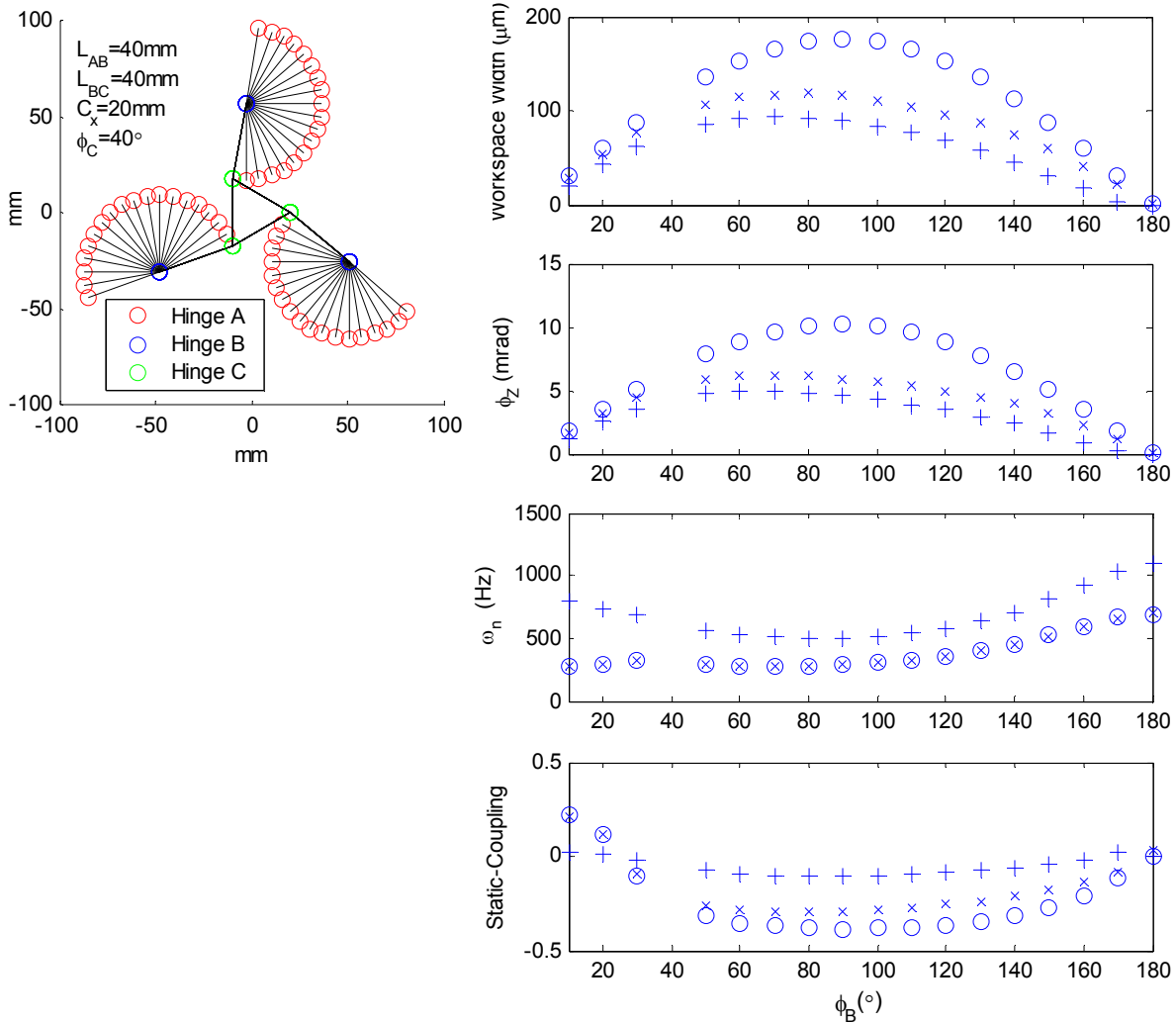


Figure 6-6 - Linkage configuration (left) and output characteristics (right) for SCHM of $XY\theta_Z$ stage (+), SCHM of 3RRR (\times) and PRBM of 3RRR (O), when ϕ_B is varied ($R_o=3.5\text{mm}$, $t_{A,B,C}=0.94\text{mm}$, $R_{A,B,C}=1.5\text{mm}$)

Workspace width and maximum rotation, $\theta_{Z,\max}$

All models predict that the workspace width and $\theta_{Z,\max}$ change significantly with ϕ_B ; there is a single maximum that occurs near to $\phi_B=90^\circ$, while workspace width and $\theta_{Z,\max}$ tend to zero at $\phi_B=0^\circ$ and $\phi_B=180^\circ$. The SCHM of the $XY\theta_Z$ stage and 3RRR both predict the maximum workspace width and $\theta_{Z,\max}$ to occur at close to $\phi_B=80^\circ$. The $XY\theta_Z$ model predicts a smaller workspace width and $\theta_{Z,\max}$ than the 3RRR, but with similar shape curve. The PRBM of the 3RRR predicts the maximum at $\phi_B=90^\circ$.

Natural Frequency, ω_n

All models predict that increasing ϕ_B significantly changes the ω_n in a non-linear way. The PRBM and SCHM of the 3RRR give very similar predictions of ω_n , while the SCHM of the $XY\theta_Z$ stage predicts significantly higher ω_n . All models predict the maximum occurs at $\phi_B=180^\circ$, while the minimum is predicted to occur at; $\phi_B=90^\circ$ for the $XY\theta_Z$ model, and at $\phi_B=0^\circ$ for the 3RRR models.

Static-Coupling

The SCHM of the $XY\theta_Z$ stage predicts that changing L_{AB} has a minor effect on the static-coupling, while the SCHM and PRBM of the 3RRR both predict a more significant effect. All models predict an absolute maximum at approximately $\phi_B=90^\circ$.

6.3.4 Variation of ϕ_C

The fourth parameter to be varied is the angle between links 2 and the end-effector at hinge C (ϕ_C). The plots of linkage configurations and output characteristics are given in Figure 6-7. It was found that both the PRBM and SCHM were unsolvable at $\phi_C = 0^\circ$ and $\pm 90^\circ$. These configurations are singularities. Furthermore the PRBM was unsolvable when $\phi_C = \pm 95^\circ$ and $\pm 100^\circ$, suggesting a singularity in the equations.

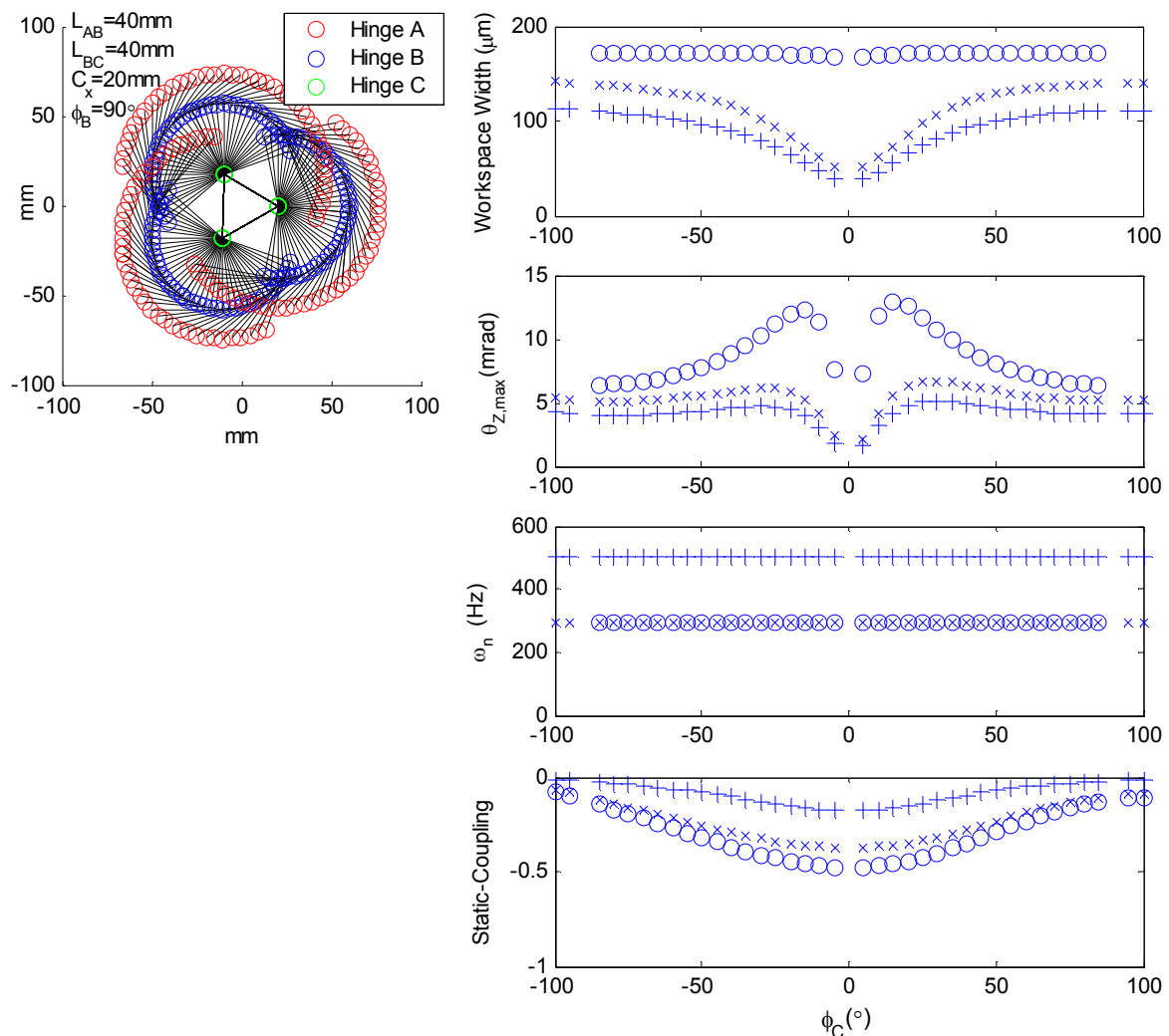


Figure 6-7 - Linkage configuration (left) and output characteristics (right) for SCHM of $XY\theta_Z$ stage (+), SCHM of 3RRR (x) and PRBM of 3RRR (O), when ϕ_B is varied ($R_o=3.5\text{mm}$, $t_{A,B,C}=0.94\text{mm}$, $R_{A,B,C}=1.5\text{mm}$).

Workspace width

The SCHM of the $XY\theta_Z$ stage and 3RRR both predict that the workspace width increases, in a non-linear way, with increasing $|\phi_C|$ from zero at $\phi_C=0^\circ$. The $XY\theta_Z$ model predicts a smaller workspace width than the 3RRR. The PRBM of the 3RRR predicts no significant change of workspace width with changing ϕ_C .

Maximum rotation, $\theta_{Z,\max}$

The SCHM of the $XY\theta_Z$ stage and 3RRR both predict an increase in $\theta_{Z,\max}$ as $|\phi_C|$ decreases, reaching a peak at $\phi_C= \pm 10^\circ$ and then decreases as ϕ_C approaches zero. The PRBM of the 3RRR predicts that the $\theta_{Z,\max}$ increases continually as ϕ_C approaches zero.

Natural Frequency, ω_n

All models predict that ω_n does not change with changing ϕ_C . The SCHM and PRBM of the 3RRR give very similar predictions of ω_n while the SCHM of the $XY\theta_Z$ stage model predicts significantly higher ω_n .

Static-Coupling

All models predict that changing ϕ_C has a significant effect on the static-coupling. All three models give similar non-linear plots, for which static-coupling has a maximum absolute value at $\phi_C= 0^\circ$ and a minimum absolute value at $\phi_C= \pm 100^\circ$. The $XY\theta_Z$ stage model predicts the magnitude of static-coupling to be less significant than the 3RRR models.

6.3.5 Variation of R_o

The fifth parameter to be varied is the distance between the centre of hinge A and the centre line of the piezo-actuator, R_o , as shown in Figure 6-3. The plot of output characteristics are given in Figure 6-8.

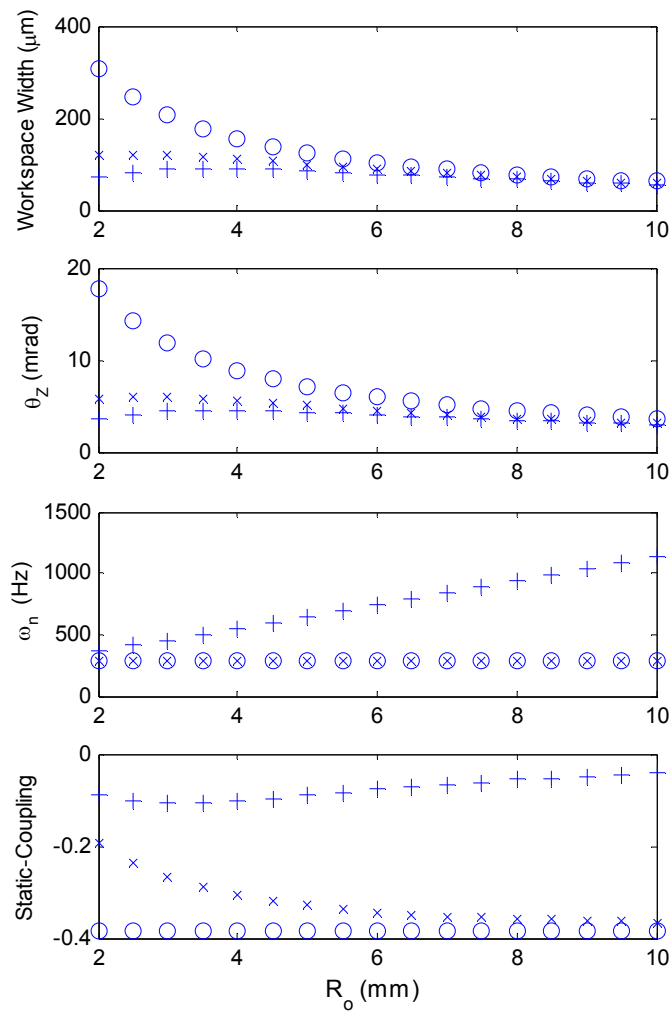


Figure 6-8 - Output characteristics for SCHM of $XY\theta_Z$ stage (+), SCHM of 3RRR (x) and PRBM of 3RRR (O), when R_o is varied ($L_{AB} = 40\text{mm}$, $L_{BC} = 40\text{mm}$, $\phi_B = 90^\circ$, $\phi_C = 40^\circ$, $R_o = 3.5\text{mm}$, $t_{A,B,C} = 0.94\text{mm}$, $R_{A,B,C} = 1.5\text{mm}$)

Workspace width and maximum rotation, $\theta_{Z,\max}$

The PRBM of the 3RRR predicts a very significant non-linear decrease of workspace width and $\theta_{Z,\max}$ with increasing R_o . The SCHM of the 3RRR and $XY\theta_Z$ stage predict a less significant non-linear change with changing R_o and predict the maximum to occur close to 3mm, which is two times R_A . The SCHM of the $XY\theta_Z$ stage predicts a significantly smaller workspace width and $\theta_{Z,\max}$ than the SCHM of the 3RRR.

Natural Frequency, ω_n

The SCHM and PRBM of the 3RRR give very similar predictions of ω_n and predict that there is no significant change of ω_n with changing R_o , while the SCHM of the $XY\theta_Z$ stage predicts a significant increase of ω_n with increasing R_o .

Static-Coupling

The three models predict significantly different trends in static-coupling with changing R_o . The PRBM of the 3RRR predicts no change in static coupling with changing R_o . The SCHM of the $XY\theta_Z$ stage predicts that changing R_o has a minor effect on the static-coupling, while the SCHM of the 3RRR predicts a significant, non-linear, increase in the absolute magnitude of coupling with increasing R_o .

6.4 Discussion

From Figures 6-4 to 6-8 several observations can be made. It is apparent that there are some significant differences in the predictions given by the models. The predictions of the workspace width, maximum rotation, $\theta_{Z,\max}$, and static-coupling,

given by the SCHM and PRBM of the 3RRR compliant mechanism differ significantly for most parameter variations. There are some very significant differences in the trends predicted by the SCHM and PRBM. These results indicate that, if the SCHM is demonstrated to be more accurate than the PRBM, the SCHM should be used in preference to the PRBM in parametric study and optimisation, where the workspace, rotation and static-coupling are of concern. The results given in Chapter 4 suggest that, indeed, the SCHM is more accurate than the PRBM.

The predictions for the natural frequency, ω_n , given by the SCHM and PRBM are almost identical for all parameter variations. Therefore, if the only output characteristic of concern is the natural frequency, then either the SCHM or PRBM may be used.

For most parameter variations and output characteristics the SCHM of the $XY\theta_Z$ and the SCHM of the 3RRR predict similar changes, but the magnitude of workspace width, maximum rotation, $\theta_{Z,max}$, and static-coupling is significantly less for the $XY\theta_Z$, while the prediction of natural frequency, ω_n , is significantly greater for the $XY\theta_Z$. This highlights the importance of including the piezo-actuator into the model if a design with specific output characteristics is needed.

6.4.1 Design Rules

The results of this study can be used to establish some rules of thumb to aid in the design process. The rules given below were established based upon the predictions given by the SCHM of the $XY\theta_Z$ stage.

Selection of L_{AB}

- If a larger workspace and $\theta_{Z,max}$ are desired then L_{AB} should be increased to the length that gives the maximum output. Iterative design or optimisation is needed to determine this length.
- If a higher ω_h is desired then L_{AB} should be decreased.

Selection of L_{BC}

- If a larger workspace and rotation are desired then L_{BC} should be increased so that $L_{BC} \geq L_{AB}$.
- If a higher ω_h is desired then L_{BC} should be decreased.

Selection of ϕ_B

- To increase the workspace and rotation set $\phi_B = 80^\circ - 90^\circ$.
- If a higher ω_h is desired then ϕ_B should be increased.

Selection of ϕ_C

- If a larger workspace is desired then $|\phi_C|$ should be increased.
- If a larger rotation is desired then $|\phi_C|$ should be decreased.

Selection of R_o

- To increase the workspace and rotation R_o should be reduced to the value that gives the maximum output, iterative design or optimisation can be used.

However, the value of R_o that gives the maximum output is close to the value of R_A . In a practical design the minimum possible value of R_o will depend on R_A and the space required for the piezo-actuator mounting, see Figure 6-3. In most cases the minimum practically possible R_o will be greater than the value that gives the maximum output and therefore the minimum practical value should be used.

- To increase the ω_n , R_o should be increased.

Alternatively, if one output characteristic alone is of concern the following design rules can be applied:

To increase workspace only:

- set L_{AB} to value that gives maximum output using iterative design or optimisation.
- set $L_{BC} \geq L_{AB}$.
- set $\phi_B = 80^\circ - 90^\circ$.
- increase $|\phi_C|$.
- set R_o to value that gives maximum output using iterative design or optimisation, or use the minimum practical value.

To increase $\theta_{Z,max}$ only:

- set L_{AB} to value that gives maximum output using iterative design or optimisation.
- set $L_{BC} \geq L_{AB}$.
- set $\phi_B = 80^\circ - 90^\circ$.

- set $|\phi_C|$ to value that gives maximum output using iterative design or optimisation.
- set R_o to value that gives maximum output using iterative design or optimisation, or use the minimum practical value.

To increase ω_n only:

- decrease L_{AB} and L_{BC} .
- set $\phi_B \approx 0^\circ$ or 180° .
- increase R_o .

To minimise static-coupling only:

- decrease L_{BC} .
- set $\phi_B \approx 0^\circ$ or 180° .
- increase $|\phi_C|$.

In all cases the design of the hinges must also be considered and it must be ensured that the hinges are designed to provide the required rotation. The hinge design is considered in the following section.

6.5 Effect of hinge design

The design of the flexure hinge has a significant impact on the kinematics and dynamics of the 3RRR compliant mechanism and $XY\theta_Z$ stage. This section will discuss how the hinge design affects the hinge performance and present the results of a parametric study of hinges A, B and C.

In Chapter 4 a model was presented that considered the planar flexure hinge to be a 3-DOF joint. This representation of the flexure hinge is shown again in Figure 6-9(b). This joint is described by three stiffness terms K_b , K_x and K_y . These three stiffness terms are affected by the hinge parameters R and t , shown in Figure 6-9(a). Thus R and t should be selected carefully in order to give hinge stiffness terms that can provide the compliant mechanism with desirable performance specifications. Out of plane compliance is not considered in this analysis.

6.5.1 Simple lever example

To understand how the hinge stiffness affects the mechanism performance a simple example is presented. The simple amplifying lever will be considered as an example. Figure 6-9 shows schematic diagrams of a lever using a flexure hinge with a force applied. Figure 6-9(a), shows the flexure hinge; Figure 6-9(b) shows a 3-DOF model representation of the flexure hinge; and Figure 6-9(c) demonstrates the displacement of the lever arm when the flexure hinge has both rotational and translational compliance.

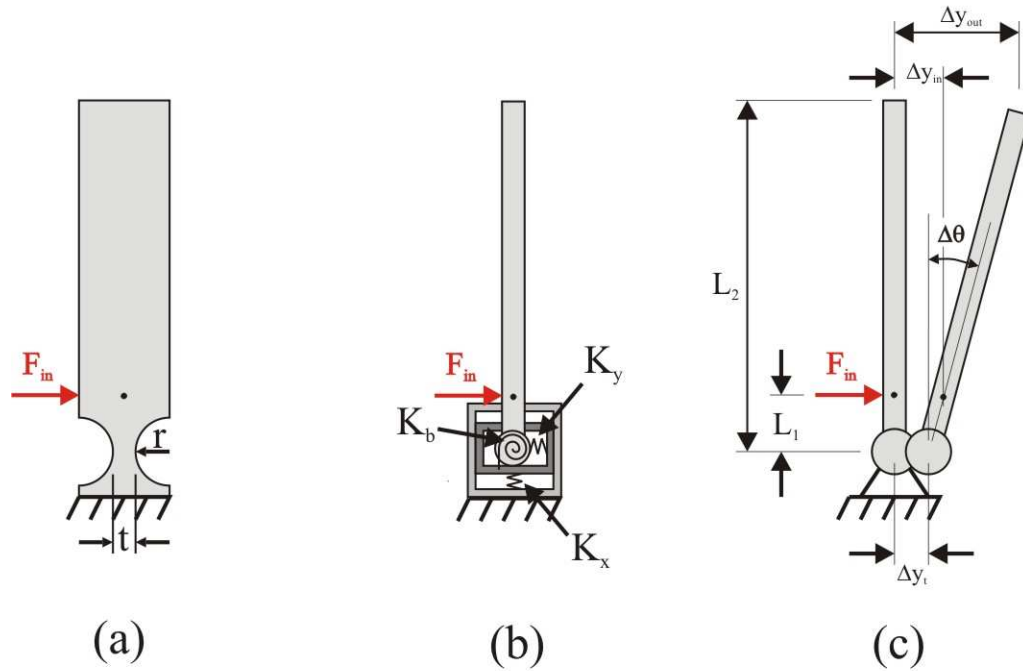


Figure 6-9 - (a) Flexure hinge and link, (b) 3-DOF model of hinge and link, (c) Schematic showing displacement of link.

As can be seen in Figure 6-9(c) the lever provides displacement amplification given by $\Delta y_{out} / \Delta y_{in}$. If the flexure hinge provided purely revolute motion and the rotational displacement is very small then the amplification of the lever can be given by L_2 / L_1 . This is the ideal gain, G_{ideal} , and is greater than 1 for the case of a displacement amplifying lever. The output displacement is given by equation (6.1).

$$\Delta y_{out} (ideal) = \Delta y_{in} \frac{L_2}{L_1} = \Delta y_{in} G_{ideal} \quad (6.1)$$

However, for the case of the flexure hinge with 3-DOF the input force causes a translation, Δy_t , and rotation, $\Delta\theta$, of the lever as schematically shown in Figure 6-9(c). The output displacement is given by equation (6.2).

$$\Delta y_{out} = \frac{(\Delta y_{in} - \Delta y_t)L_2}{L_1} + \Delta y_t = \Delta y_{in} G_{ideal} - \Delta y_t (G_{ideal} - 1) \quad (6.2)$$

The translation of the lever, Δy_t , is input motion that is not amplified by the lever. Therefore the amplification is less than G_{ideal} . The greater Δy_t the less the lever amplification will be. The translational stiffness of the flexure hinge K_y determines the amount of translational motion, Δy_t , of the lever. The larger the K_y the smaller the Δy_t . To get the greatest amplification K_y should be as large as possible.

Furthermore, if K_x and K_y are large then the rotational motion of the lever is more precise and the motion of the lever is more predictable under any loading condition. This is desirable for the sake of precise and predictable motion.

The analytical equations for the stiffness of the flexure hinge [Wu, 2002] are given in equations (6.3), (6.4), and (6.5). These give insight to how the selection of R and t affects the hinge stiffness K_b , K_x and K_y .

$$\frac{1}{K_b} = \frac{\alpha_z}{M_z} = \frac{12}{EbR^2} \left[\frac{2s^3(6s^2 + 4s + 1)}{(2s + 1)(4s + 1)^2} + \frac{12s^4(2s + 1)}{(4s + 1)^{5/2}} \arctan \sqrt{4s + 1} \right] \quad (6.3)$$

$$\frac{1}{K_y} = \frac{\Delta y}{F_y} = \frac{12}{Eb} \left[\frac{s(24s^4 + 24s^3 + 22s^2 + 8s + 1)}{2(2s+1)(4s+1)^2} + \frac{(2s+1)(24s^4 + 8s^3 - 14s^2 - 8s - 1)}{2(4s+1)^{5/2}} \right] + \arctan \sqrt{4s+1} + \frac{\pi}{8} + \frac{1}{Gb} \left[\frac{2(2s+1)}{\sqrt{4s+1}} \arctan \sqrt{4s+1} - \frac{\pi}{2} \right] \quad (6.4)$$

$$\frac{1}{K_x} = \frac{\Delta x}{F_x} = \frac{1}{Eb} \left[\frac{2(2s+1)}{\sqrt{4s+1}} \arctan \sqrt{4s+1} - \frac{\pi}{2} \right] \quad (6.5)$$

where E is Young's modulus, G is the shear modulus, b is the material thickness and s is given by equation (6.6)

$$s = R/t \quad (6.6)$$

Observation of these equations reveals that K_x and K_y are dependent on s only, while K_b is dependent on s and R. Therefore K_x and K_y can be maximised by careful selection of s. To understand how s affects K_x and K_y a plot of K_x versus s and K_y versus s is given in Figure 6-10 and Figure 6-11, respectively.

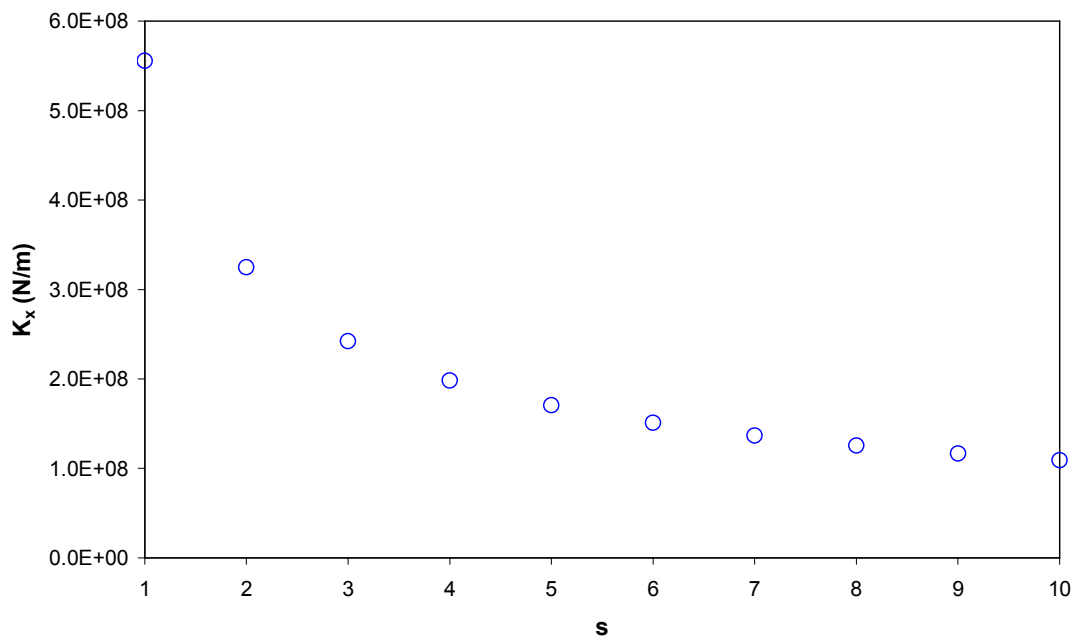


Figure 6-10 - Plot of K_x vs s for a circular flexure hinge with $E=72\text{GPa}$, $G=27\text{GPa}$, $b=11.7\text{mm}$, $t=0.5\text{mm}$, $R=0.5-5\text{mm}$.

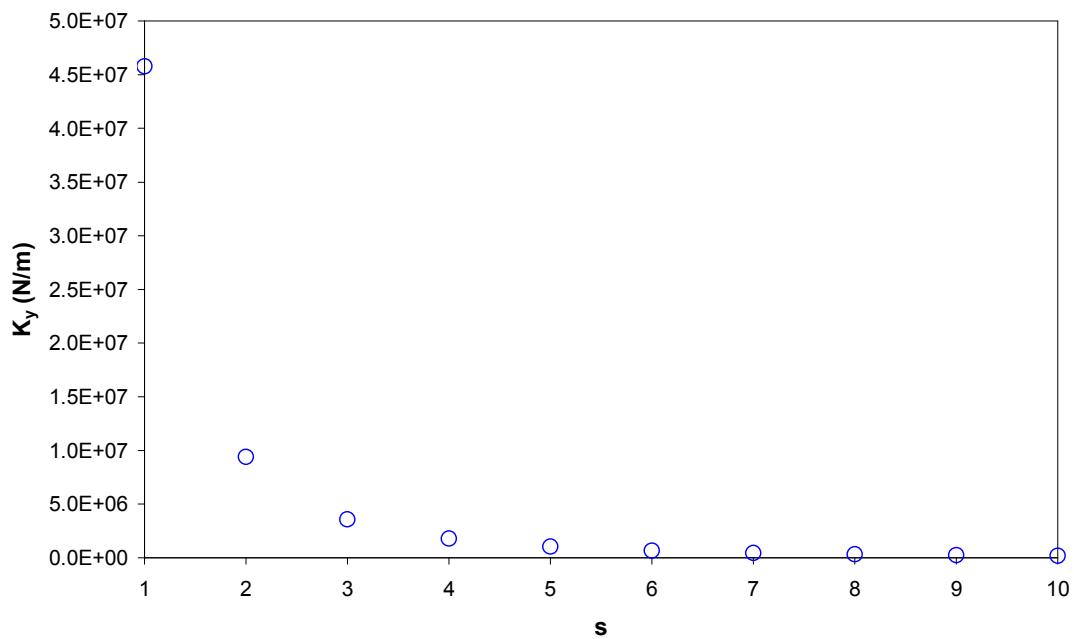


Figure 6-11 - Plot of K_y vs s for a circular flexure hinge with $E=72\text{GPa}$, $G=27\text{GPa}$, $b=11.7\text{mm}$, $t=0.5\text{mm}$, $R=0.5-5\text{mm}$.

From Figure 6-10 and Figure 6-11 it can clearly be seen that minimising s will maximise both K_x and K_y . To do this either t can be increased or R can be reduced.

However, the rotation limit, $\Delta\theta_{\text{limit}}$, of the hinge must also be taken into consideration. The required rotation, $\Delta\theta_{\text{max}}$, of the hinge is a constraint on the hinge design. Therefore the relationship between R, t and $\Delta\theta_{\text{limit}}$ must also be considered.

[Zou, 2000] presented a design control equation relating hinge design to $\Delta\theta_{\text{limit}}$, which is given in equation (6.7).

$$\Delta\theta_{\text{limit}} \leq \frac{bt^2}{6K_b} [\sigma] \quad (6.7)$$

where $[\sigma]$ is the maximum allowable stress, given by equation (6.8).

$$[\sigma] = \frac{\sigma_p}{n} \quad (6.8)$$

where σ_p is the material's proportional limit and n is a factor of safety (in this study, n=2).

Combining equations (6.3) and (6.7) gives equation (6.9).

$$\Delta\theta_{\text{limit}} = \frac{2\sigma}{Es^2} \left[\frac{2s^3(6s^2 + 4s + 1)}{(2s + 1)(4s + 1)^2} + \frac{12s^4(2s + 1)}{(4s + 1)^{5/2}} \arctan \sqrt{4s + 1} \right] \quad (6.9)$$

Inspection of equation (6.9) reveals that $\Delta\theta_{\text{limit}}$ is also a function of s only. A plot of $\Delta\theta_{\text{limit}}$ versus s is given in Figure 6-12.

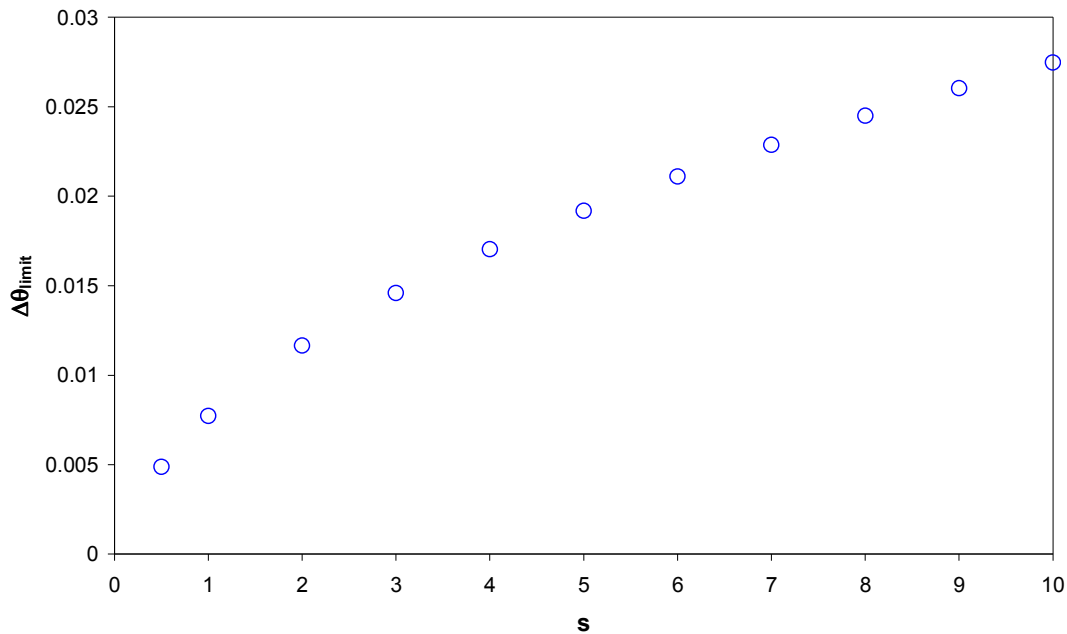


Figure 6-12 - Plot of $\Delta\theta_{\text{limit}}$ vs s for a circular flexure hinge with $E=72\text{GPa}$, $G=27\text{GPa}$, $b=11.7\text{mm}$, $t=0.5\text{mm}$, $R=0.5\text{-}5\text{mm}$.

From Figure 6-12 it can clearly be seen that $\Delta\theta_{\text{limit}}$ decreases with decreasing s . It is thus clear that maximising K_x and K_y and maximising $\Delta\theta_{\text{limit}}$ are conflicting goals. Therefore, a compromise must be reached.

The z -axis rotation of the hinge is the dominant degree-of-freedom and therefore the choice of K_b has the most significant effect on the mechanism behaviour. Inspection of equation (6.3) reveals that K_b is a function of s and R . A plot is given in Figure 6-13 of K_b versus s . In this figure K_b is plotted for several values of R . It can be noted from equation (6.3) and Figure 6-13 that K_b is a function of R^2 and a power

of s . It can be noted from equation (6.3) that changing s has a greater impact on K_b than on K_x and K_y .

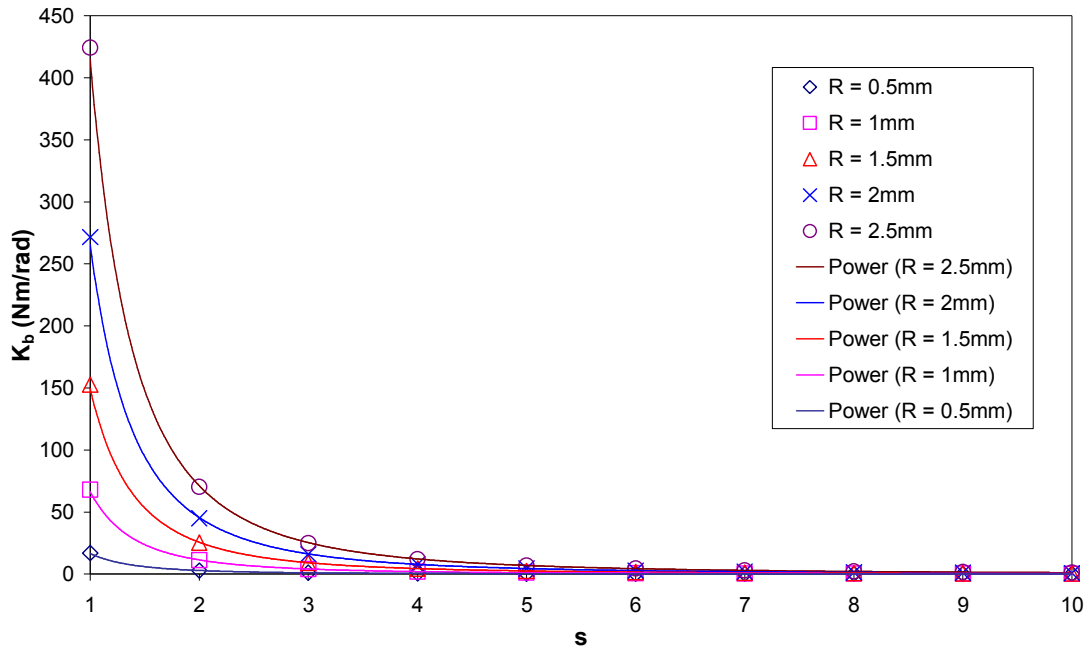


Figure 6-13 - Plot of K_b vs s for a circular flexure hinge with $E=72\text{GPa}$, $G=27\text{GPa}$, $b=11.7\text{mm}$.

Changing t or R affects K_b , K_x and K_y . In a system more complex than a simple lever the effect of these changes is not so clear. To understand how changing R and t , and thus K_b , K_x and K_y , effects the 3RRR mechanism and $XY\theta_Z$ stage a parametric study of hinges A, B and C was performed using the SCHM and PRBM. The values of t and R were selected so that each plot gives s ($=R/t$) ranging from 1 to 10. The results are given in Figures 6-14 to 6-16 below. For all the plot values given below $\Delta\theta_{\text{limit}}$ for each hinge is not exceeded by the rotation of the hinge.

6.5.2 Variation of Hinge A

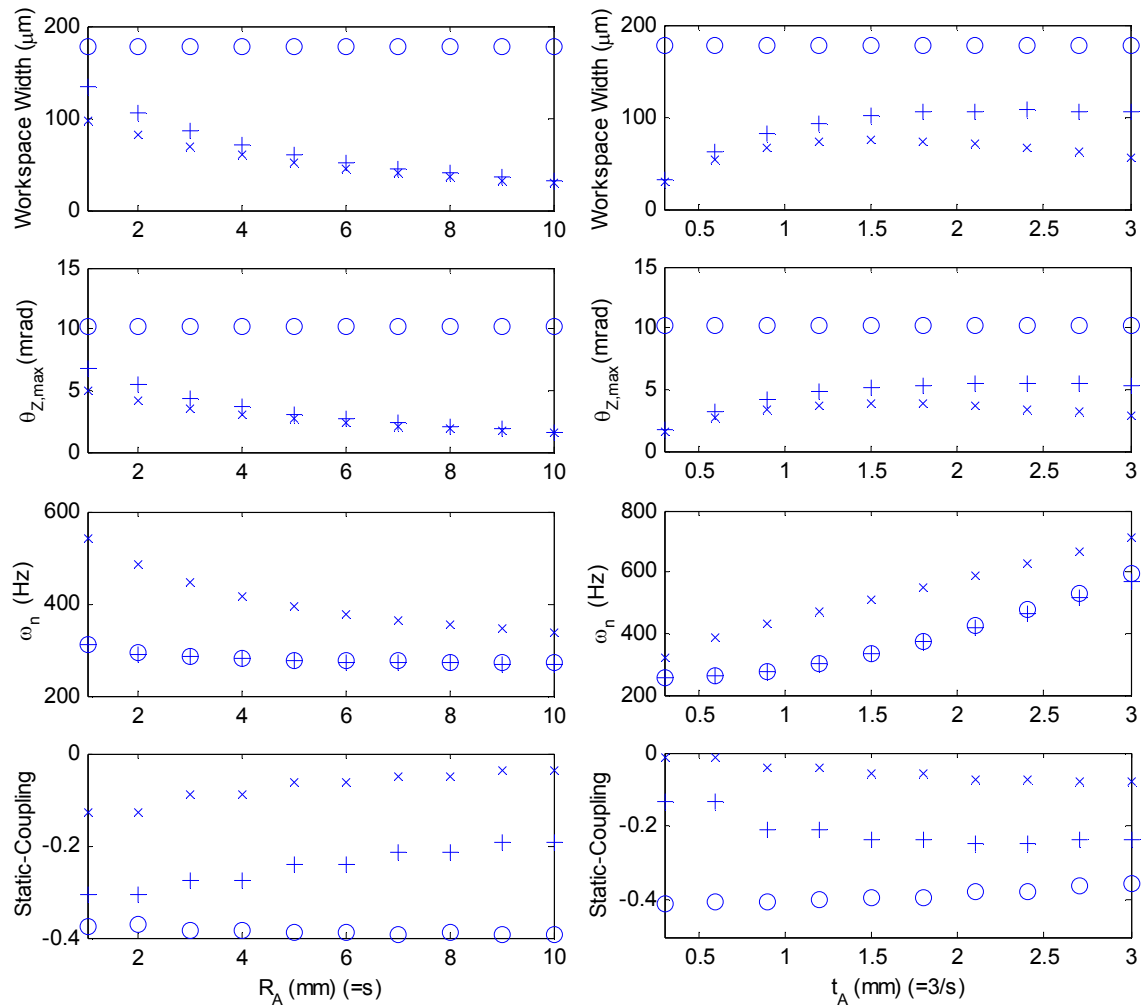


Figure 6-14 - Output characteristics for SCHM of $XY\theta_Z$ stage (+), SCHM of 3RRR (\times) and PRBM of 3RRR (O), when R_A and t_A are varied so that $s=1$ to 10. ($L_{AB}=40\text{mm}$, $L_{BC}=40\text{mm}$, $\phi_B=90^\circ$, $\phi_C=40^\circ$, $R_o=3.5\text{mm}$, $t_{B,C}=1\text{mm}$, $R_{B,C}=3\text{mm}$).

Workspace width and maximum rotation, $\theta_{Z,\max}$

The SCHM and PRBM predict very different results. The PRBM of the 3RRR does not predict any change of workspace width or $\theta_{Z,\max}$ with either changing R_A or t_A .

The SCHM of the 3RRR and $XY\theta_Z$ stage predict a significant non-linear change of both workspace width and $\theta_{Z,\max}$ with a change of both R_A and t_A . The SCHM of the 3RRR predicts that that decreasing s , by changing either R_A or t_A , and hence

increasing K_y and K_x , increases the workspace width and $\theta_{Z,\max}$. The SCHM of the $XY\theta_Z$ stage predict a similar result, but as t_A increases beyond a point the workspace width and $\theta_{Z,\max}$ starts to decrease.

Natural Frequency, ω_n

All models predict that reducing R_A or increasing t_A will increase the ω_n .

Static-Coupling

All models predict that changing t_A or R_A has a minor effect on the static-coupling.

6.5.3 Variation of Hinge B

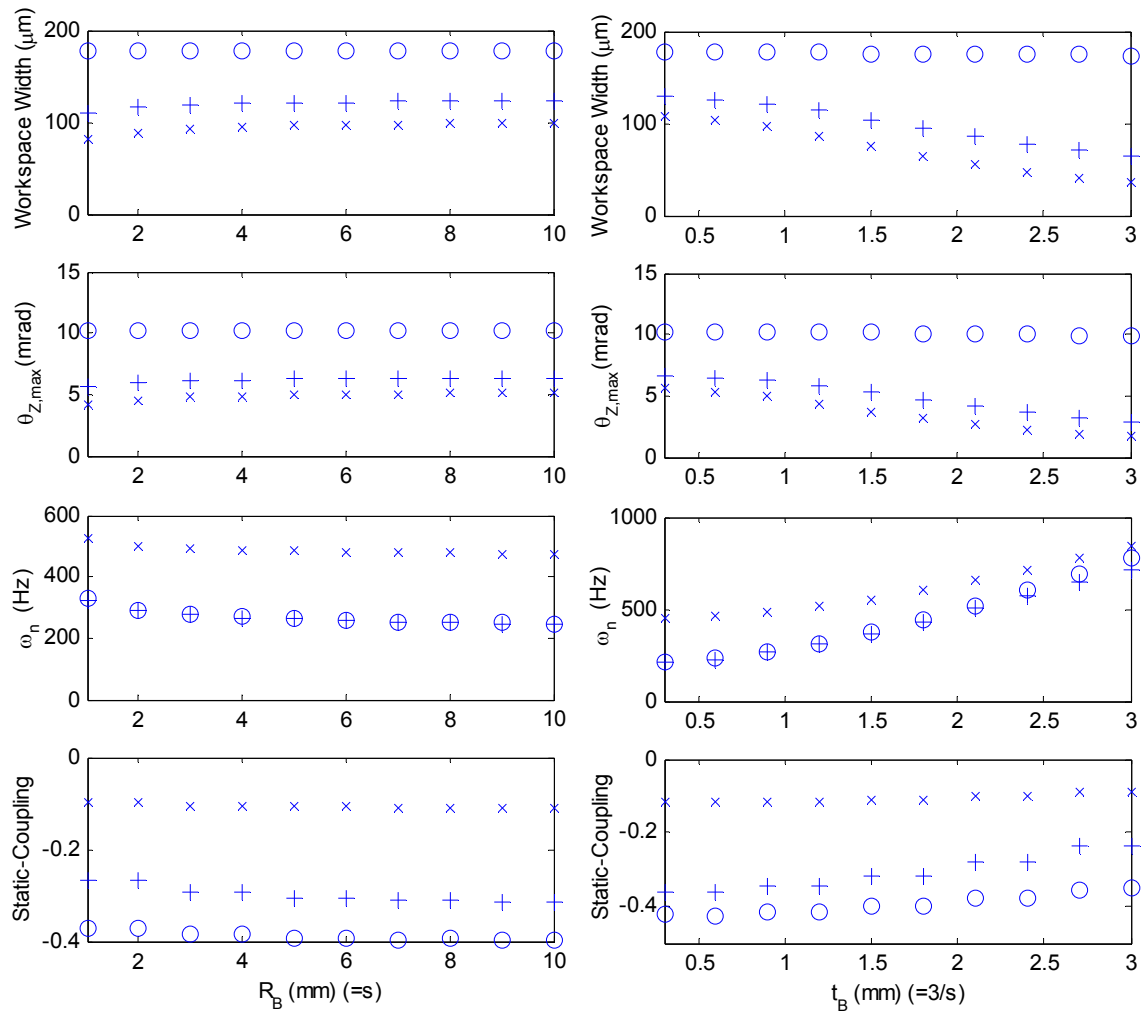


Figure 6-15 - Output characteristics for SCHM of $XY\theta_Z$ stage (+), SCHM of 3RRR (\times) and PRBM of 3RRR (O), when R_B and t_B are varied so that $s=1$ to 10. ($L_{AB}=40\text{mm}$, $L_{BC}=40\text{mm}$, $\phi_B=90^\circ$, $\phi_C=40^\circ$, $R_o=3.5\text{mm}$, $t_{A,C}=1\text{mm}$, $R_{A,C}=3\text{mm}$).

Workspace width and maximum rotation, $\theta_{Z,\max}$

The SCHM and PRBM predict very different results. The PRBM of the 3RRR does not predict any change of workspace width or $\theta_{Z,\max}$ with either changing R_B or t_B .

The SCHM of the 3RRR and the $XY\theta_Z$ stage predicts a minor increase of workspace width and $\theta_{Z,\max}$ with an increase of R_B and a significant decrease of workspace width and $\theta_{Z,\max}$ with an increase of t_B .

Natural Frequency, ω_n

All models predict that reducing R_B or increasing t_B will increase the ω_n .

Static-Coupling

All models predict that changing t_B or R_B has a minor effect on the static-coupling.

6.5.4 Variation of Hinge C

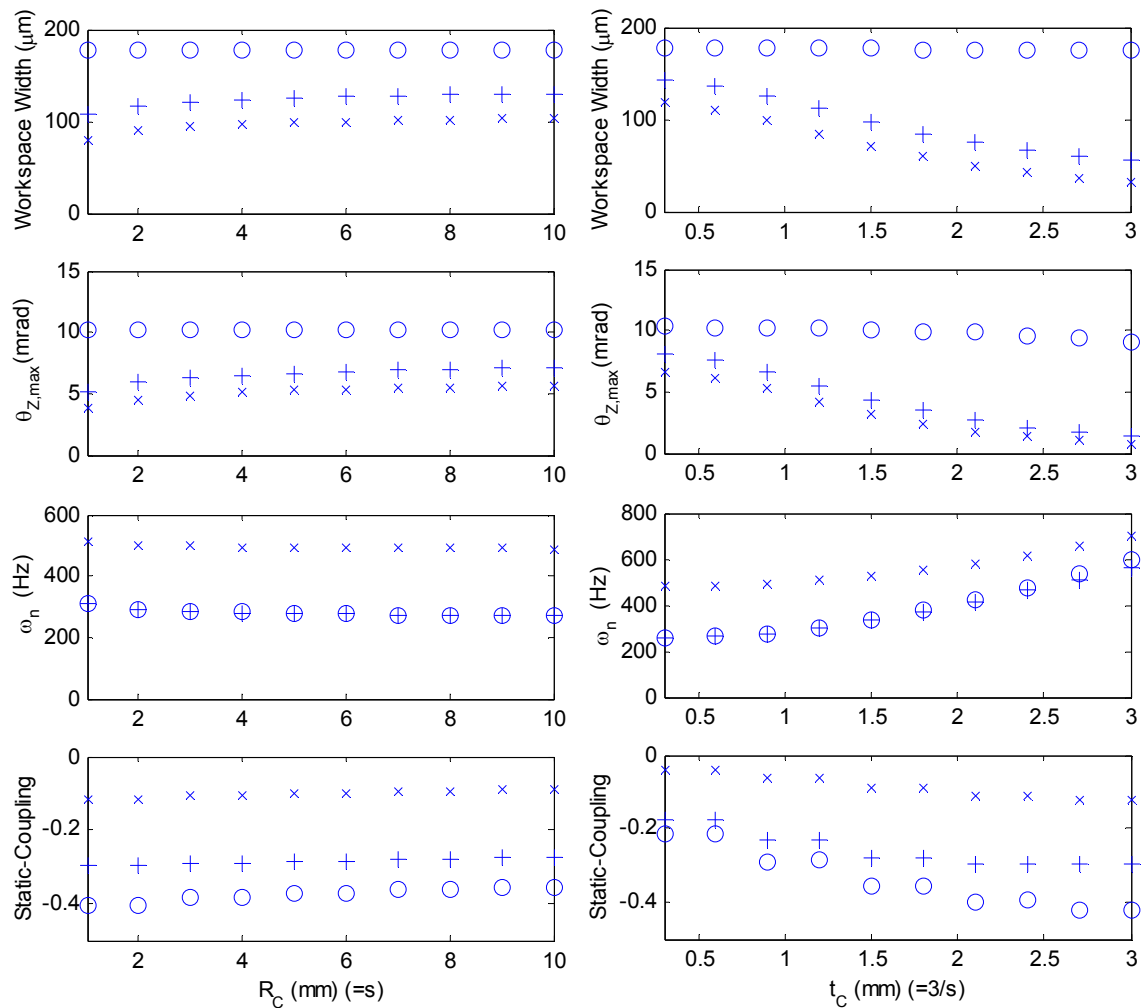


Figure 6-16 - Output characteristics for SCHM of $XY\theta_Z$ stage (+), SCHM of 3RRR (\times) and PRBM of 3RRR (O), when R_C and t_C are varied so that $s=1$ to 10. ($L_{AB}=40\text{mm}$, $L_{BC}=40\text{mm}$, $\phi_B=90^\circ$, $\phi_C=40^\circ$, $R_o=3.5\text{mm}$, $t_{A,B}=1\text{mm}$, $R_{A,B}=3\text{mm}$).

Workspace width and maximum rotation, $\theta_{Z,\max}$

The SCHM and PRBM predict very different results. The PRBM of the 3RRR does not predict any change of workspace width or $\theta_{Z,\max}$ with either changing R_C or t_C .

The SCHM of the 3RRR and the $XY\theta_Z$ stage predicts a minor increase of workspace width and $\theta_{Z,\max}$ with an increase of R_C and a significant decrease of workspace width and $\theta_{Z,\max}$ with an increase of t_C .

Natural Frequency, ω_n

All models predict that reducing R_C or increasing t_C will increase the ω_n .

Static-Coupling

All models predict that changing t_C or R_C has a minor effect on the static-coupling.

6.5.5 Discussion

Inspection of Figures 6-14 to 6-16 reveals that the SCHM and PRBM give very different predictions of some output characteristics. As expected, the PRBM does not indicate any affects on the workspace width or maximum rotation, $\theta_{Z,max}$, caused by changes in hinge parameter, as the PRBM models the flexure hinges as purely rotational joints. However, the SCHM predicts that changing some hinge parameters has a significant affect on the workspace width and maximum rotation, $\theta_{Z,max}$, as this model does consider the effects of translational compliances in the flexure hinges. These results highlight the limited usefulness of a PRBM to model the 3RRR compliant mechanism kinematic behaviour. If the SCHM is demonstrated to be accurate, as suggested by the results from Chapter 4, then it should be used in parametric study and optimisation.

The predictions for the natural frequency, ω_n , given by the SCHM and PRBM are almost identical for all hinge parameter variations. Therefore, if the only output characteristic of concern is the natural frequency, then either the SCHM or PRBM may be used.

For most hinge parameter variations the SCHM of the $XY\theta_Z$ and the SCHM of the 3RRR predict similar changes, but the magnitude of workspace width, maximum rotation, $\theta_{Z,\max}$, and static-coupling is significantly less for the $XY\theta_Z$, while the prediction of natural frequency, ω_n , is significantly greater for the $XY\theta_Z$. The SCHM of the 3RRR and $XY\theta_Z$ stage predict that the hinge parameters of hinge A, B and C all have a significant effect on the output characteristics.

The relationship between the hinge parameters and the output is not easily explained, as the stiffness values and the geometric configuration parameters all affect the relationship. In addition the appropriate choice of hinge parameters is also constrained by the required rotation of each hinge for a given geometric configuration. Therefore it is difficult to establish any solid design rules for selecting hinge parameters. Optimisation should be used to select the best hinge parameters.

6.6 Use of the SCHM and design rules in optimisation

The design rules, outlined in section 6.4.1, were established based upon the SCHM of the $XY\theta_Z$ micro-motion stage. The results in Chapter 4 show that the SCHM of the 3RRR compliant mechanism gives very similar predictions to the 2-D FEM, which is assumed to be a reliable benchmark. Therefore, the results given by the SCHM in this parametric study will be assumed to be reliable, and, furthermore, the SCHM will be used in optimisation. The $XY\theta_Z$ stage model, including the piezo-actuator, will also be assumed to improve the prediction. The validity of this assumption will be demonstrated by experimental validation in Chapter 8.

In most situations a $XY\theta_Z$ micro-motion stage will be required to satisfy a number of requirements. These may be conflicting and a compromise will need to be met. Design optimisation is the most effective way to develop a design to meet specific requirements. The design rules that have been presented can be used to set some parameters and establish some dependent relationships between parameters. For example; if a large workspace is required, and there are no size constraints, then $\phi_B = 80^\circ - 90^\circ$ and $L_{BC} \geq L_{AB}$ should be set, $|\phi_C|$ should be maximised and R_o should be set to the minimum practical value.

The design rules also allow the initial parameters to be set to an appropriate value for the design specifications given. This will make the optimisation process faster and improve the likelihood that a global minimum is found.

The optimisation must also consider geometric size constraints, the mounting of the piezo-actuator and ensure that there is no interference between links, end-effector or piezo-actuator.

The optimisation of the $XY\theta_Z$ micro-motion stage will be discussed in the following chapter.

Chapter

7 Optimal design of the $XY\theta_Z$ micro-motion stage

In Chapters 4 and 5 a simple-compliant-hinge-model (SCHM) of the 3RRR compliant mechanism and $XY\theta_Z$ micro-motion stage were presented. In Chapter 6 the model of the $XY\theta_Z$ stage was used in a parametric study. In this chapter an optimal design procedure using the SCHM of the $XY\theta_Z$ stage will be presented. Some conclusions drawn from the parametric study will be used to simplify the optimisation and improve its efficiency. The ANSYS Design Optimisation features were used to perform this optimisation.

As a test case, a $XY\theta_Z$ stage was designed to satisfy the demands of an application in a Scanning-Electron-Microscope (SEM).

The SCHM of the optimally designed $XY\theta_Z$ stage was then compared to equivalent 2-D FEM and PRBM of the $XY\theta_Z$ stage.

7.1 $XY\theta_z$ stage specifications for SEM application

The new $XY\theta_z$ stage was designed to be used in a SEM. For this application it needs to manoeuvre a sample under the beam of the microscope with fine resolution movement in the x-y plane. This will allow the SEM to take finer resolution pictures of the sample than is currently possible. The $XY\theta_z$ stage needs to be mounted to the existing coarse motion stage inside the SEM and to fit within the size constraints imposed by the microscope. The coarse motion stage, with the size constraints marked, is shown in Figure 7-1. The system also needs to operate in a high vacuum.

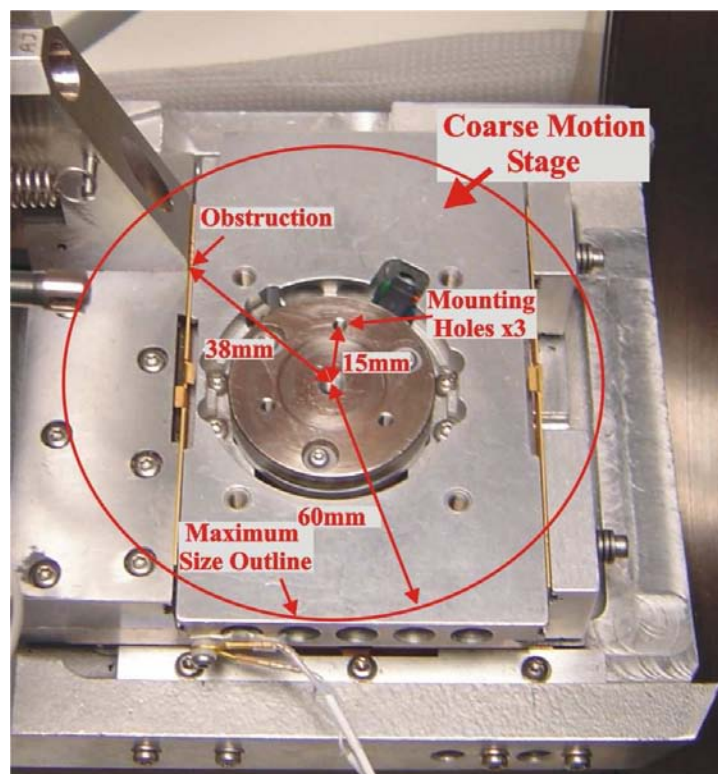


Figure 7-1 - Photo showing coarse motion stage on the tray of the SEM and size constraints for $XY\theta_z$ stage.

7.1.1 $XY\theta_Z$ stage requirements

The requirements of the $XY\theta_Z$ stage are:

- Must fit within size constraints:
 - Maximum thickness of 20mm
 - Maximum width across of 120mm as defined by the maximum size outline
 - Must allow for obstruction at one point, 38mm from centre of stage
 - End-effector must support sample holder of diameter 16mm
 - Must allow for mounting holes, three of 3mm at 15mm radius from centre

- must be vacuum compatible

Desired Performance Characteristics

- Natural frequency $>200\text{Hz}$
- Static-coupling < 0.02

Objective

- Maximise constant-orientation workspace width

It is hoped that the stage will be able to provide constant-orientation workspace width of over $100\mu\text{m}$.

7.2 $XY\theta_z$ stage components

7.2.1 Compliant mechanism

The 3RRR compliant mechanism was to be wire cut from a single piece of 12.8mm thick 7075-T6 aluminium plate. To ensure that the linkages were firmly fixed at hinge A the compliant mechanism was to be mounted on a base plate. This plate could be 6mm thick while still ensuring the required total thickness of less than 20mm.

7.2.2 Piezo-actuators

Only one model of piezo-actuator was readily available for use in this prototype and therefore the actuators were not considered as variables in the optimal design. The actuator used was the Tonkin AE0505D16 stack piezoelectric actuator, with strain gauges mounted. The properties of this actuator were given in Table 6-2 of Chapter 6.

7.2.3 Piezo-actuator preload mechanism

A new preload mechanism was designed specifically for this stage. Due to the size constraints this needed to be as compact as possible, while still providing rigid support for the piezo-actuator. The use of a screw and lock nut to provide the preload has been commonly used and was felt to be a significant improvement on the mechanism used in the first prototype. Placing the preload on the linkage would allow easy access to the screw and nut and allow the linkages and piezo-actuator to

be compactly positioned to reduce the overall size of the stage. The benefit of this preload design to reduce the size can be seen by inspection of the final stage design.

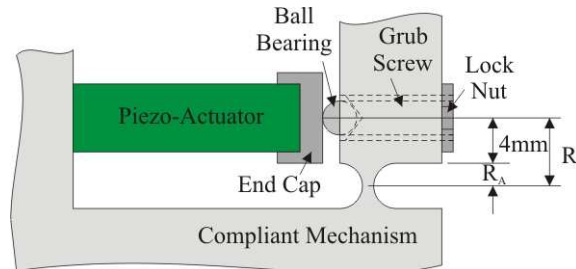


Figure 7-2 - New preload mechanism design.

7.3 Optimisation model

The SCHM of the $XY\theta_z$ stage, as presented in Chapter 5, was used in optimisation. The model parameters were the same as presented in Chapter 6. The model also incorporated a number of constraints relating to the allowable rotation of the flexure hinges, the size of the mechanism, the mounting of the piezo-actuator and interference between the links and the piezo-actuator.

7.3.1 Constraints

7.3.2 Hinge rotation

Each flexure hinge has a rotation limit, $\Delta\theta_{\text{limit}}$, which ensures the elastic yield limit of the material is not exceeded. $\Delta\theta_{\text{limit}}$ is dependent on the hinge parameters t and R , as discussed in Chapter 6. In the optimisation model a check was performed to ensure that the maximum rotation of each hinge, $\Delta\theta_{\text{max}}$, would not exceed its specified

$\Delta\theta_{\text{limit}}$. The rotation of each hinge changes depending on the position of the

The Modelling and Optimal Design of a 3-DOF $XY\theta_z$ Micro-Motion Stage

compliant mechanism. The rotation of the flexure hinges was calculated for three different positions of the mechanism, which corresponded to the extremities of the workspace and rotation. The maximum rotation experienced by each hinge in any of these positions was the $\Delta\theta_{\max}$ for that hinge. The input displacements to move the compliant mechanism into the three extreme positions are given in Table 7-1.

Because of the design of this prototype, the maximum input displacement applied to an input-link is due to the maximum displacement of the piezo-actuator, $\Delta L_{\max,load}$, and the preload mechanism. As the preload is tightened the compliant mechanism displaces. It is this displacement that generates the preload force to hold the piezo-actuator in place. The term describing this displacement is $\Delta D_{pre-load}$. The maximum displacement of the input-link, ΔD_{\max} , is given by equation (7.1).

$$\Delta D_{\max} = \Delta L_{\max,load} + \Delta D_{preload} \quad (7.1)$$

As discussed in Chapter 5, $\Delta L_{\max,load}$ is dependent on the un-loaded piezo-actuator displacement, $\Delta L_{\max,no-load}$, the stiffness of the piezo-actuator, k_p , and the stiffness of the compliant mechanism, k_{in} .

In the model the preload displacement, $\Delta D_{preload}$, was set to a value that ensures that the compliant mechanism always applies a compressive load on the piezo-actuator. The value chosen was $\Delta D_{preload}$ equals $20\mu\text{m}$. In reality, it is hard to ensure that this preload displacement is set to this specific value, and that all preload mechanisms are set evenly. This will be discussed in Chapter 8.

Mechanism Position No.	ΔD₁	ΔD₂	ΔD₃
1	ΔD _{max}	ΔD _{max}	0
2	ΔD _{max}	0	ΔD _{max}
3	ΔD _{max}	ΔD _{max}	ΔD _{max}

Table 7-1 – Inputs applied to 3RRR compliant mechanism model to check hinge rotations at extreme positions.

At each of these three extreme positions a test was performed of each hinge to ensure that $\Delta\theta_{\max}$ did not exceed $\Delta\theta_{\text{limit}}$. Equation (7.2) was used to perform this test.

$$\Delta\theta_{\text{check}(A, B \text{ or } C)} = 1 + \Delta\theta_{\text{limit}} - |\Delta\theta_{\max}| \quad (7.2)$$

$\Delta\theta_{\text{check}} > 1$ ensures that the hinge parameters are feasible.

7.3.3 Size constraints

The model included calculations for a number of critical dimension parameters, which needed to be constrained so that the optimal XYθ_Z stage would satisfy the size requirements. Figure 7-3 shows a sketch of the mechanism and the size constraints.

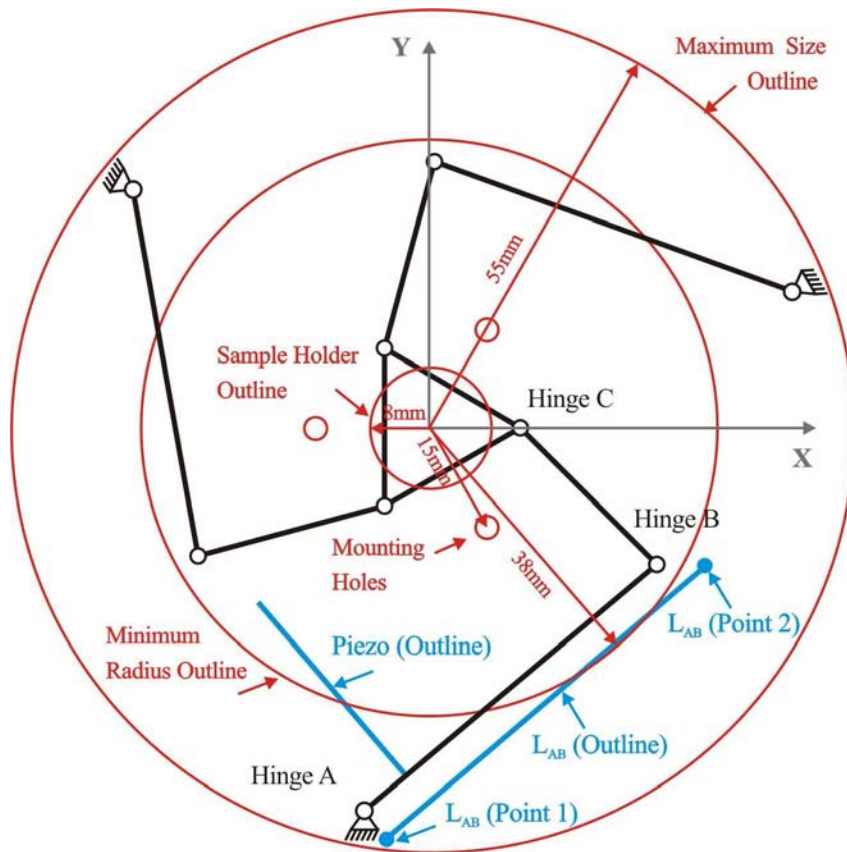


Figure 7-3 - Diagram showing the size constraints of the optimal design.

7.3.3.1 End-effector size

The end-effector must carry a sample holder of radius 8mm. Its outline is shown in Figure 7-3. The end-effector size is defined by the location of hinge C. Hinge C needs to be located so that the entire flexure hinge is clear of the sample holder. The distance from the centre of the end-effector to the centre of hinge C is denoted by C_x . To ensure that hinge C is positioned clear of the end-effector, regardless of ϕ_C , equation (7.3) is used to determine C_x .

$$C_x = 8mm + R_c + \frac{t_c}{2} \quad (7.3)$$

7.3.3.2 Maximum size

Inspection of an initial design indicated that the outer most points would occur at L_{AB} (*Point 1*) and L_{AB} (*Point 2*), as shown in Figure 7-3. Equations have been written to define the distance between the centre of the stage and each of these points. This distance is constrained to be less than 55mm, which allows for 5mm thickness of the link, so that the overall size is less than 60mm radius.

7.3.3.3 Minimum radius

It is required that the stage have one point on its outline with a radius of ≤ 38 mm. This ensures that the stage does not interfere with the obstruction shown in Figure 7-1. Investigation of an initial design shows that the minimum radius of the mechanism occurs at a point on the edge of link AB, shown as $L_{AB}(\text{Outline})$ in Figure 7-3. Inspection of Figure 7-3 indicates that a feasible design is one for which $L_{AB}(\text{Outline})$ and the *Minimum Radius Outline* intersect. An equation defining the circle-line intersection was used and an output parameter, *Min Radius*, was defined. $\text{Min Radius} \geq 0$ indicates that the $L_{AB}(\text{Outline})$ and *Minimum Radius Outline* intersect and, therefore, the design is feasible.

7.3.3.4 Piezo-actuator mounting and link interference

The model determines the required location of the piezo-actuators. This is represented with a line defining the piezo-actuator outline as shown in Figure 7-3. A test is performed to ensure that the lines representing the links and the piezo-actuator will not interfere. An output parameter *Piezo-Actuator Interfere* was defined. If the

lines do not interfere *Piezo-Actuator Interfere* is 0, if the lines do interfere *Piezo-Actuator Interfere* is 1.

7.4 ANSYS design optimisation

In the ANSYS design optimisation, design variables (DVs), state variables (SVs) and an Objective Function are defined. The DVs are the independent model parameters that are varied in order to achieve an optimal design. The upper and lower bounds of these can be set to constrain the design. The SVs are output quantities dependent on the DVs that constrain the design. The Objective Function is the output quantity to be minimised during the optimisation and is also a function of the DVs. The value of the Objective Function must be positive.

7.4.1 Design variables

The design variables are parameters of the 3RRR compliant mechanism only. As only one type of piezo-actuator was readily available this was not a variable. Using the findings from the parametric study, discussed in Chapter 6, the Design Variables were constrained to appropriate ranges. In addition R_o , as shown in Figure 7-2, was made dependent on other variables. The design variables are given in Table 7-2.

XYθ _Z Stage Design Variable	Range Constraint
Link _{AB} Length (L _{AB})	5 to 60 mm
Link _{BC} Length (L _{BC})	5 to 60 mm
φ _B	85° to 95°
φ _C	-40° to -80°
R _{A, B, C}	1 to 3 mm
t _{A, B, C}	0.5 to 2 mm

Table 7-2 - XYθ_Z stage design variables.

7.4.1.1 R_o

It was demonstrated in the parametric study that the maximum workspace width occurs when R_o is some value close to R_A. To determine the exact value requires an iterative investigation. However, the minimum practical value of R_o is dependent on R_A and the design of the piezo-actuator preload mechanism as shown in Figure 7-2. The minimum value of R_o, that is possible for the design of piezo-actuator mounting used in this prototype, is given by equation (7.4).

$$R_o = R_A + 4\text{mm} \quad (7.4)$$

This value of R_o is considerably larger than the value of R_o corresponding to the maximum workspace width in the parametric study. Therefore, the value of R_o given by equation (7.4) can be assured to give the maximum workspace width. Equation (7.4) was used to make R_o a dependent value and to ensure the workspace was maximised.

7.4.2 State variables

The state variables are the performance characteristics of the XYθ_Z stage. The state variables are given in Table 7-3 below.

XYθ _Z Stage State Variables	Constraint
Natural Frequency, ω_n	>200Hz
Static-Coupling	<0.02
Distance L _{AB} Point 1 to centre	<55mm
Distance L _{AB} Point 2 to centre	<55mm
<i>Min Radius</i>	≥ 0
<i>Piezo-Actuator Interfere</i>	=0
$\Delta\theta_{\text{check (A, B,C) for all 3 positions}}$	<1

Table 7-3 - XYθ_Z stage state variables.

7.4.3 Objective function

It was desired that the constant-orientation workspace width be as large as possible. Therefore, the objective function given by equation (7.5) was used. This function was to be minimised.

$$\text{Objective Function} = 1000 - \text{Constant-Orientation Workspace Width} \quad (7.5)$$

7.5 Optimisation method

ANSYS offers two optimisation methods, the *Subproblem Approximation Method* and the *First Order Method*. The Subproblem Approximation Method is an advanced zero-order method which uses curve fitting to the dependent variables (the SVs and

the objective function). The Subproblem Approximation Method is a quick method. However, it only minimises an approximation of the objective function and not the actual objective function. The First Order Method uses the derivatives of the dependent variables with respect to the design variables. It is highly accurate but can be computationally intense. For both methods the program performs a series of analysis-evaluation-modification cycles. An analysis of the initial design is performed, the results are evaluated against specified design criteria, and the design is modified as necessary. This process is repeated until all specified criteria are met. A design set is returned for each cycle which indicates if the design is feasible or not.

Both of these methods were used in the design optimisation of the $XY\theta_Z$ stage. The Subproblem Approximation Method was used first, to quickly search the entire design space to find design sets close to the global minimum. The optimum design set found using this method was then used to give the initial values for the First Order Method, which could then more accurately determine the optimal design.

7.6 Optimal design results

The optimal design set returned from the optimisation process is given in Table 7-4.

$XY\theta_Z$ Stage Design Variable	Optimal Design Value
Link_{AB} Length (L_{AB})	49 mm
Link_{BC} Length (L_{BC})	27 mm
ϕ_B	90°
ϕ_C	-77°
R_A	1.1 mm
t_A	0.84 mm

R_B	1.87 mm
t_B	0.7mm
R_C	3 mm
t_C	0.5mm
Values not determined using Optimisation	
R_o	5.1mm
C_x	11.25mm

Table 7-4 - $XY\theta_z$ stage optimal design variables.

The state variables corresponding to this design set are given in Table 7-5.

$XY\theta_z$ Stage State Variables	Optimal Design Value
Natural Frequency, ω_n	641Hz
Static Coupling	0.014
Distance L_{AB} Point 1 to centre	51.9mm
Distance L_{AB} Point 2 to centre	39.0mm
<i>Min Radius</i>	1.88e-7
<i>Piezo-Actuator Interfere</i>	0
$\Delta\theta_{\text{check (A, B and C) for all 3 positions}}$	≥ 1.0

Table 7-5 - $XY\theta_z$ stage optimal state variables.

The value returned for the objective function was 891.1. This gives a maximum constant-orientation workspace of $108.9\mu\text{m}$.

This optimal design satisfies all the constraints and provides all desired performance characteristics.

7.7 The second prototype optimal design

The optimal design parameters were used in the design of a 3RRR compliant mechanism prototype. The 3RRR compliant mechanism as shown in Figure 7-4 was

wire cut from a 12.8mm thick 7075-T6 aluminium plate. This compliant mechanism was designed to be bolted to a base plate, which provided a rigid fixture for hinge A, at the base of each linkage, as shown in Figure 7-5. The preload mechanism as shown in Figure 7-2 was used.

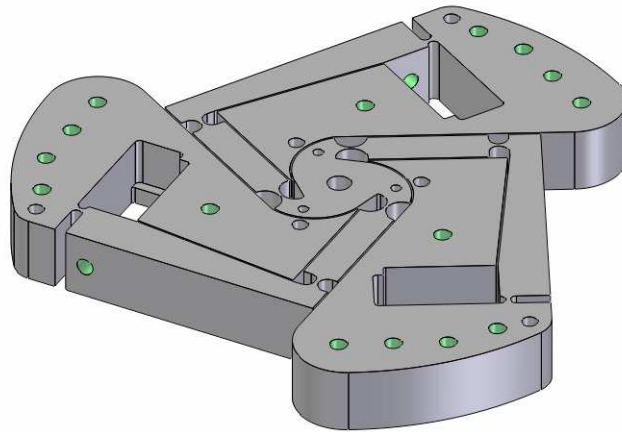


Figure 7-4 - Diagram of optimal design 3RRR compliant mechanism prototype for SEM application.

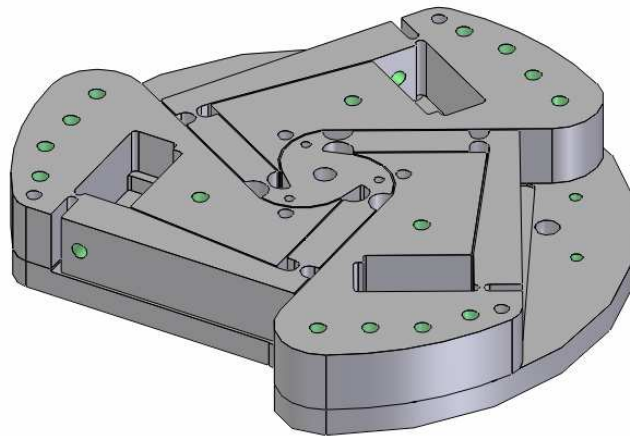


Figure 7-5 - Diagram of optimal design 3RRR compliant mechanism prototype and base plate.

The piezo-actuators and preload mechanism were assembled into the 3RRR compliant mechanism to complete the second prototype $XY\theta_z$ stage, as shown in

Figure 7-6. This prototype was then used in verification experiments as discussed in Chapter 8.

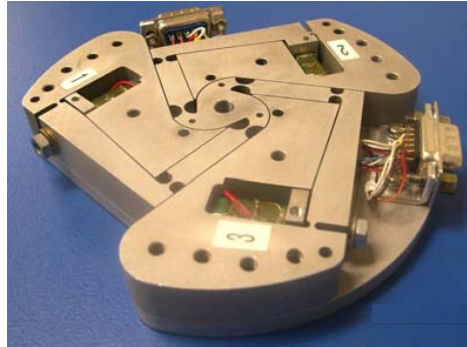


Figure 7-6 - Photograph of assembled the second prototype $XY\theta_z$ stage.

The completed stage was tested in the SEM to ensure that it met the size constraints and was vacuum compatible. Figures 7-7 and 7-8 show photographs of the stage assembled into the SEM. It can be seen that the stage fits nicely. It was also found to work satisfactorily in a high vacuum.



Figure 7-7 - Photograph of the second prototype $XY\theta_z$ stage mounted on tray of SEM.

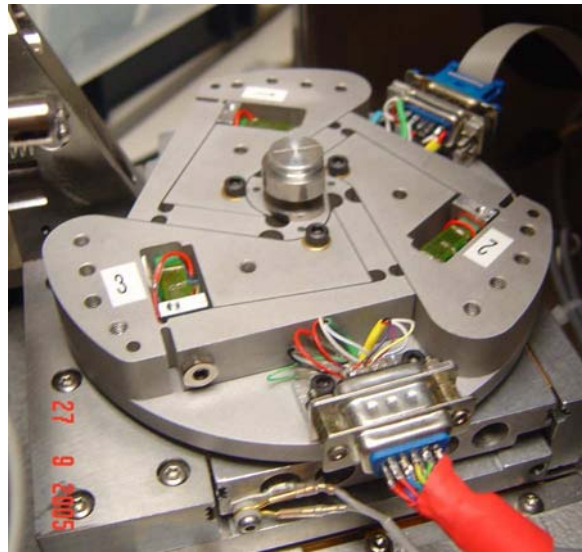


Figure 7-8 – Close-up photograph of the second prototype $XY\theta_z$ stage mounted on tray of SEM.

7.7.1 Manufacturing error

The optimal design specifications require that R_o be equal to 5.1mm for each of the three input-links. Unfortunately, a manufacturing error was found. One input-link had R_o of 5.6mm. This link was designated to be input-link 1. All models of the optimally designed the second prototype had to be modified to take this manufacturing error into consideration. Due to this manufacturing error the $XY\theta_z$ stage is no longer symmetrical. The model and experimental results clearly show the impact of this. The results presented are, therefore, sub-optimal.

7.8 Comparison of 2-D FEM, SCHM and PRBM of optimal design

A 2-D FEM and a PRBM of the optimal design were also constructed and compared to the SCHM. The modelling methods used were the same as discussed in Chapters 4 and 5. The 3RRR compliant mechanism and the $XY\theta_z$ stage models are both

compared. The Jacobian of the 3RRR complaint mechanism; the workspace width and rotation of the $XY\theta_Z$ stage; the natural frequency of the 3RRR complaint mechanism and $XY\theta_Z$ stage; and the static coupling of the 3RRR complaint mechanism and $XY\theta_Z$ stage are all derived and compared.

7.8.1 SCHM using FEA flexure hinge stiffness terms

The SCHM used in the optimisation uses the analytical equations presented in Chapter 4 to predict the stiffness of the flexure hinges. A SCHM was also derived that uses hinge stiffness terms that were determined from an FEA of the flexure hinges.

The accuracy of the flexure hinge stiffness prediction has a noticeable effect on the model performance. The optimal SCHM model uses values for K_x , K_y and K_b calculated using the analytical equations presented by Paros-Weisbord, Wu and Lobontiu. The values given by these equations, $K_{\text{Analytical}}$, are shown in Table 7-6. A 2-D finite element analysis (FEA) of the hinge geometry used in the optimal design was conducted and the results, K_{FEA} , are shown in Table 7-6. The percentage difference between the analytical equations and the FEA is given in Table 7-6. It can be seen that there is a significant difference in the flexure hinge bending stiffness, K_b , predicted by these two methods, while K_x and K_y are in closer agreement. K_b and K_x were calculated using equations (4.1) and (4.2), respectively. K_y was calculated using equations (4.7), (4.10) and (4.11). The FEA stiffness values, K_{FEA} , were also

used in the SCHM and the results compared to the model using the analytical stiffness equations.

Hinge	Hinge Parameters t (mm) R (mm)		Analytical Equations, $K_{\text{Analytical}}$			ANSYS 2-D FEA, K_{FEA}			% diff.		
			K_b (Nm/rad)	K_x (N/m)	K_y (N/m)	K_b (Nm/rad)	K_x (N/m)	K_y (N/m)	K_b	K_x	K_y
A	0.84	1.11	44.4	4.9e8	8.4e7	34.5	4.9e8	8.5e7	-29.0	0.0	0.3
B	0.7	1.87	20.5	2.9e8	3.5e7	17.7	2.7e8	3.3e7	-15.9	-5.1	-6.4
C	0.5	3	6.8	1.7e8	1.2e7	6.3	1.5e8	1.1e7	-7.8	-6.8	-13.2

Table 7-6- Flexure hinge stiffness terms, used in the SCHM, determined from a 2-D FEA and from the analytical equations, and the percentage relative difference compared to the 2-D FEA.

7.8.2 Jacobians of the optimally designed 3RRR compliant mechanism

The Jacobians derived for the models are shown below. The Jacobians derived by the 2-D FEM, the SCHM and the PRBM are shown in Tables 7-7 and 7-8. In Table 7-8 the percentage relative difference between the SCHM and PRBM compared to the 2-D FEM is also given.

2-D FEM		
3.98	1.27	-5.55
3.63	-5.71	1.77
-227.9	-248.1	-247.1

Table 7-7- Jacobian of the second prototype determined using the 2-D FEM.

SCHM						PRBM					
$K_{\text{analytical}}$			K_{FEA}			$K_{\text{analytical}}$			K_{FEA}		
3.87	1.22	-5.41	3.91	1.24	-5.49	4.07	1.30	-5.75	4.07	1.30	-5.75
3.53	-5.54	1.72	3.58	-5.62	1.74	3.71	-5.90	1.83	3.71	-5.90	1.83
-224.	-243.7	-243.7	-228.1	-247.7	-247.7	-236.6	-259.6	-259.6	-236.6	-259.6	-259.6
% diff. to 2-D FEM			% diff. to 2-D FEM			% diff. to 2-D FEM			% diff. to 2-D FEM		
2.9	3.7	2.7	1.7	1.6	1.2	-2.2	-2.6	-3.6	-2.2	-2.6	-3.6
2.9	3.0	3.0	1.4	1.6	2.0	-2.2	-3.3	-3.1	-2.2	-3.3	-3.1
1.4	1.8	1.4	-0.1	0.2	-0.2	-3.8	-4.6	-5.1	-3.8	-4.6	-5.1

Table 7-8- Jacobians of the second prototype determined using the SCHM and PRBM, and the percentage relative difference compared to the 2-D FEM.

All the Jacobians clearly indicate the impact of the manufacturing error. The rotational terms, which are given in the bottom row of the Jacobian matrix, are no longer equal and the Jacobian terms corresponding to input-link 1, the first row, have been reduced. It can be seen from the results in Table 7-8 that the SCHM using $K_{\text{analytical}}$ gives a Jacobian within 3.7% of 2-D FEM Jacobian. The SCHM using K_{FEA} gives a prediction even closer to the 2-D FEM, within 1.7%. Interestingly, for this configuration of 3RRR compliant mechanism the PRBM also gives a prediction close to the 2-D FEM, within 5.1%. It is worth comparing this result to the first prototype Jacobian predictions, given in Chapter 4, Table 4-12. For the first prototype configuration the PRBM prediction was over 40% different to the 2-D FEM. The PRBM Jacobian is not affected by the value of K_b .

7.8.3 Stiffness of the optimally designed 3RRR compliant mechanism and piezo-actuator displacement under load

The stiffness, k_{in} , of the optimally design 3RRR compliant mechanism predicted by the 2-D FEM, SCHM and PRBM is given in Table 7-9.

Using these values of k_{in} , the un-loaded piezo-actuator displacement, $\Delta L_{max,no-load}$, the stiffness of the piezo-actuator, k_p , and Equation (5.2), the piezo-actuator displacements under load are predicted, as given in Table 7-10. As the 3RRR compliant mechanism is nearly symmetrical and the same type of piezo-actuators are used, all three piezo-actuators have the same maximum displacement $\Delta L_{max,load}$.

Stiffness	2-D FEM	SCHM			PRBM		
		$K_{analytical}$ % diff.	K_{FEA} % diff.	K_{FEA} % diff.	$K_{analytical}$ % diff.	K_{FEA} % diff.	
K_{in}	5.33e6	5.94e6 -11.6	5.17e6 3.0	6.37e6 -19.5	5.51e6 -3.5		

Table 7-9- Input stiffness of 3RRR compliant mechanism the second prototype predicted by the 2-D FEM, SCHM and PRBM, and the percentage relative difference compared to the 2-D FEM

	2-D FEM	SCHM	PRBM
k_{in} (N/m)	5.33e6	5.94e6	6.37e6
k_p (N/m)	55e6	55e6	55e6
$\Delta L_{max,no-load}$ (μm)	11.6	11.6	11.6
$\Delta L_{max,load}$ (μm)	10.6	10.5	10.4

Table 7-10 –Input stiffness of the 3RRR compliant mechanism the second prototype predicted by the 2-D FEM, SCHM and PRBM and the displacement under load of the piezo-actuator

From Table 7-9 it can be seen that the SCHM and PRBM using K_{FEA} both give a prediction of k_{in} close to the 2-D FEM, within 3.5%. The SCHM and PRBM using $K_{analytical}$ give predictions significantly different to the 2-D FEM. From Table 7-10 it can be seen that all models predict similar $\Delta L_{max,load}$, even though the k_{in} of the SCHM and PRBM was predicted using $K_{analytical}$. It is worth comparing these results with those for the first prototype compliant mechanism given in Chapter 4, Table 4-14, and Chapter 5, Table 5-2. The first prototype k_{in} is approximately twice that of the second prototype, while, the difference between the PRBM and 2-D FEM predictions for the first prototype is over 95%. The increased k_{in} of the first

The Modelling and Optimal Design of a 3-DOF XYθ_z Micro-Motion Stage

prototype significantly reduces the piezo-actuator displacement, the SCHM predicting the $\Delta L_{max,load}$ to be only $8.5\mu\text{m}$.

7.8.4 Workspace of the $XY\theta_Z$ stage

Using the method presented in Chapter 5, the reachable and maximum constant-orientation workspaces predicted by the 2-D FEM, SCHM and PRBM for the second prototype $XY\theta_Z$ stage, were plotted. These are shown in Figures 7-9 to 7-11. A comparison of the maximum constant-orientation workspace is shown in Figure 7-12. The reachable and maximum constant-orientation workspace widths predicted by the 2-D FEM, SCHM and PRBM for the second prototype $XY\theta_Z$ stage are given in Table 7-11.

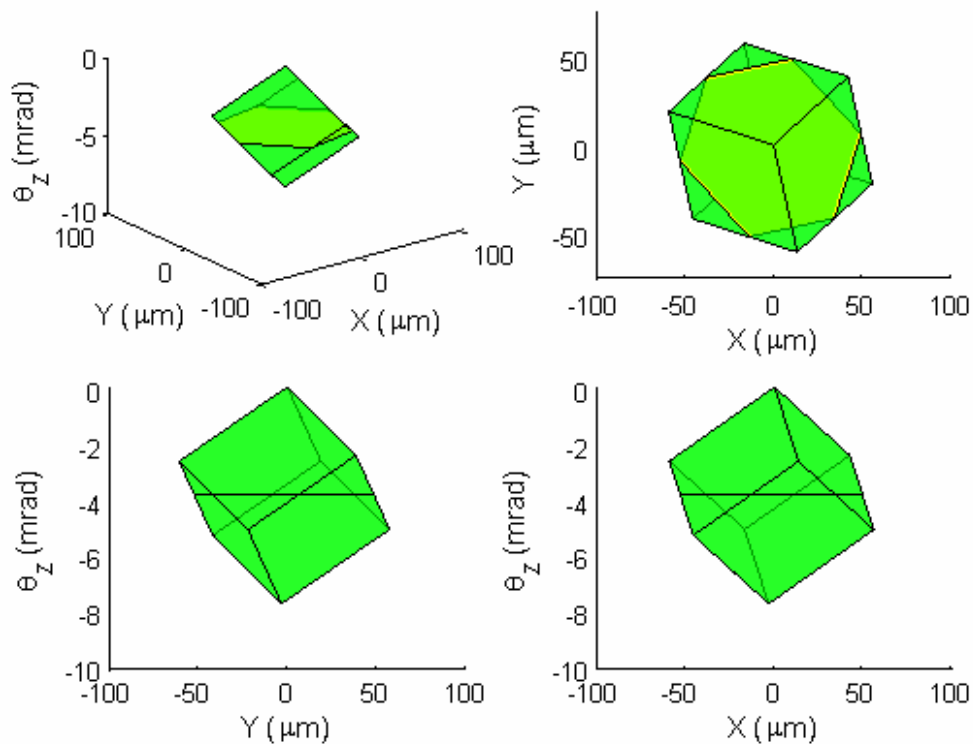


Figure 7-9 - Plots of workspace predicted by 2-D FEM of the second prototype $XY\theta_Z$ stage.

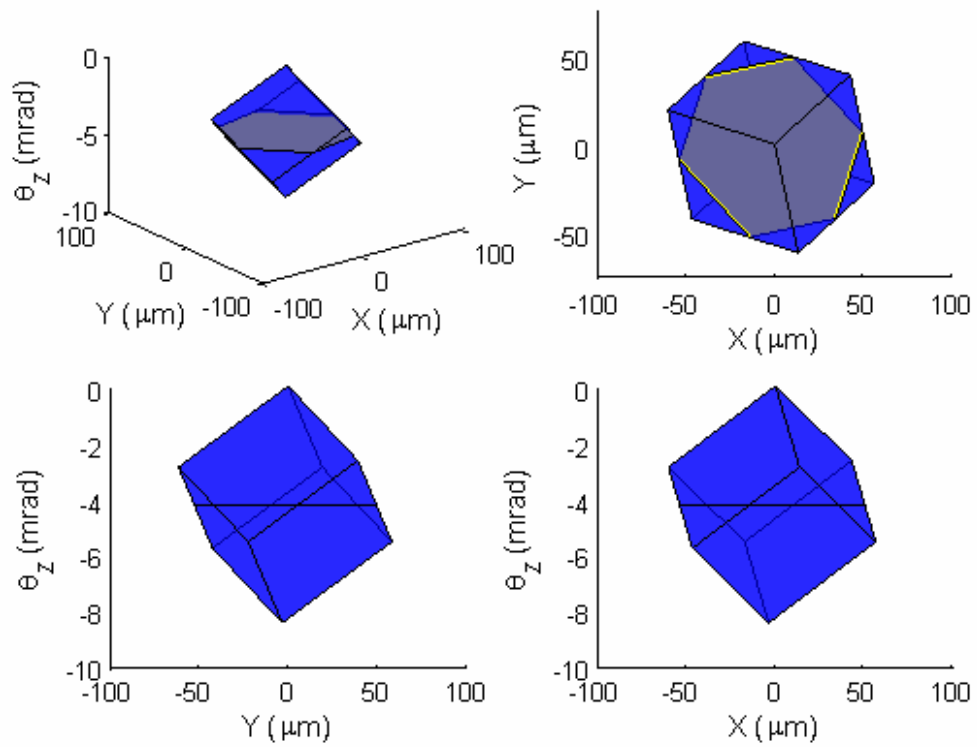


Figure 7-10 - Plots of workspace predicted by SCHM, using $K_{\text{analytical}}$, of the second prototype $XY\theta_z$ stage.

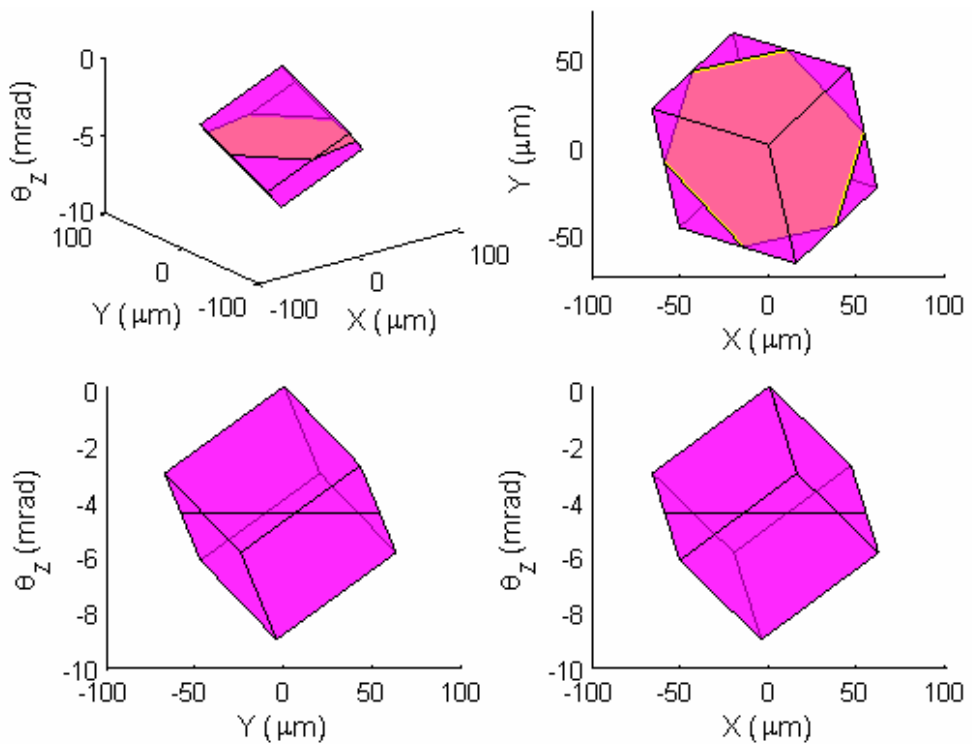


Figure 7-11 - Plots of workspace predicted by PRBM, using $K_{\text{analytical}}$, of the second prototype $XY\theta_z$ stage.

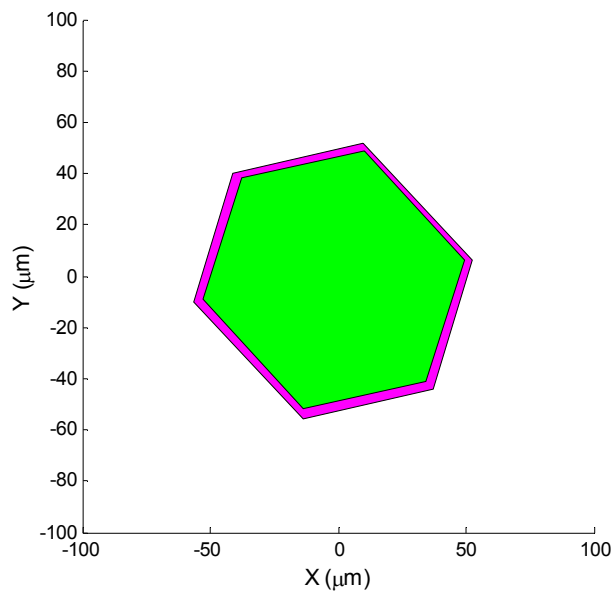


Figure 7-12 - Superimposed plots of constant orientation workspace predicted by the 2-D FEM (green), SCHM (blue) and PRBM (magenta) for the second prototype $XY\theta_z$ stage.

	2-D FEM	SCHM	% diff.	PRBM	% diff.
Reachable Workspace Width (μm)	121.6	119.9	1.4	129.9	-6.8
Maximum Constant-Orientation Workspace Width (μm)	107.3	105.9	1.3	114.9	-7.1

Table 7-11 - Reachable and constant-orientation workspace widths for the second prototype $XY\theta_z$ stage predicted by the 2-D FEM, SCHM and PRBM, and difference of SCHM and PRBM compared to the 2-D FEM.

From Figure 7-12 and Table 7-11 it can be seen that the 2-D FEM and the SCHM predict very similar workspaces, while the PRBM predicts a larger reachable and maximum constant-orientation workspace. All models predict workspaces with the same shape, proportions and orientation. It can be noted that, unlike the prototype 1 workspace given in Chapter 5, the hexagonal area of both the reachable and maximum constant-orientation workspace are not symmetrical. This is due to the manufacturing error. It can also be noted that the first prototype and the second prototype workspaces are orientated differently. This is due to a different definition

of the workspace axis. Furthermore, it can be noted that the first prototype workspace is less than half that of the second prototype.

7.8.5 Natural frequency

A modal analysis was performed in ANSYS to determine the natural frequencies of the second prototype 3RRR compliant mechanism and $XY\theta_z$ stage, predicted by the 2-D FEM, SCHM and PRBM. The 2-D FEM used the Block Lanczos mode extraction method, while the PRBM and SCHM used the reduced mode extraction method. The first three modes were determined. These modes correspond to two translational modes in the x-, y- plane and one rotational mode about the z-axis. Figures 7-13 to 7-15 show sequences of images taken from an animation, generated in ANSYS, of each mode of the 2-D FEM. Table 7-12 gives the natural frequencies of the second prototype 3RRR compliant mechanism and $XY\theta_z$ stage predicted by the 2-D FEM, SCHM and PRBM, and gives the difference of the SCHM and PRBM compared to the 2-D FEM.

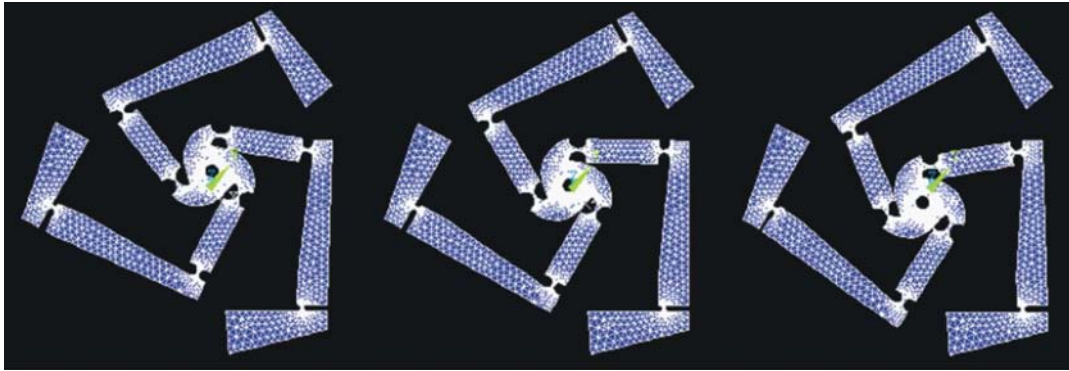


Figure 7-13 - Sequence of images from an animation generated in ANSYS of the first translational mode, 260.5Hz, of the 2-D FEM of the 3RRR compliant mechanism.

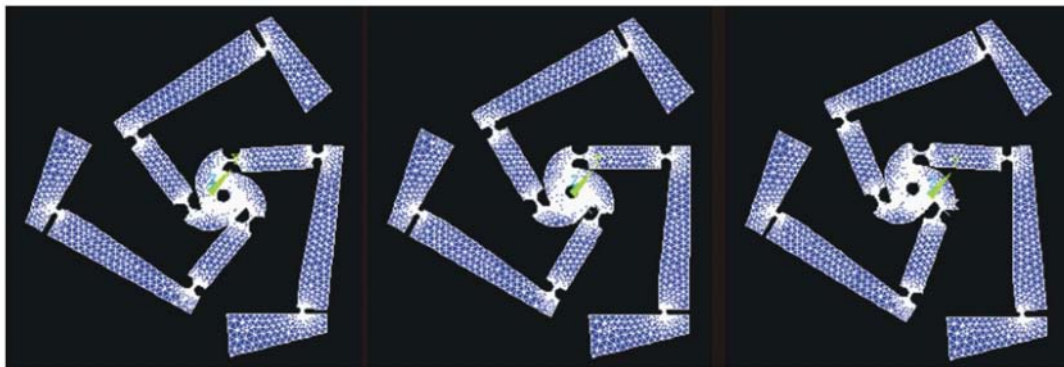


Figure 7-14 - Sequence of images from an animation generated in ANSYS of the second translational mode, 260.5Hz, of the 2-D FEM of the 3RRR compliant mechanism.

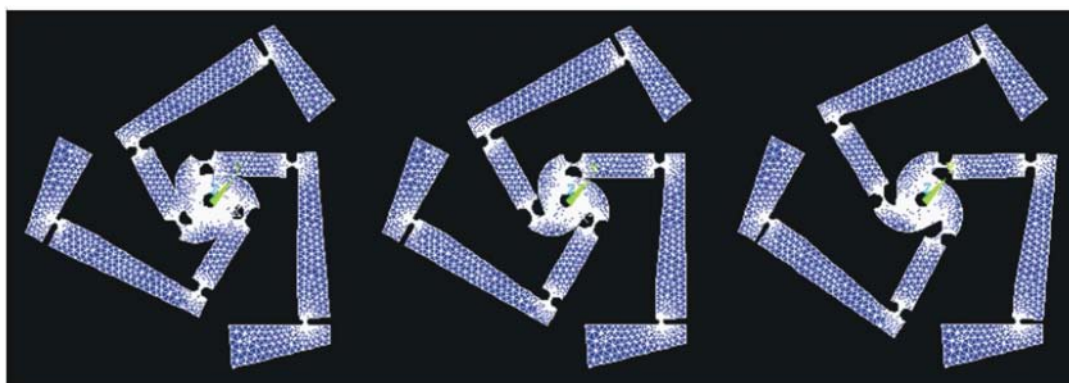


Figure 7-15 - Sequence of images from an animation generated in ANSYS of the first rotational mode, 426.9Hz, of the 2-D FEM of the 3RRR compliant mechanism.

Comparing Figures 7-13 and 7-14, the difference between the two translational modes can be observed, by noting the location of the end-effector centre relative to the origin axes. They oscillate in different directions, causing different deflection of the compliant mechanism. Both modes occur at the same frequency. This is due to the symmetry of the compliant mechanism. As the piezo-actuators are not included in this analysis the position of R_o does not affect the result and so the manufacturing error has no impact. From Figure 7-15 the rotational mode can be clearly observed.

Natural Frequencies of 3RRR Compliant Mechanism									
Mode	2-D FEM	SCHM				PRBM			
		$K_{analytical}$ %		K_{FEA} %		$K_{analytical}$ %		K_{FEA} %	
		ω_n	diff.	ω_n	diff.	ω_n	diff.	ω_n	diff.
1st translation	260.5	278.7	-7.0	256.8	1.4	281.6	-8.1	258.6	0.7
2nd translation	260.5	278.7	-7.0	256.8	1.4	281.6	-8.1	258.6	0.7
1st rotation	426.9	475.9	-11.5	448.8	-5.1	478.0	-12.0	450.0	-5.4

Natural Frequencies of XY θ_z Stage									
Mode	2-D FEM	SCHM				PRBM			
		$K_{analytical}$ %		K_{FEA} %		$K_{analytical}$ %		K_{FEA} %	
		ω_n	diff.	ω_n	diff.	ω_n	diff.	ω_n	diff.
1st translation	630.1	641.0	-1.7	633.1	-0.5	896.6	-42.3	889.9	-41.2
2nd translation	656.5	665.1	-1.3	657.6	-0.2	944.0	-43.8	937.6	-42.8
1st rotation	865.9	955.7	-10.4	943.8	-9.0	1294.4	-49.5	1284.7	-48.4

Table 7-12 - Translational and rotational mode natural frequencies in Hz of the second prototype predicted by the 2-D FEM, SCHM and PRBM, and the percentage relative difference compared to the 2-D FEM.

From Table 7-12 it can be seen that the SCHM and PRBM predict similar natural frequencies for the 3RRR compliant mechanism. Both the SCHM and PRBM give predictions close to the 2-D FEM when K_{FEA} is used, giving significantly closer predictions than when $K_{analytical}$ is used. The prediction of the rotational mode given by the SCHM and PRBM is not as close to the 2-D FEM as the translational mode prediction, which can be attributed to the inaccurate modelling of the end-effector.

Considering the model predictions for the $XY\theta_Z$ stage it can be noted that the two translational modes do not occur at the same frequency. This is due to the asymmetry introduced by the manufacturing error. Furthermore, the inclusion of the piezo-actuators causes the natural frequencies of the $XY\theta_Z$ stage to be approximately 140% more than the 3RRR compliant mechanism. The SCHM gives predictions very close to the 2-D FEM, particularly when K_{FEA} is used. However, the PRBM gives predictions very different to both the 2-D FEM and SCHM, even when K_{FEA} is used. The reason for this is unclear.

It is interesting to compare these results to those given in Chapter 4 and 5 for the first prototype 3RRR compliant mechanism and $XY\theta_Z$ stage. It can be noted that the first prototype 3RRR compliant mechanism natural frequencies are approximately 150% higher than the second prototype, while the first prototype $XY\theta_Z$ stage natural frequencies are only 60% higher than the second prototype.

7.8.6 Static-Coupling

The static-coupling for the second prototype 3RRR compliant mechanism and $XY\theta_Z$ stage predicted by the 2-D FEM, SCHM and PRBM, is given in Table 7-13.

From Table 7-13 it can be seen that for both the 3RRR compliant mechanism and $XY\theta_Z$ stage the Static-Coupling 1/2 and 3/2 are not the same. This is due to the asymmetry introduced by the manufacturing error. It can also be noted that the static-coupling of the 3RRR compliant mechanism is approximately 10 times greater than

for the $XY\theta_Z$ stage. Considering the 3RRR compliant mechanism it can be seen that the SCHM using K_{FEA} gives a prediction significantly closer to the 2-D FEM than the SCHM using $K_{analytical}$. However, the PRBM using K_{FEA} gives a prediction further from the 2-D FEM than the PRBM using $K_{analytical}$. This is unexpected, but, as the PRBM is known to be inaccurate, it is probably that the two sources of error are cancelling each other. Considering the $XY\theta_Z$ stage it can be seen that predictions of the SCHM and PRBM do not differ much regardless of whether $K_{analytical}$ or K_{FEA} is used. The SCHM gives a prediction closer to the 2-D FEM than the PRBM.

Static-Coupling of 3RRR Compliant Mechanism									
	2-D FEM	SCHM				PRBM			
		$K_{analytical}$ % diff.		K_{FEA} % diff.		$K_{analytical}$ % diff.		K_{FEA} % diff.	
Static-Coupling 1/2	-0.154	-0.131	15.2	-0.146	5.6	-0.151	2.2	-0.164	-6.0
Static-Coupling 3/2	-0.142	-0.119	16.1	-0.133	6.5	-0.137	3.7	-0.149	-5.3
Static-Coupling of $XY\theta_Z$ Stage									
	2-D FEM	SCHM				PRBM			
		$K_{analytical}$ % diff.		K_{FEA} % diff.		$K_{analytical}$ % diff.		K_{FEA} % diff.	
Static-Coupling 1/2	-0.015	-0.014	10.0	-0.014	9.6	-0.018	-18.7	-0.017	-16.0
Static-Coupling 3/2	-0.014	-0.013	10.3	-0.013	10.1	-0.016	-17.8	-0.016	-14.1

Table 7-13 - Static-coupling of 3RRR compliant mechanism and $XY\theta_Z$ stage the second prototype predicted by the 2-D FEM, SCHM and PRBM.

7.9 Discussion

The optimal design procedure was successfully applied to design a $XY\theta_Z$ stage for application in the SEM. The resulting $XY\theta_Z$ stage satisfies all the size constraints,

has a maximum constant-orientation workspace of $108.9\mu\text{m}$, a natural frequency of 630Hz and static-coupling of 0.014 . These performance characteristics exceed the desired specifications.

The optimal design $XY\theta_Z$ stage has been manufactured and assembled. The stage fits within the confines of the SEM and is vacuum compatible. However, a manufacturing error was found, which cause the $XY\theta_Z$ stage to no longer be symmetrical. The effects of this on the output characteristics have been identified. This optimal stage will from here on be referred to as the *second prototype*.

The second prototype design incorporates numerous improvements compared to the first prototype (based upon the design presented by Zou (2000)). The compliant mechanism and end-effector are made in one piece and the end-effector mass has been minimised. The thickness of the stage has been reduced significantly. The preload mechanism has been improved to provide ease of adjustment and rigid support for the piezo-actuator. Furthermore, the second prototype workspace is over twice as large as the first prototype workspace.

Another difference that can be noted is that the input stiffness of the second prototype compliant mechanism is approximately half that of the first prototype. This allows the piezo-actuator displacement to be greater, increasing the workspace. However, this also causes the natural frequency of the second prototype stage to be significantly less than the first prototype stage, even though the second prototype stage has a much lighter end-effector.

An interesting finding was that for the second prototype configuration the PRBM gives predictions of Jacobian, workspace, input stiffness, natural frequency and static-coupling close to the 2-D FEM. However, from the results given in Chapter 4 it can be seen that this result is very different to the findings for the first prototype, where it was found that the PRBM predictions were very different to the 2-D FEM. This result highlights that for some particular configurations the PRBM gives an accurate result, but for other configurations it does not. This finding agrees with the trends found in the parametric study of Chapter 6, which indicate that the PRBM gives significantly different results to the SCHM for some configurations.

Experimental validation of the first prototype and two models will be presented Chapter 8.

Chapter

8 Experimental validation of the 3RRR compliant mechanism and $XY\theta_Z$ micro-motion stage models

Previous chapters have presented theoretical modelling and optimal design of a $XY\theta_Z$ micro-motion stage. Two different 3RRR compliant mechanisms were presented to be used in the $XY\theta_Z$ micro-motion stage. The first compliant mechanism was based upon a design presented by Zou (2000). The second compliant mechanism was designed using the optimal design procedure for a specific application in a scanning electron microscope (SEM). Both of these 3RRR compliant mechanisms have been manufactured and incorporated into $XY\theta_Z$ micro-motion stage prototypes. In this chapter both of these prototypes are used to experimentally validate the modelling procedure.

8.1 Kinematic model validation

An experimental procedure was used to examine the kinematic characteristics of the 3RRR compliant mechanisms. This experiment determined the Jacobians of both the first prototype and two 3RRR compliant mechanisms. These Jacobians were compared to the 2-D FEM, SCHM and PRBM predictions. The kinematic

characteristics of the complete $XY\theta_Z$ micro-motion stage prototypes were also experimentally determined. This experiment determined the reachable and constant-orientation workspace. The workspaces were then compared to the 2-D FEM, SCHM and PRBM predictions.

8.2 Dynamic model validation

An experimental procedure was used to determine the natural frequencies and static-couplings of the 3RRR compliant mechanisms and the complete $XY\theta_Z$ micro-motion stage prototypes. These results were then compared to the model predictions given by the 2-D FEM, SCHM and PRBM.

8.3 $XY\theta_Z$ micro-motion stage prototypes

8.3.1 The first prototype

The first prototype of the $XY\theta_Z$ micro-motion stage uses a modified version of the 3RRR compliant mechanism as described by Zou (2000). The 3RRR compliant mechanism was wire-cut from 11.7mm 7075-T6 Aluminium plate and bolted to a base plate, as shown in Figure 8-1. The end-effector was made from a 6mm plate and fixed to the compliant mechanism using 3 bolts at the end of each of the 3 linkages, as shown schematically in Figure 8-1.

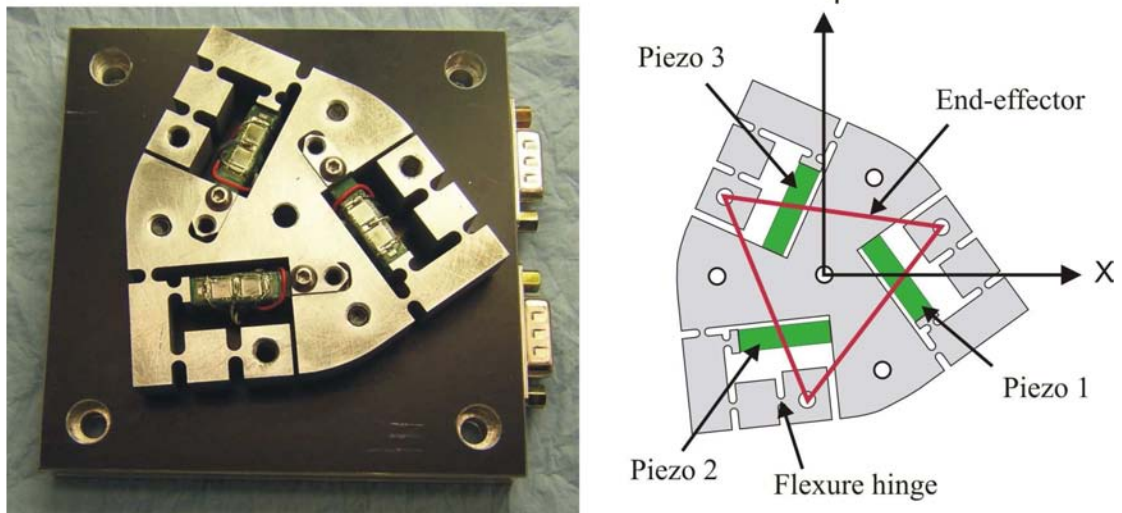


Figure 8-1 - $XY\theta_z$ micro-motion stage the first prototype, without end-effector, and schematic diagram.

Three Tokin AE0505D16 stack piezoelectric actuators were assembled into the compliant mechanism, as shown in Figure 8-1. Each piezo-actuator was held in place via a preload mechanism which applied a compressive force to the piezo-actuator. This force ensured constant contact between the piezo-actuators and compliant mechanism during operation. The original prototype presented by Zou (2000) did not allow for a preload mechanism. Preload was therefore applied by inserting metal shims at the base of each piezo-actuator as shown in Figure 8-2.

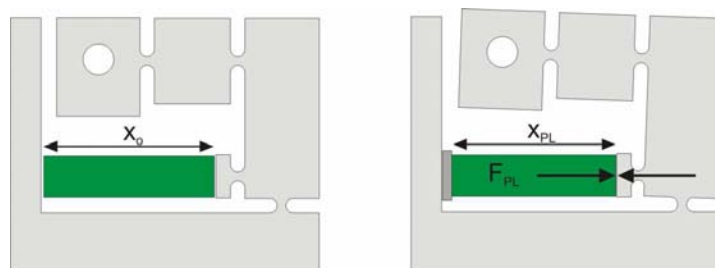


Figure 8-2 – The first prototype preload applied using metal shims.

This approach made assembly difficult and did not allow for adjustment of the preload. Due to manufacturing variations the preload is likely to be different at each piezo-actuator. To improve upon this, a new preload mechanism was designed and incorporated into the compliant mechanism. Due to the design of the compliant mechanism the preload mechanism had to be very compact and adjustable from the top. The mechanism used in the prototype is shown in Figure 8-3 and 8-4.

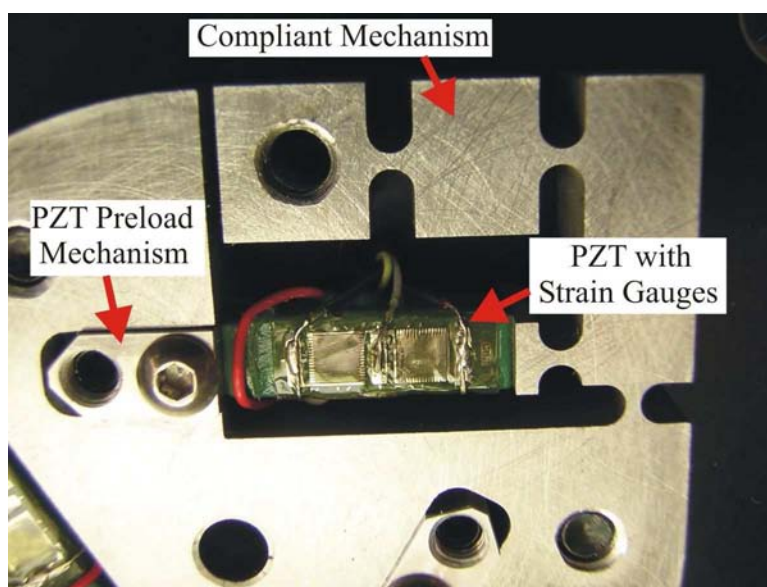


Figure 8-3 – Close-up top-view of piezo-actuator and preload mechanism used in the first prototype

This mechanism, as shown in Figure 8-4, was designed to apply a compressive force on the piezo-actuator by moving the preload block towards the piezo-actuator and compressing the piezo-actuator between the block and the compliant mechanism. This was achieved using the adjustment grub screw to force the block forward. The locking bolt was then used to lock the block in place.

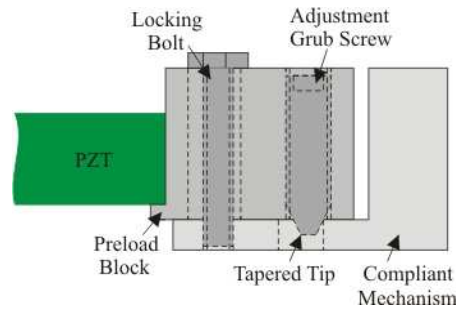


Figure 8-4 – Diagram showing side-view of the preload mechanism used in the first prototype

8.3.2 The second prototype

The second prototype $XY\theta_z$ micro-motion stage uses the 3RRR compliant mechanism designed using the optimisation procedure. The 3RRR compliant mechanism was wire-cut from 12.8mm 7075-T6 Aluminium plate and bolted to a base plate, as shown in Figure 8-5.

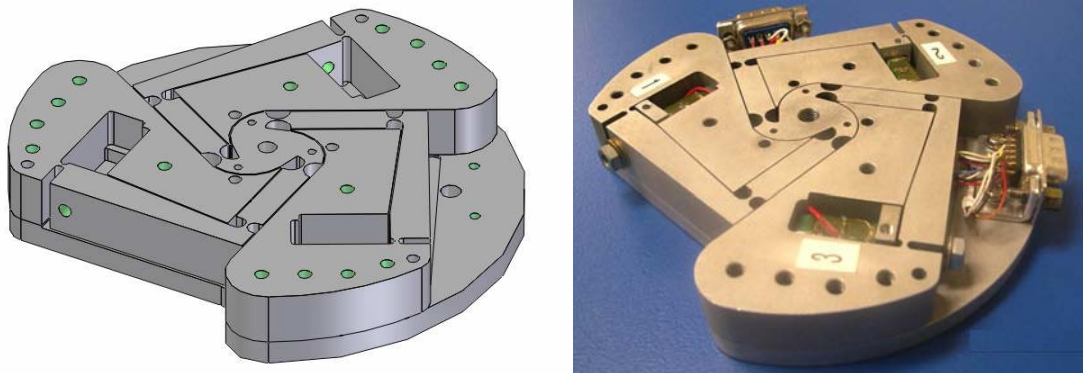


Figure 8-5 – Diagram of the second prototype 3RRR compliant mechanism (left) and photograph of the assembled $XY\theta_z$ stage (right)

Three Tokin AE0505D16 stack piezoelectric actuators were assembled into the compliant mechanism, as shown in Figure 8-5. Each piezo-actuator was held in place via a preload mechanism which applied a compressive force to the piezo-actuator. This force ensured constant contact between the piezo-actuators and compliant

mechanism during operation. A diagram of the preload mechanism is shown in Figure 8-6. It can be seen that the preload mechanism is located in the input links of the 3RRR compliant mechanism. This mechanism uses a screw to apply the preload.

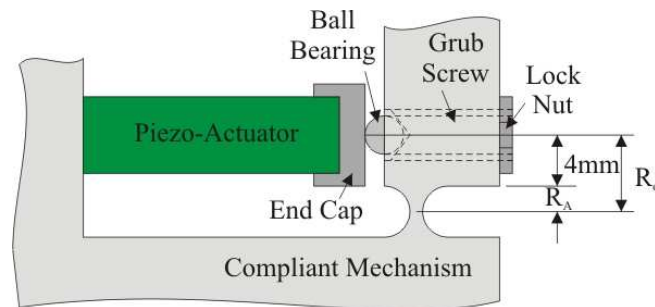


Figure 8-6 - Diagram showing top-view of the preload mechanism used in the second prototype

8.3.3 Piezo-actuator feedback and control

Each unloaded piezo-actuator is specified by the manufacturer to have a maximum displacement of $11.6 \pm 2.0 \mu\text{m}$ with a 100V input. Each of the piezo-actuators is driven by a Physik Instrumente (PI) amplifier, which can provide a DC voltage between -20V and 120V . The amplifiers have a maximum output power of 30W. Measurement Group EA-06-125TG-350 strain gauges are mounted to the piezo-actuators to determine their displacement. A full-bridge arrangement is used so that the strain gauges can be temperature compensated. All the strain gauges are connected to a strain gauge conditioner. Using feedback from these strain gauges the displacement of the piezo-actuators is controlled using closed-loop proportional-integral (PI) control. The control loop is shown in Figure 8-7.

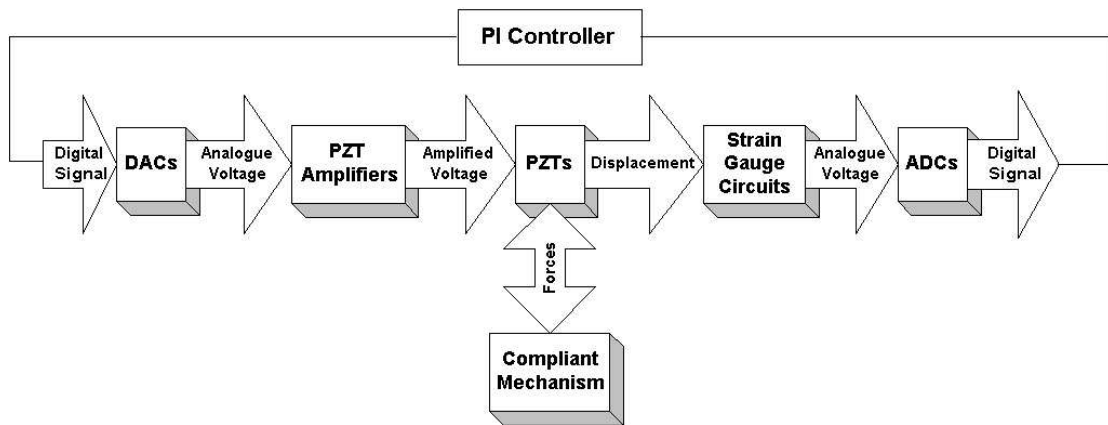


Figure 8-7 - Schematic of closed-loop PI controller using strain gauge feedback.

8.3.4 Strain gauge calibration

Strain gauges are bonded to the piezo-actuators to measure the input displacement applied to the 3RRR compliant mechanism. The strain-gauges were calibrated while the piezo-actuators were assembled into the compliant mechanism. To calibrate the strain gauges a Philtec D20 fibre-optic sensor was used. This sensor had been calibrated using a laser interferometer. A mirror was attached to the compliant mechanism, as shown in Figures 8-8 and 8-9, for the first prototype and Figures 8-10 and 8-11, for the second prototype. The fibre-optic sensor was used to measure the displacement of the mirror, as also shown in Figures 8-8 to 8-11. The fibre-optic sensor was mounted on a translation stage so that the sensor could be correctly positioned relative to the mirror, within its measurement range. The mirror was bonded to the first prototype, and attached to the second prototype via a magnet to the preload mechanism. Care was taken to ensure that the fibre-optic sensor was aligned with the axis of the preload mechanism so that the displacement measured was the displacement at the point of piezo-actuator force input.

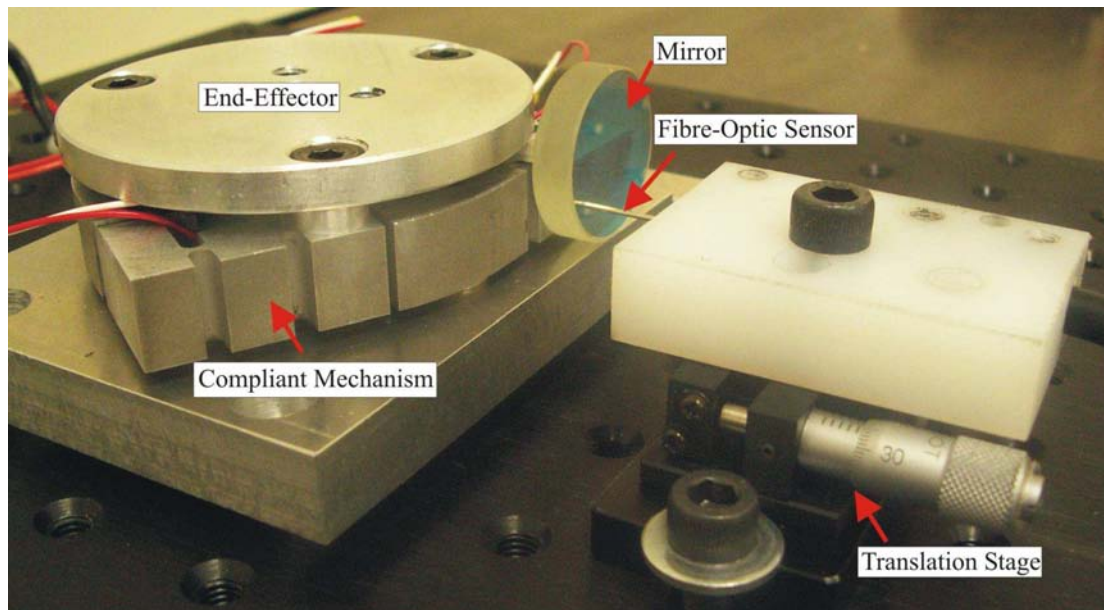


Figure 8-8 - Photograph showing the set-up used for strain gauge calibration of the first prototype.

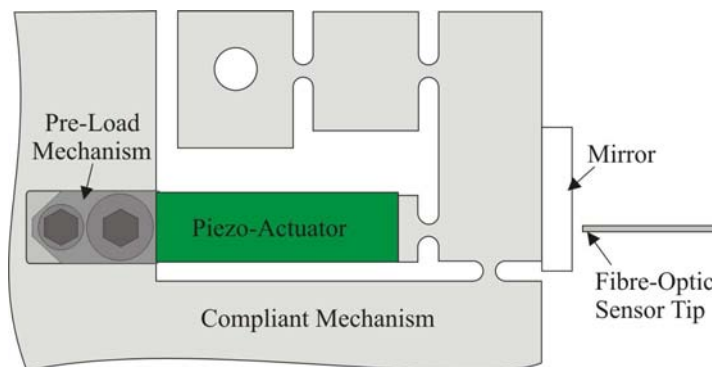


Figure 8-9 - Diagram showing the mounting of the mirror and positioning of the fibre-optic sensor for strain-gauge calibration of the first prototype.

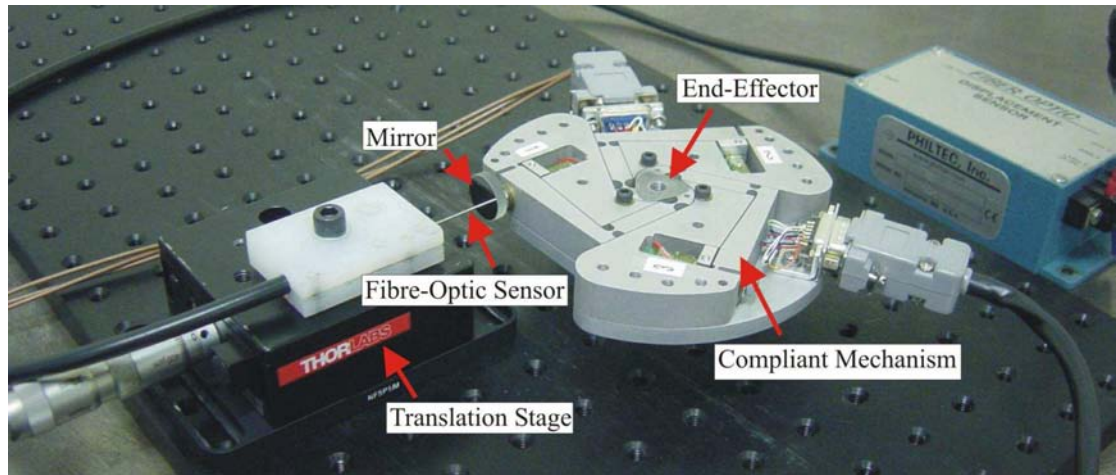


Figure 8-10 – Photograph showing the set-up used for strain gauge calibration of the second prototype.

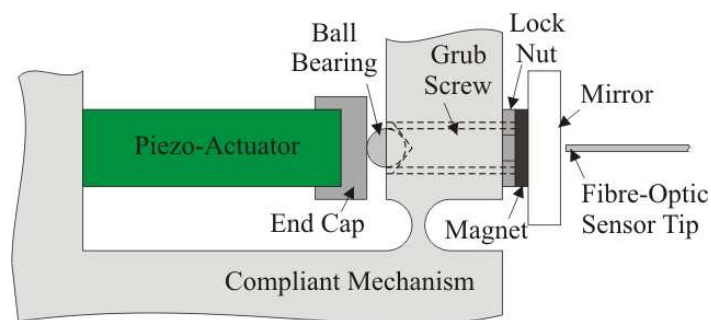


Figure 8-11 - Diagram showing the mounting of the mirror and positioning of the fibre-optic sensor for strain-gauge calibration of the second prototype.

Using this approach the strain gauge voltage relates to the displacement of the compliant mechanism input link, ΔD , rather than the length change of the piezo-actuator, ΔL . Therefore, the experimentally derived Jacobian gives the relationship between input link displacement and end-effector displacement. This approach was taken so that any unmodelled compliance in the preload, would not cause discrepancies between the model and experimental results. This is in accordance with the way the Jacobian was determined in the models.

8.3.5 End-effector position measurement

The end-effector location and rotation were determined using measurements recorded by three Micro-Epsilon eddyNCDT 3700 eddy-current sensors. Three aluminium targets were mounted to the end-effectors of the prototypes and the sensors recorded the change in displacement of the targets. The sensors were mounted on translation stages so that they could be correctly positioned relative to the target, within their measurement range. For the first prototype the sensors and targets were positioned as shown in Figure 8-12. A rectangular end-effector was attached specifically for this experiment so that the targets could be appropriately positioned.

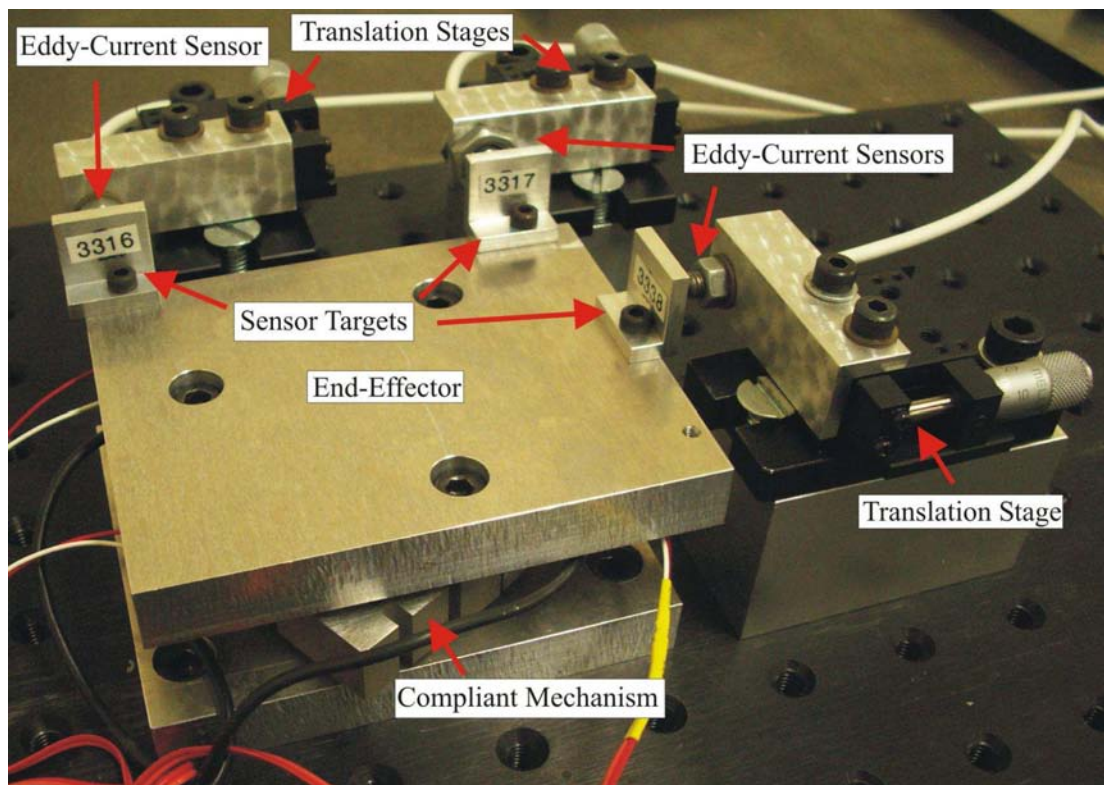


Figure 8-12 – Photograph showing the set-up used to determine the Jacobian of the first prototype.

For the second prototype a flat square plate was mounted to the end-effector of the 3RRR compliant mechanism and to this were mounted the three aluminium targets, as shown in Figure 8-13. The three eddy-current sensors were positioned as shown in Figure 8-13 to measure the displacement of the targets.

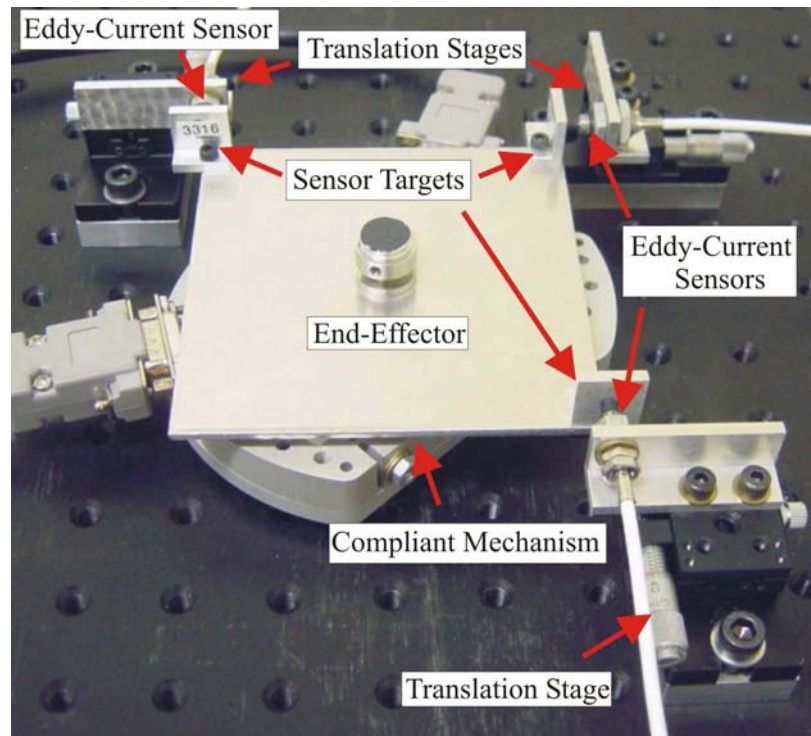


Figure 8-13 - Photograph showing the set-up used to determine the Jacobian of the second prototype.

The ΔX , ΔY displacement and rotation, $\Delta\theta_z$, of the end-effector could be determined from the displacement measured by the three eddy-current sensors.

The piezo-actuator amplifiers, strain gauge conditioning circuitry and eddy-current transducers were connected to a dSPACE DS1104 DSP controller board via inbuilt DACs and ADCs. A schematic of the experimental set-up is shown in Figure 8-14.

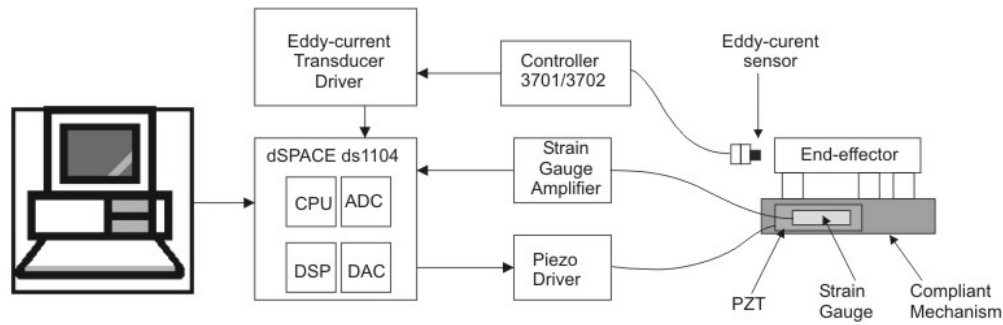


Figure 8-14- Schematic of the first prototype experimental set-up.

During experiments the $XY\theta_Z$ micro-motion stage was mounted on an anti-vibration table and in a room with stable temperature.

8.4 Kinematic model validation

8.4.1 Experimental procedure to determine the Jacobian of the 3RRR compliant mechanism

Each piezo-actuator was displaced one at a time to its maximum displacement, with 100V input, while the other two piezo-actuators were constrained to have zero displacement. To control the length of each piezo-actuator PI feedback control was used. The end-effector displacement, ΔX , ΔY and rotation, $\Delta\theta_Z$, was measured using the three eddy-current sensors. This resulted in three sets of data, ΔX versus ΔD , ΔY versus ΔD and $\Delta\theta_Z$ versus ΔD , where ΔD is the displacement of a compliant mechanism input link. The experiment was repeated for each piezo-actuator, giving a total of nine data sets. Each of the nine sets of experimental data was approximated by a linear fit. The slope of each line corresponds to one of the constants in the experimental Jacobian. An example of this procedure is given in equations (8.1) and (8.2) for an input to piezo-actuator 1, causing displacement of input link 1, ΔD_1 .

$$\begin{bmatrix} \Delta X(\Delta D_1) \\ \Delta Y(\Delta D_1) \\ \Delta \theta_z(\Delta D_1) \end{bmatrix} = \begin{bmatrix} J_{11} & J_{12} & J_{13} \\ J_{21} & J_{22} & J_{23} \\ J_{31} & J_{32} & J_{33} \end{bmatrix} \begin{bmatrix} \Delta D_1 \\ 0 \\ 0 \end{bmatrix} = \begin{bmatrix} \Delta D_1 J_{11} + 0 + 0 \\ \Delta D_1 J_{21} + 0 + 0 \\ \Delta D_1 J_{31} + 0 + 0 \end{bmatrix} \quad (8.1)$$

$$\begin{bmatrix} J_{11} \\ J_{21} \\ J_{31} \end{bmatrix} = \begin{bmatrix} \Delta X(\Delta D_1) / \Delta D_1 \\ \Delta Y(\Delta D_1) / \Delta D_1 \\ \Delta \theta_z(\Delta D_1) / \Delta D_1 \end{bmatrix} \quad (8.2)$$

8.4.2 Experimental results

8.4.2.1 Jacobian of the first prototype

The experimental data for ΔX vs ΔD_i , ΔY vs ΔD_i and $\Delta \theta_z$ vs ΔD_i , ($i=1,2,3$) is given in Figures 8-15, 8-17 and 8-19, respectively. The end-effector displacements predicted by the 2-D FEM, SCHM and PRBM are also plotted in Figures 8-15, 8-17 and 8-19. To give these model predictions the piezo-actuator input displacements were multiplied by the 2-D FEM, SCHM and PRBM Jacobians to give a prediction of end-effector displacement. The errors between the model predictions and the experimental results are given in Figures 8-16, 8-18 and 8-20.

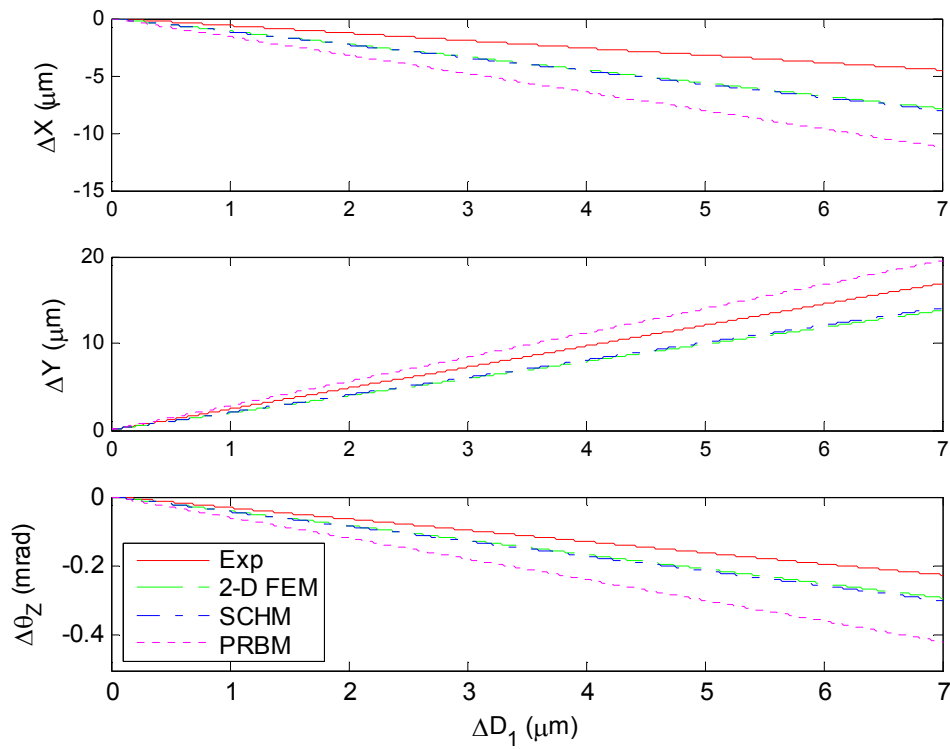


Figure 8-15 - Plots of ΔX , ΔY and $\Delta\theta_z$ vs. ΔD_1 for the first prototype given by the experiment, 2-D FEM, SCHM and PRBM.

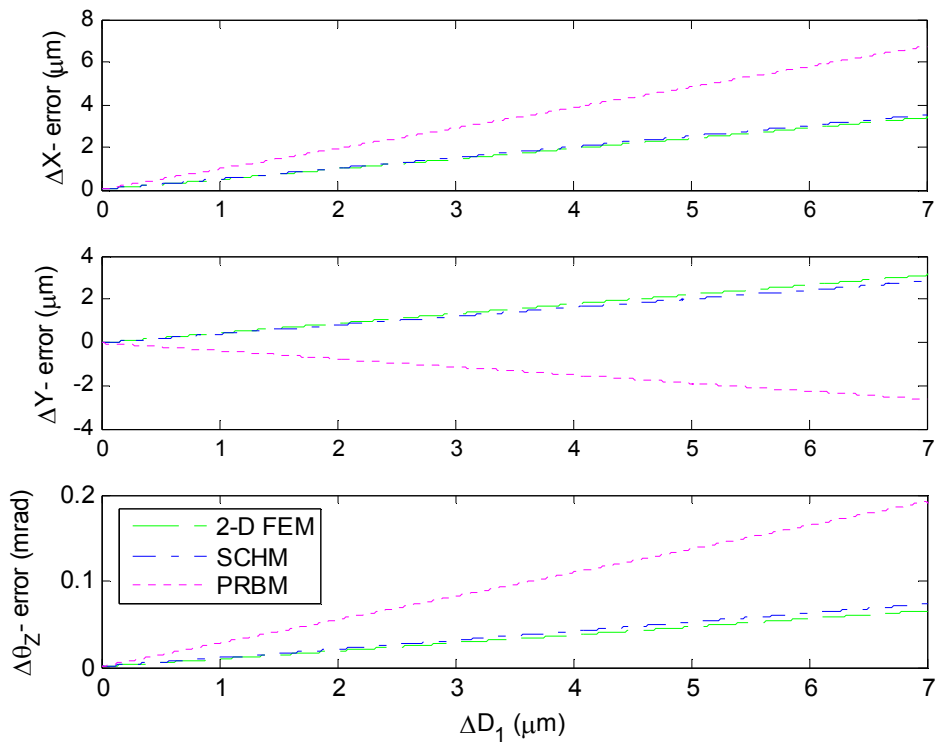


Figure 8-16 - Plots of ΔX -error, ΔY -error, and $\Delta\theta_z$ -error vs. ΔD_1 for the first prototype given by the 2-D FEM, SCHM and PRBM compared to the experiment result.

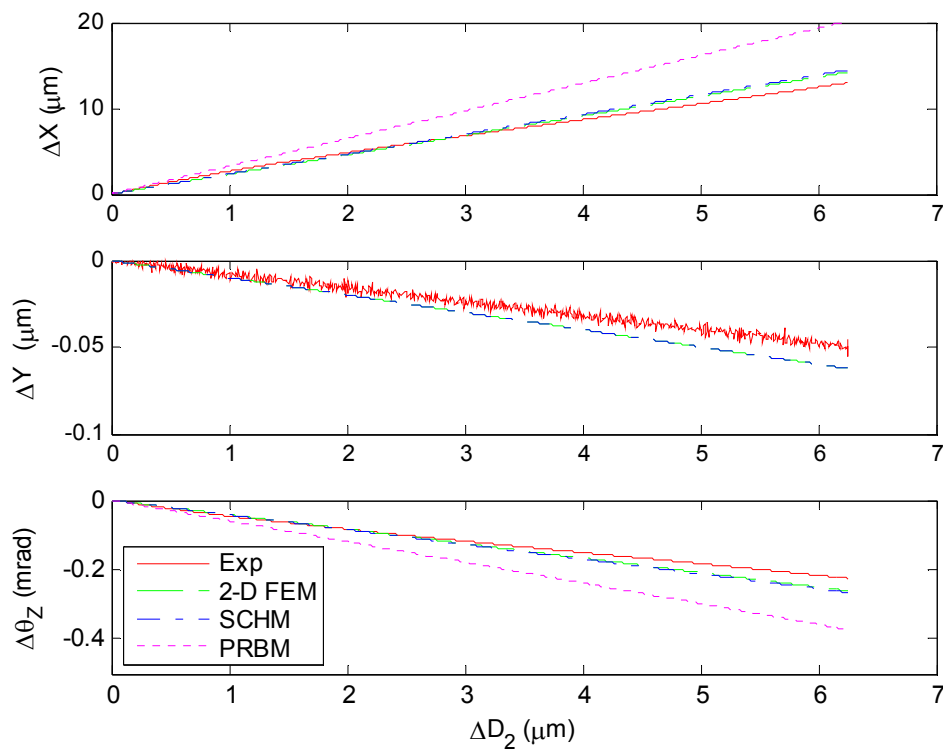


Figure 8-17 - Plots of ΔX , ΔY and $\Delta\theta_z$ vs. ΔD_2 for the first prototype given by the experiment, 2-D FEM, SCHM and PRBM.

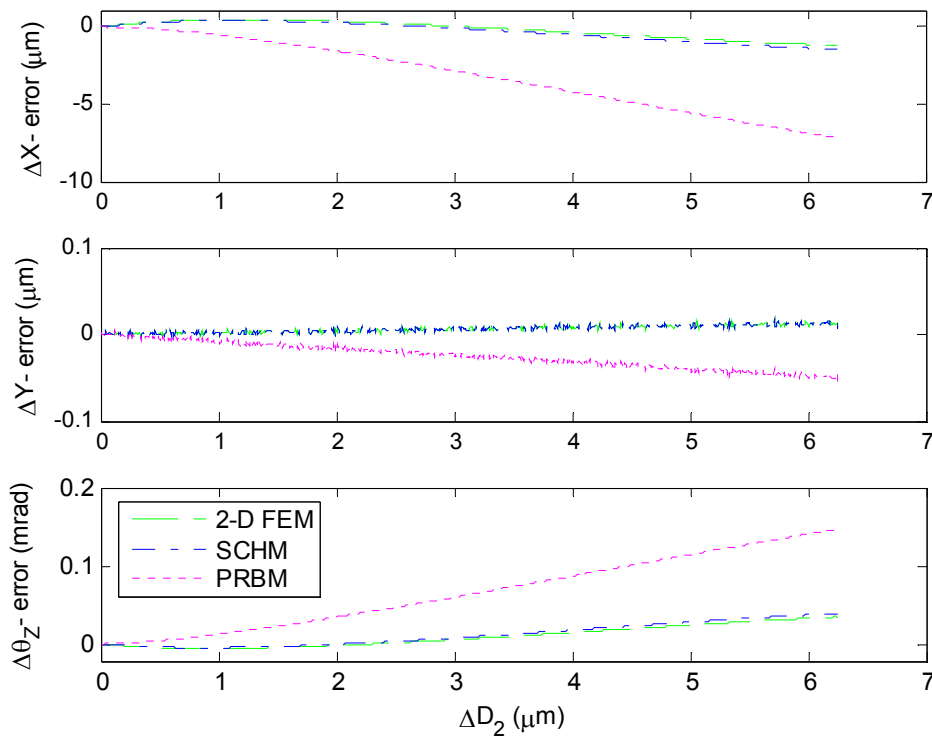


Figure 8-18 - Plots of ΔX -error, ΔY -error, and $\Delta\theta_z$ -error vs. ΔD_2 for the first prototype given by the 2-D FEM, SCHM and PRBM compared to the experiment result.

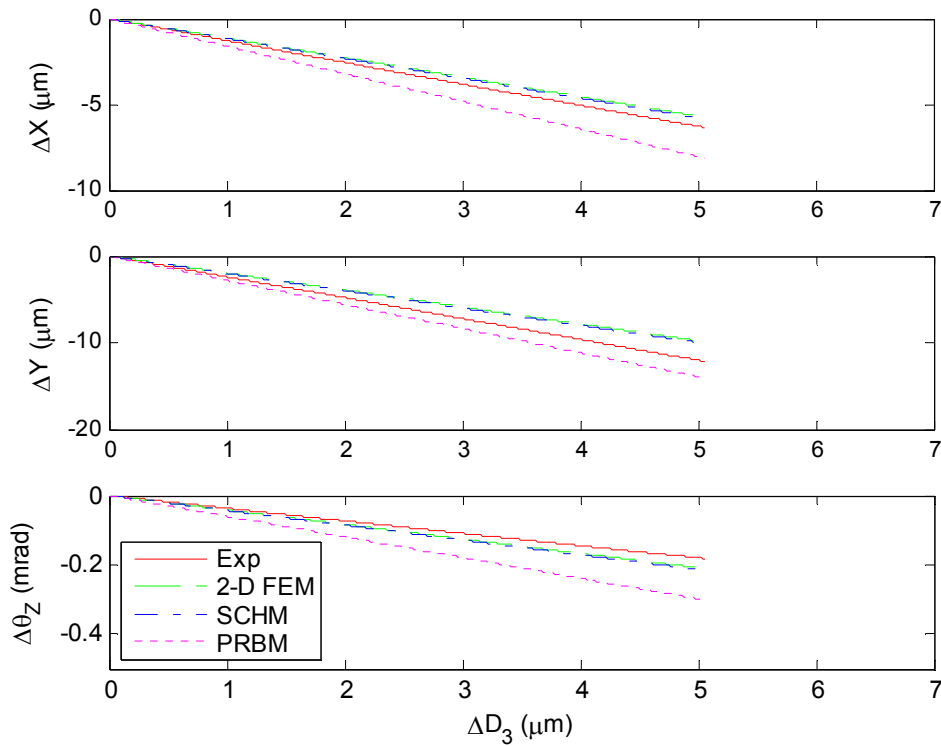


Figure 8-19 - Plots of ΔX , ΔY and $\Delta\theta_z$ vs. ΔD_3 for the first prototype given by the experiment, 2-D FEM, SCHM and PRBM.

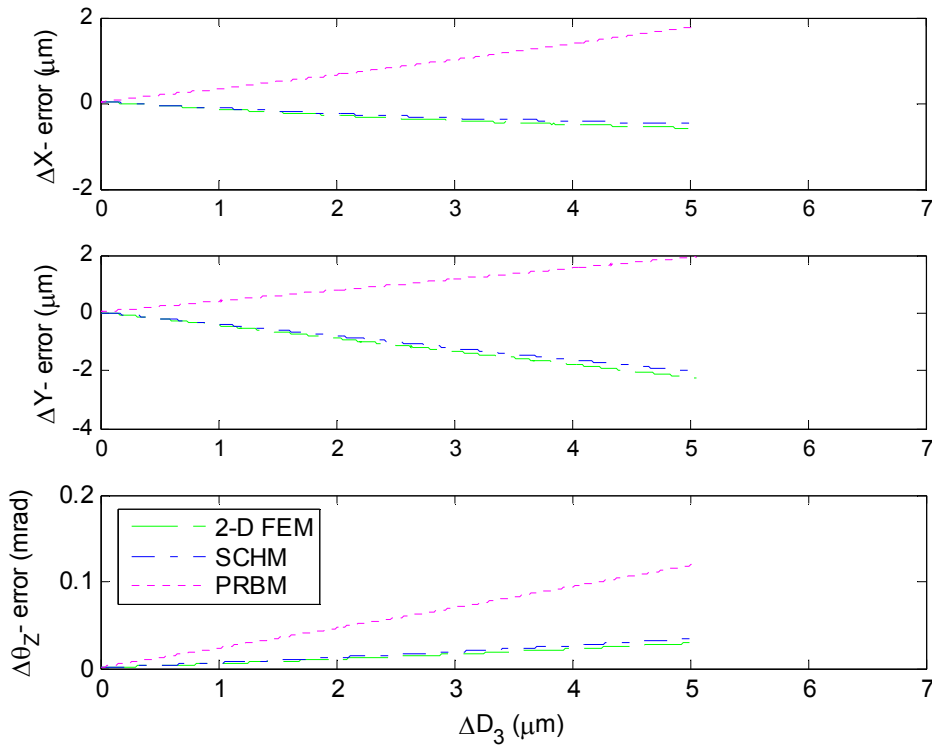


Figure 8-20 - Plots of ΔX -error, ΔY -error, and $\Delta\theta_z$ -error vs. ΔD_3 for the first prototype given by the 2-D FEM, SCHM and PRBM compared to the experiment result.

Linear approximations were fitted to the experimental data of Figures 8-15, 8-17 and 8-19. Using the slope of the lines the constants of the Jacobian were experimentally derived, as given in Table 8-1.

Experimental Jacobian		
-0.65	1.98	-1.26
2.42	-0.01	-2.42
-32.41	-34.55	-35.97

Table 8-1- Experimentally determined Jacobian of the first prototype 3RRR compliant mechanism

This can be compared to the model Jacobians derived in Chapter 4 and presented here again in Table 8-2. The error between the models and the experimentally derived Jacobian is also given in Table 8-2.

2-D FEM			SCHM			PRBM		
-1.13	2.27	-1.14	-1.15	2.31	-1.16	-1.61	3.22	-1.61
1.97	-0.01	-1.96	2.01	-0.01	-2.00	2.79	0.00	-2.79
-41.69	-41.80	-41.77	-42.77	-42.52	-42.78	-59.69	-59.66	-59.69
% Error Compared to Experimentally Determined Jacobian								
-73.7	-14.5	9.1	-77.3	-16.9	7.3	-148.3	-62.7	-28.1
18.6	-17.8	18.8	17.0	-11.2	17.2	-15.4	100.0	-15.5
-28.6	-21.0	-16.1	-32.0	-23.1	-18.9	-84.2	-72.7	-65.9

Table 8-2 - Jacobians for the first prototype 3RRR compliant mechanism predicted by the 2-D FEM, SCHM and PRBM, and error compared to experimentally determined Jacobian.

8.4.2.2 Discussion

From Table 8-2 it can be noted that the experimental and theoretical Jacobians are significantly different. However, this is likely to be in part due to problems with the

first prototype experimental set up. These problems are discussed in the following section.

Based upon these experimental results it can be seen that the 2-D FEM gives the prediction of the Jacobian closest to the experiment. The SCHM gives a similarly close prediction of the translational movement but less accurate prediction of the rotation. The PRBM prediction is less accurate than both the other models, particularly for the rotation.

8.4.3 Problems with the first prototype experimental results

8.4.3.1 Problems with strain gauge calibration

A problem was identified with the strain gauge calibration method: as the mirror was mounted to the link of the compliant mechanism the mirror would rotate when the piezo-actuator was displaced. This meant that the fibre-optic sensor tip and the mirror would not remain perpendicular during the measurement. This introduced a non-linear error into the strain gauge calibration.

8.4.3.2 Preload mechanism of the first prototype

The displacement of the unloaded piezo-actuators is specified by the manufacturer to be $11.6 \pm 2.0 \mu\text{m}$ with a 100V input. According to the model prediction discussed in Chapter 5 the displacement of the piezo-actuator assembled into the first prototype compliant mechanism should be close to $9 \mu\text{m}$. However, as can be seen from Figures 8-15 to 8-20, the displacement measured by the fibre-optic sensor is much less, as

little as $5\mu\text{m}$ for piezo-actuator 3. This discrepancy can be attributed to the preload mechanism. The preload mechanism of the first prototype is shown in Figures 8-3 and 8-4. A sliding preload block is used to provide the preload and this block is fixed in place by a locking bolt. Theoretically this block should not displace at all and provide a rigid support for the piezo-actuator. However, it is highly likely that, in the real system, it might displace by a small amount. To check this the displacement of the block was measured by bonding an aluminium target to it and measuring its displacement with the eddy-current sensor. It was found that for a maximum displacement of the piezo-actuator the displacement of the preload block was just over $3\mu\text{m}$. The block acts as a spring and returns to its original position when the piezo-actuator displacement returns to zero. This compliance is very significant and explains why the input link displacement is significantly less than the expected piezo-actuator input displacement. As this effect was not modelled by the 3RRR compliant mechanism model or piezo-actuator model it becomes clear why it is important to measure the input link displacement directly, and thereby allow for a better comparison with the 3RRR compliant mechanism model.

It was hypothesised that the flexibility of the preload mechanism is due to the small diameter screw and bolts used. It was suggested that a better design of compliant mechanism should take the preload into consideration at the early design phase to allow adequate room for the preload mechanism in the compliant mechanism.

8.4.3.3 End-effector attachment

The design of the first prototype necessitates the preload to be applied with the end-effector removed, to allow access to the locknut and adjustment screw. This means that the linkages of the compliant mechanism are displaced from their original position before the end-effector is attached and, therefore, the geometry of the compliant mechanism is slightly different to the model. In addition, the tightening of the end-effector bolts has the tendency to deform the compliant mechanism, which is likely to affect the overall geometry of the compliant mechanism, causing it to differ slightly from the model.

Furthermore, the strain gauges need to be calibrated with the circular end-effector fitted, as shown in Figure 8-8, but the Jacobian measurement needs the rectangular end-effector shown in Figure 8-12. This means that the end-effector needs to be removed and attached after calibration of the strain-gauges. It was found that the strain gauge calibration after the removal and reattachment of the end-effector was sometimes different by a significant margin, as large as 5%-10%. This meant that the strain gauge calibration was unreliable.

8.4.3.4 Jacobian of the second prototype

The experimental data for ΔX versus ΔD_i , ΔY versus ΔD_i and $\Delta \theta_z$ versus ΔD_i , ($i=1,2,3$) is given in Figures 8-21, 8-23 and 8-25, respectively. The end-effector displacements predicted by the 2-D FEM, SCHM and PRBM are also plotted in Figures 8-21, 8-23 and 8-25. To arrive at these model predictions the piezo-actuator

input displacements were multiplied by the 2-D FEM, SCHM and PRBM Jacobians, giving a prediction of end-effector displacement. The errors between the model predictions and the experimental results are given in Figures 8-22, 8-24 and 8-26.

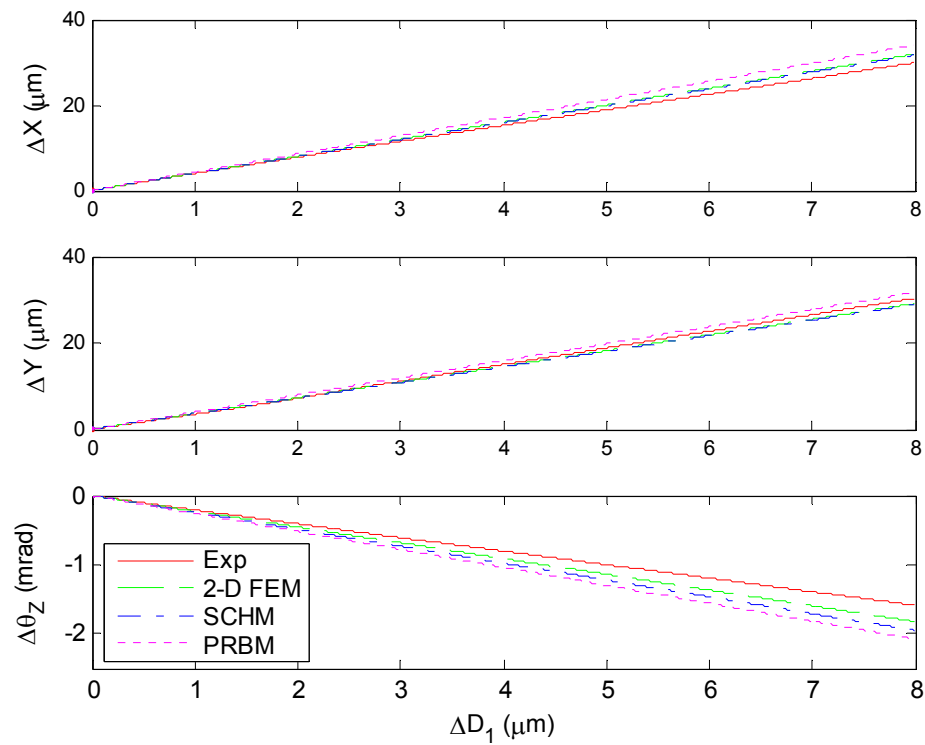


Figure 8-21 - Plots of ΔX , ΔY and $\Delta\theta_z$ vs. ΔD_1 for the second prototype given by the experiment, 2-D FEM, SCHM and PRBM.

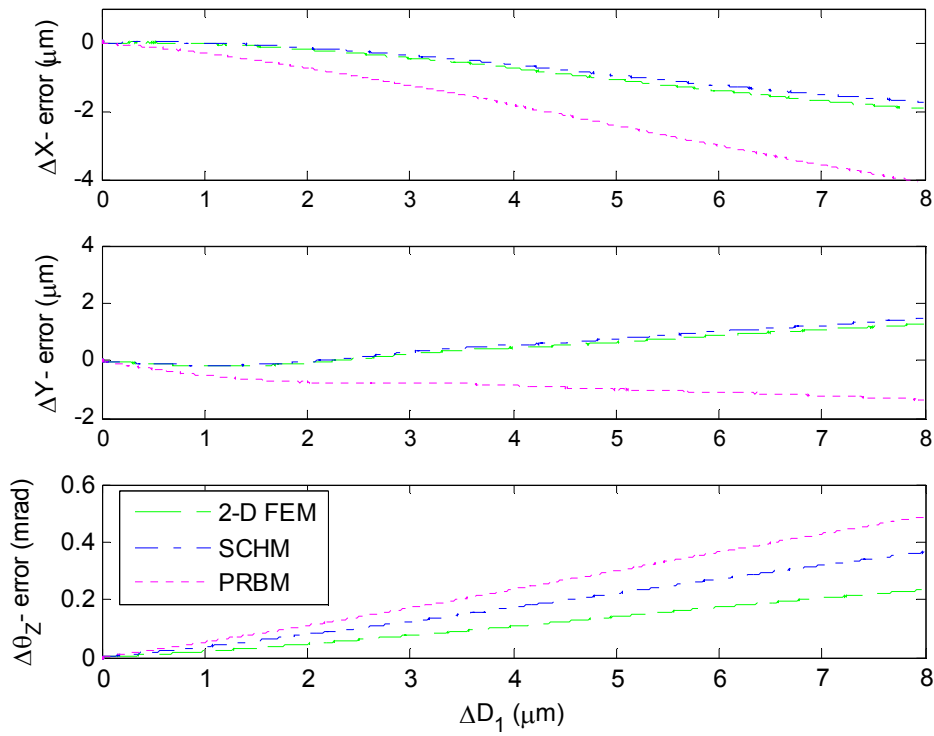


Figure 8-22 - Plots of ΔX -error, ΔY -error, and $\Delta\theta_z$ -error vs. ΔD_1 for the second prototype given by the 2-D FEM, SCHM and PRBM compared to the experiment result.

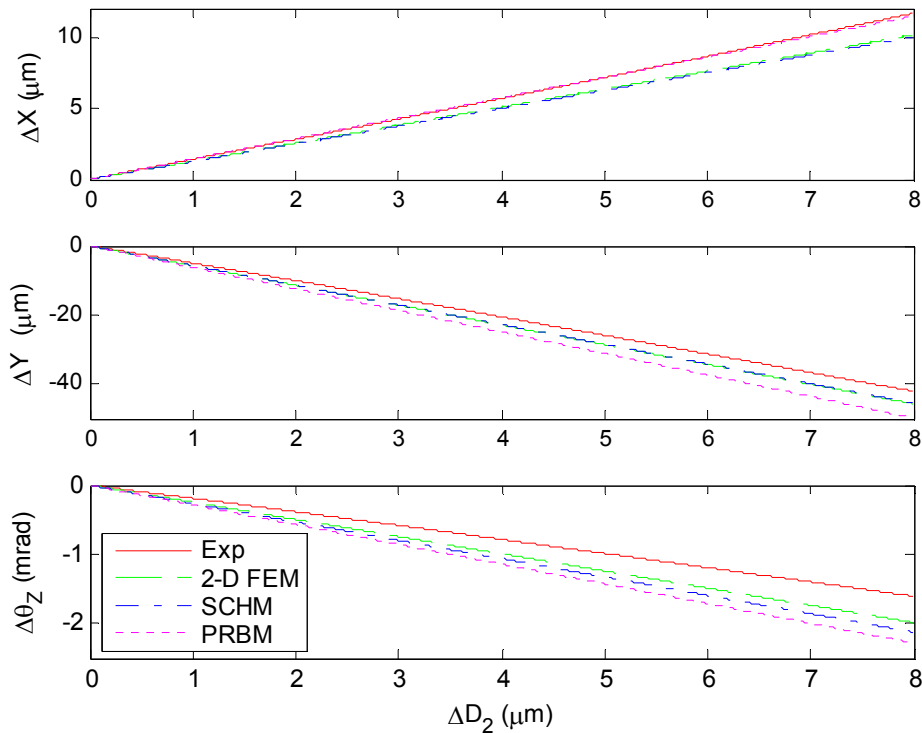


Figure 8-23 - Plots of ΔX , ΔY and $\Delta\theta_z$ vs. ΔD_2 for the second prototype given by the experiment, 2-D FEM, SCHM and PRBM.

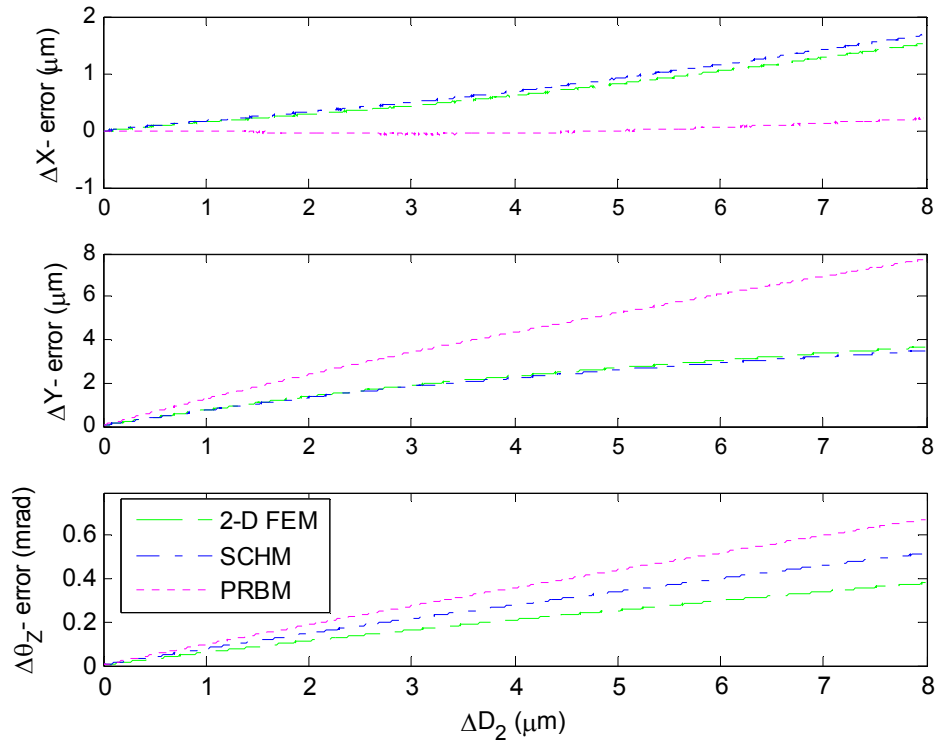


Figure 8-24 - Plots of ΔX -error, ΔY -error, and $\Delta\theta_z$ -error vs. ΔD_2 for the second prototype given by the 2-D FEM, SCHM and PRBM compared to the experiment result.

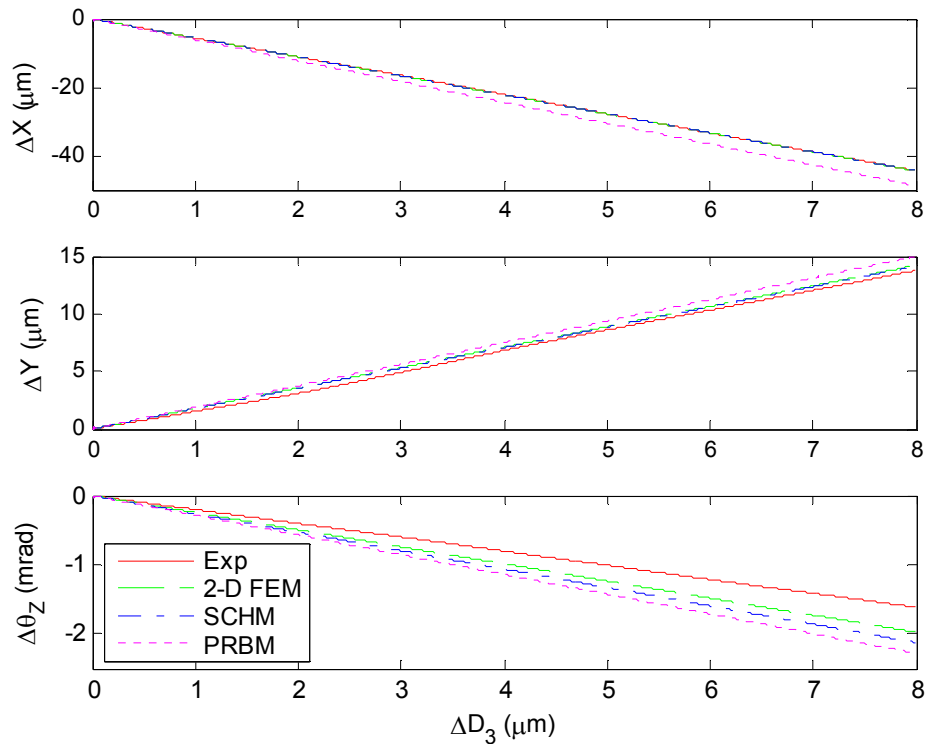


Figure 8-25 - Plots of ΔX , ΔY and $\Delta\theta_z$ vs. ΔD_3 for the second prototype given by the experiment, 2-D FEM, SCHM and PRBM.

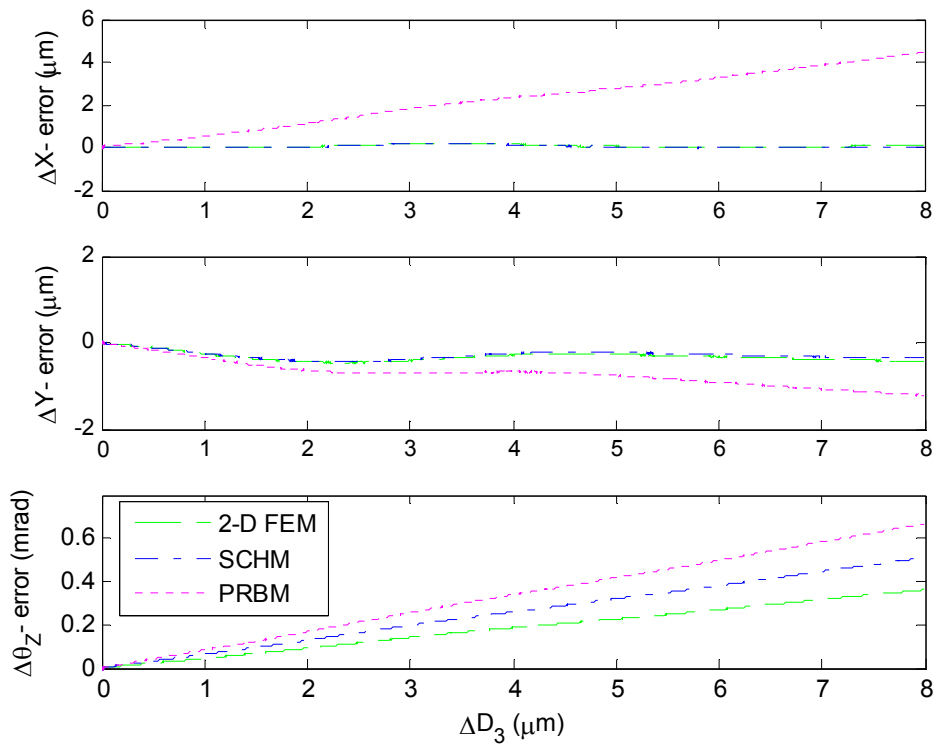


Figure 8-26 - Plots of ΔX -error, ΔY -error, and $\Delta\theta_z$ -error vs. ΔD_3 for the second prototype given by the 2-D FEM, SCHM and PRBM compared to the experiment result.

Linear approximations were fitted to the experimental data of Figures 8-21, 8-23 and 8-25. Using the slope of the lines the constants of the Jacobian were experimentally derived, as given in Table 8-3.

Experimental Jacobian		
3.84	1.40	-5.62
3.87	-5.44	1.84
-199.77	-211.90	-209.42

Table 8-3 - Experimentally determined Jacobian of the second prototype 3RRR compliant mechanism.

This can be compared to the model Jacobians derived in Chapter 7, which are presented here again in Table 8-4. The error between the models and the experimentally derived Jacobian is also given in Table 8-4.

2-D FEM			SCHM			PRBM		
3.98	1.27	-5.55	3.97	1.25	-5.58	4.25	1.43	-6.10
3.63	-5.71	1.77	3.62	-5.72	1.77	3.96	-6.22	1.87
-227.90	-248.10	-247.10	-244.66	-266.20	-266.21	-259.75	-285.19	-285.19
% Error Compared to Experimentally Derived Jacobian								
-3.8	9.9	1.2	-3.5	10.8	0.8	-10.9	-1.9	-8.6
6.1	-4.9	3.6	6.4	-5.0	3.7	-2.4	-14.3	-1.8
-14.1	-17.1	-18.0	-22.5	-25.6	-27.1	-30.0	-34.6	-36.2

Table 8-4 - Jacobians for the second prototype 3RRR compliant mechanism predicted by the 2-D FEM, SCHM and PRBM, and error compared to experimentally determined Jacobian.

8.4.3.5 Discussion

It can be seen from Table 8-4 that the 2-D FEM gives the closest prediction to the experimental result. The SCHM gives a similarly close prediction of the translational movement, but less accurate prediction of the rotation. The PRBM prediction is less accurate than both the other models, particularly for the rotation.

8.4.4 Experimental procedure to determine the workspace

8.4.4.1 Reachable workspace

The reachable workspaces of both prototypes were found experimentally by determining the vertices of the maximum reachable workspace, which were given by applying the input voltages given in Table 8-5. These points define the extremities of the workspace and the reachable workspace fills the volume between the points. The rotation is plotted on the z-axis. The volumes describing the reachable workspaces were then plotted; they are a cube like shape.

Vertex Number	Piezo-Actuator Input Voltage (V)		
	Piezo 1	Piezo 2	Piezo 3
1	0	0	0
2	0	0	100
3	0	100	0
4	0	100	100
5	100	0	0
6	100	0	100
7	100	100	0
8	100	100	100

Table 8-5 - Input displacement of piezo-actuators to give vertices of workspace.

The displacement of the compliant mechanism caused by the elongation of the piezo-actuators at 100V input is different for each actuator. This is due to; manufacturing differences of the piezo-actuators, which have a tolerance at 100V of $\pm 2.0\mu\text{m}$; compliance of the preload mechanism; and differences in the preload adjustment. In addition, creep of the actuator has an affect, and so the time taken to record the measurement affects the result. The maximum displacements of the compliant mechanism for each actuator are given in the results below.

8.4.4.2 Constant-orientation workspace

The maximum workspace area for which the end-effector orientation can be kept constant occurs when the end-effector rotation is half the maximum end-effector rotation, as given in equation (8.3).

$$\Delta\theta_{const} = \frac{\Delta\theta_{max}}{2} \quad (8.3)$$

The maximum constant-orientation workspace area is smaller than the reachable workspace area. The piezo-actuator inputs that give the vertices describing the constant-orientation workspace are given in Table 8-6. The experimental Jacobian and equations (8.4) to (8.6) were used to determine the required displacements of the input links $\Delta D_{1(\Delta\theta_{const})}$, $\Delta D_{2(\Delta\theta_{const})}$ and $\Delta D_{3(\Delta\theta_{const})}$.

$$\Delta D_{1(\theta_{const})} = (\Delta\theta_{const} - (\Delta D_{3\max,load} J_{33} + \Delta D_{2\max,load} J_{32})) / J_{31} \quad (8.4)$$

$$\Delta D_{2(\theta_{const})} = (\Delta\theta_{const} - (\Delta D_{1\max,load} J_{31} + \Delta D_{3\max,load} J_{33})) / J_{32} \quad (8.5)$$

$$\Delta D_{3(\theta_{const})} = (\Delta\theta_{const} - (\Delta D_{1\max,load} J_{31} + \Delta D_{2\max,load} J_{32})) / J_{33} \quad (8.6)$$

Vertex Number	Input-Link Displacement		
	ΔD_1	ΔD_2	ΔD_3
9	$\Delta D_{1\max,load}$	0	$\Delta D_{3(\Delta\theta_{const})}$
10	$\Delta D_{1\max,load}$	$\Delta D_{2(\Delta\theta_{const})}$	0
11	0	$\Delta D_{2\max,load}$	$\Delta D_{3(\Delta\theta_{const})}$
12	$\Delta D_{1(\Delta\theta_{const})}$	$\Delta D_{2\max,load}$	0
13	0	$\Delta D_{2(\Delta\theta_{const})}$	$\Delta D_{3\max,load}$
14	$\Delta D_{1(\Delta\theta_{const})}$	0	$\Delta D_{3\max,load}$

Table 8-6 - Input displacement of piezo-actuators to give vertices of constant orientation workspace.

The constant-orientation workspace is a hexagonal area which is included in the plot as the reachable workspace as an opaque yellow area.

8.4.4.3 Workspace width

Both the reachable workspace and constant-orientation workspace are hexagons when viewed in the X-Y plane. A simple measure to compare the size of the workspace X-Y areas is the workspace-width. The experimental workspace width was calculated and compared to the 2-D FEM, SCHM and PRBM.

8.4.5 Workspace results

8.4.5.1 The first prototype

The maximum displacement of the compliant mechanism input links caused by the piezo-actuators at 100V is given below.

$$\Delta D_{1\max,load} @100V = 7.1\mu\text{m}$$

$$\Delta D_{2\max,load} @100V = 6.4\mu\text{m}$$

$$\Delta D_{3\max,load} @100V = 5.1\mu\text{m}$$

The reachable and constant-orientation workspaces are plotted in Figure 8-27.

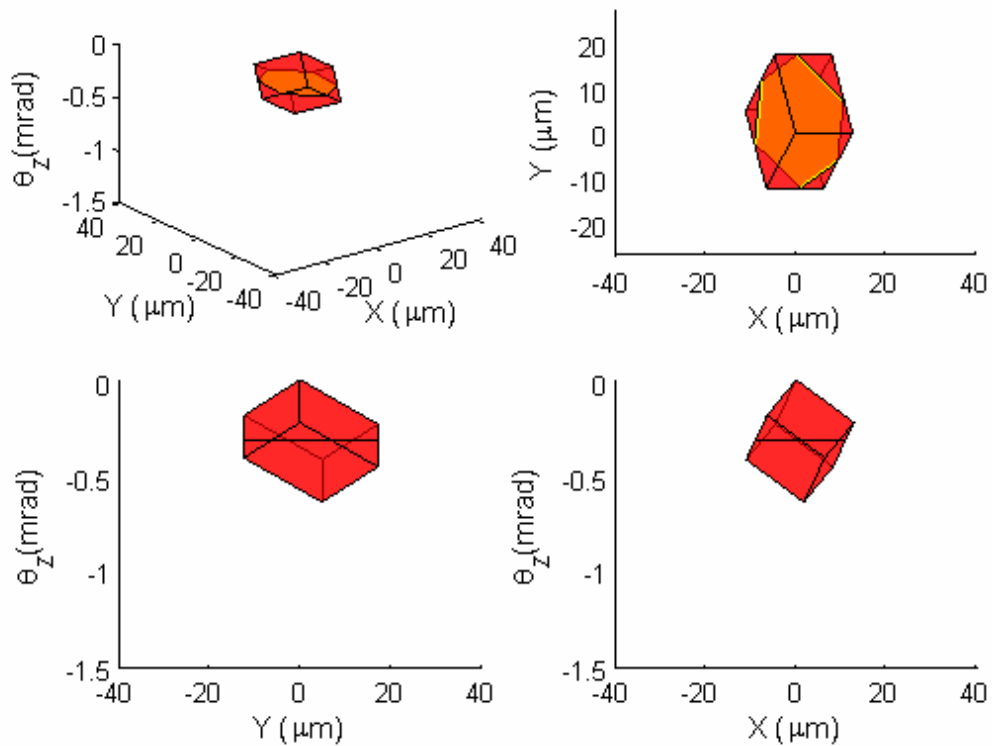


Figure 8-27 - Plots of the reachable and constant-orientation workspace for the first prototype $XY\theta_z$ stage given by the experiment.

This workspace can be compared to the workspace predicted by the 2-D FEM, SCHM and PRBM in Chapter 7. Figure 8-28 shows a comparison of the experimental, 2-D FEM, SCHM and PRBM constant-orientation workspace.

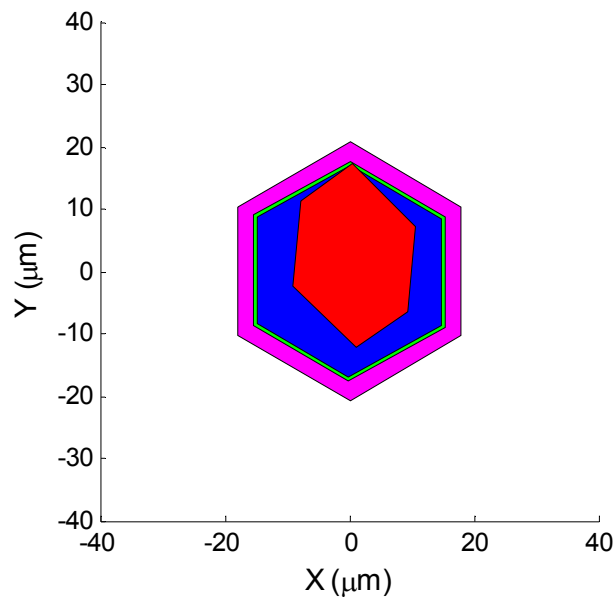


Figure 8-28 - Superimposed plots of constant-orientation workspace of the first prototype $XY\theta_z$ stage given by the experimental (red), 2-D FEM (green), SCHM (blue) and PRBM (magenta).

8.4.5.2 Workspace width

The reachable and constant-orientation workspace widths for the experiment, 2-D FEM, SCHM and PRBM are given in Table 8-7. It can be noted from Figures 8-27 and 8-28 that the experimental workspaces are not symmetrical. The widths given for the experimental result are for the maximum width across the workspace areas.

	Experiment	2-D FEM		SCHM		PRBM	
	(μm)	(μm)	% Error	(μm)	% Error	(μm)	% Error
Reachable workspace width	32.8	40.9	-24.7	39.1	-19.2	48.1	-46.6
Maximum constant-orientation workspace width	29.5	35.4	-20.0	33.9	-14.9	41.6	-41.0

Table 8-7 – Reachable and maximum constant-orientation workspace widths for the experiment, 2-D FEM, SCHM and PRBM, and % error compared to the experimental result.

8.4.5.3 Discussion

Due to the compliance of the preload mechanism the workspace of the experimental stage is far smaller than predicted by the models.

8.4.5.4 The second prototype

The maximum displacement of the compliant mechanism input links caused by the piezo-actuators at 100V is given below.

$$\Delta D_{1\max,load} @100V = 8.2\mu\text{m}$$

$$\Delta D_{2\max,load} @100V = 9.0\mu\text{m}$$

$$\Delta D_{3\max,load} @100V = 9.5\mu\text{m}$$

The reachable and constant-orientation workspaces are plotted in Figure 8-29.

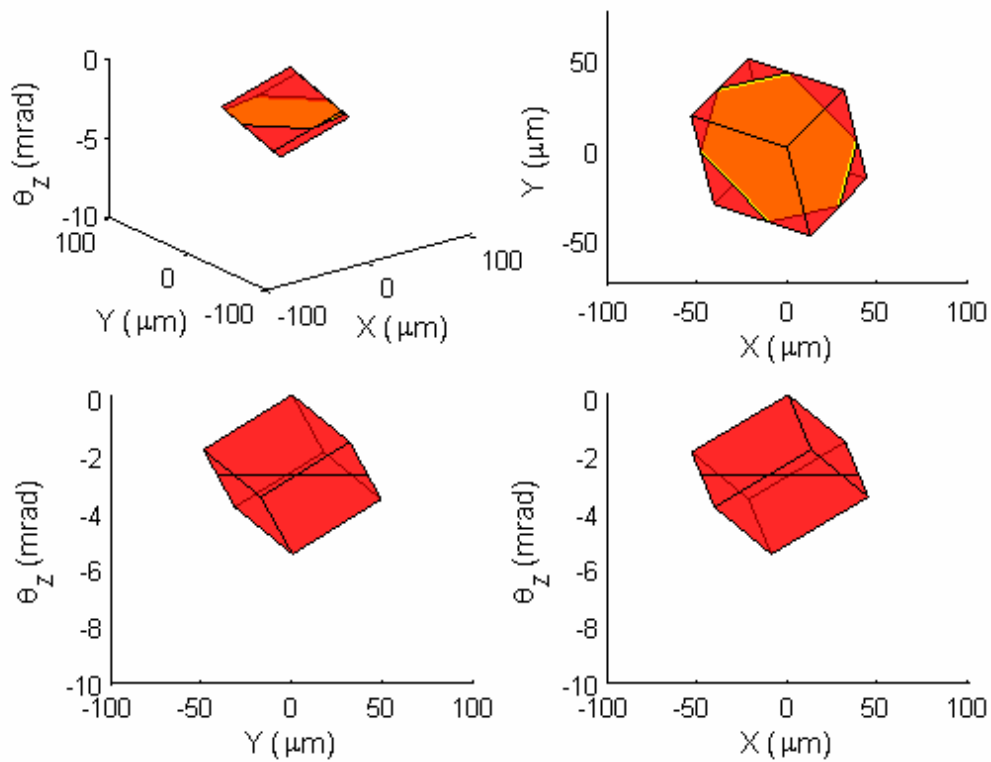


Figure 8-29 - Plots of the reachable and constant-orientation workspace for the second prototype $XY\theta_z$ stage given by the experiment.

This workspace can be compared to the workspace predicted by the 2-D FEM, SCHM and PRBM in Chapter 7. Figure 8-30 shows a comparison of the experimental, 2-D FEM, SCHM and PRBM constant-orientation workspace.

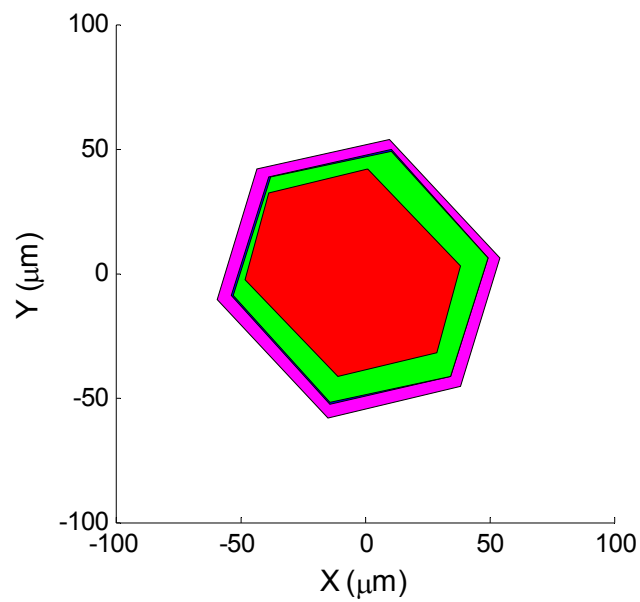


Figure 8-30 - Superimposed plots of constant-orientation workspace of the second prototype $XY\theta_z$ stage given by the experimental (red), 2-D FEM (green), SCHM (blue) and PRBM (magenta).

8.4.5.5 Workspace width

The reachable and constant-orientation workspace widths for the experiment, 2-D FEM, SCHM and PRBM are given in Table 8-8.

	Experiment	2-D FEM		SCHM		PRBM	
	(μm)	(μm)	% Error	(μm)	% Error	(μm)	% Error
Reachable workspace width	103.7	121.6	-17.3	119.9	-15.6	129.9	-25.3
Maximum constant-orientation workspace width	93.3	107.3	-15.0	105.9	-13.5	114.9	-23.2

Table 8-8 – Reachable and maximum constant-orientation workspace widths for the experiment, 2-D FEM, SCHM and PRBM, and % error compared to the experimental result.

8.4.5.6 Discussion

The workspace of the experimental stage is again considerably smaller than predicted by the models. This is partly due to the difference between experimental and model Jacobians and partly due to the displacement generated by the piezo-actuators being smaller than predicted.

8.5 Validation of the dynamic models

8.5.1 Experimental procedure to determine the natural frequencies

The natural frequencies of the first prototype and two 3RRR compliant mechanisms and $XY\theta_Z$ stages were determined using a Polytec PSV-400-3D scanning laser vibrometer. This uses three laser vibrometers to determine the three-dimensional modes of vibration of the target.

The 3RRR compliant mechanism and a shaker were mounted to a bracket, as shown in Figure 8-31, so that the tip of the shaker was in contact with the $XY\theta_Z$ stage base as shown in Figure 8-32. When excited the shaker would cause vibration of the $XY\theta_Z$ stage base and the compliant mechanism.

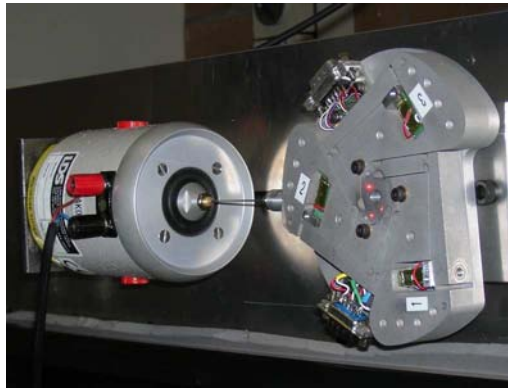


Figure 8-31 - The arrangement of the shaker and the second prototype $XY\theta_z$ stage.

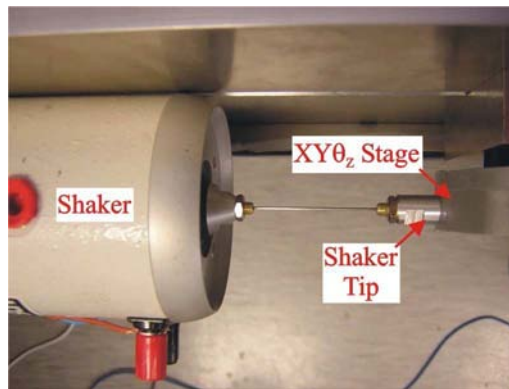


Figure 8-32 – Close-up of the shaker and the point of contact with the second prototype $XY\theta_z$ stage.

The three Polytec PSV-400 scanning heads were arranged, as shown in Figure 8-33, so that the laser beams all focused on the end-effector of the compliant mechanism, as shown in Figure 8-34.

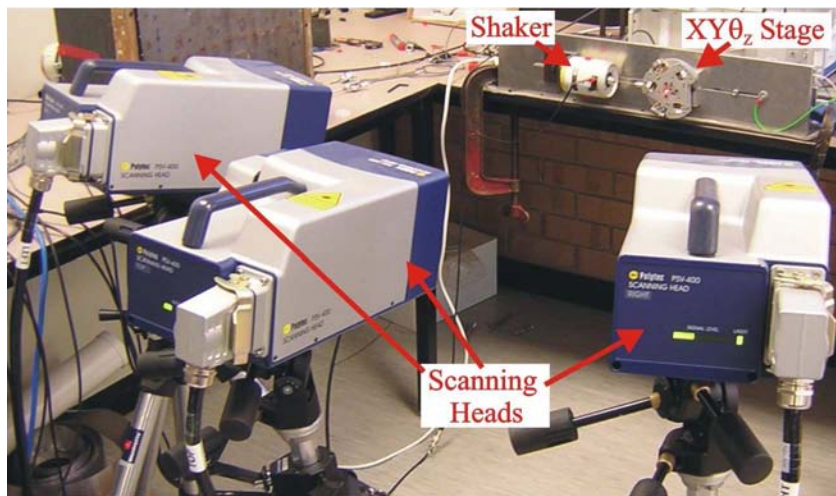


Figure 8-33 – Arrangement of the three scanning heads, shaker and the second prototype $XY\theta_z$ stage.

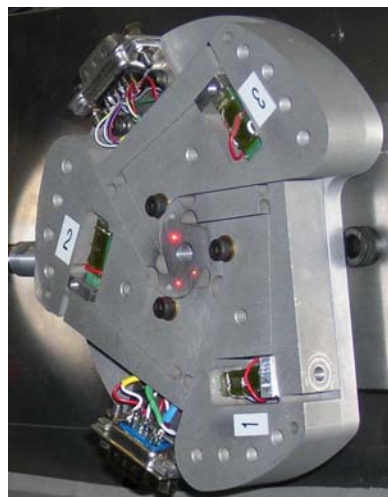


Figure 8-34 - Close-up of the second prototype $XY\theta_z$ stage showing the three laser beams (red dots) focused on the end-effector.

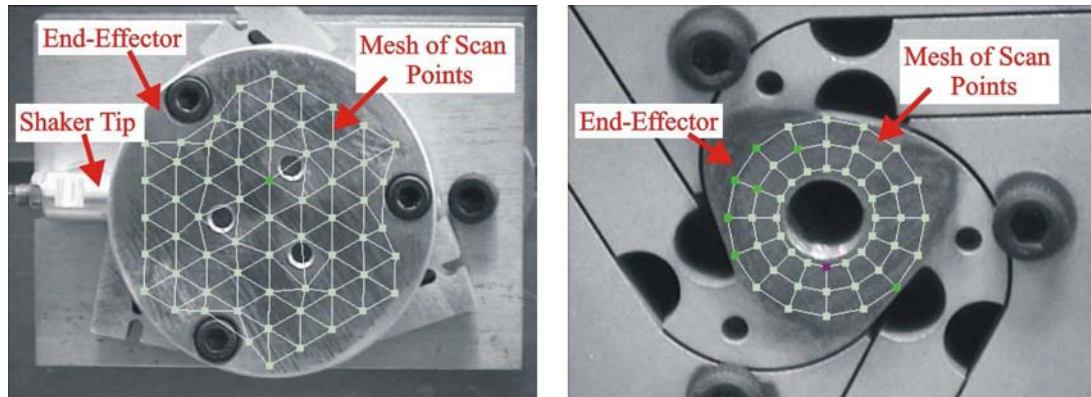


Figure 8-35 – Image of vibrometer scan area showing the mesh of the scan points for the first prototype (left) and the second prototype (right).

A mesh of scan points on the surface of the end-effector was defined as shown in Figure 8-35. During the vibrometer scan a white noise voltage signal is generated by the vibrometer. This signal, after amplification, is applied to the input of the shaker to excite the $XY\theta_z$ stage with white noise vibrations. A scan is performed during which all three laser vibrometers focus on a selected point of the mesh, determining the vibrational frequencies, in three dimensions, of the measurement point. After scanning all points in the mesh, the Polytec laser vibrometer software, PSVSoft, can generate a three-dimensional image of the vibrational frequencies of the mesh. From this, the natural frequencies of the meshed area can be determined.

The results were presented as plots of the average frequency response of the scan points in the x-axis, which is the direction of force application by the shaker. In addition, animations of the operational deflection patterns of the modes of vibration of the scan points were generated. The frequency plots are given for a frequency range from 100Hz to 1600Hz. All the first modes occur within this range.

Frequencies below 100Hz correspond to rigid-body vibrations of the bracket holding the stage.

8.5.2 Natural frequency results

8.5.2.1 The first prototype 3RRR compliant mechanism

Figure 8-36 shows the displacement magnitude frequency response for the average of the scan points in the x-axis of the 3RRR compliant mechanism. The frequencies corresponding to the natural frequencies are highlighted on the plots.

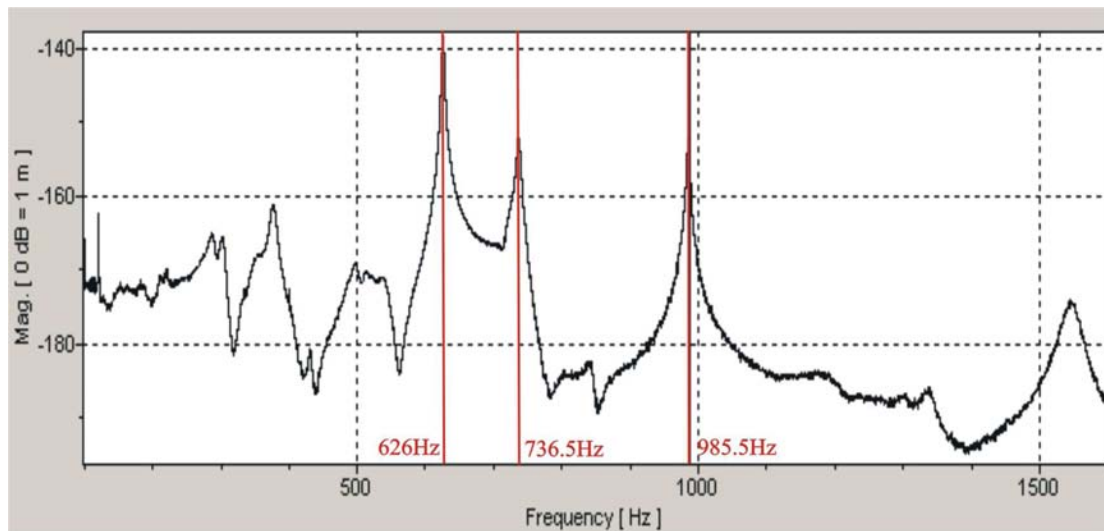


Figure 8-36 - Plot of average displacement magnitude (dB) vs. frequency for the first prototype 3RRR compliant mechanism.

Figures 8-37 to 8-39 show sequences from the animation of the operational deflection patterns corresponding to the modes of vibration for the 3RRR compliant mechanism. These clearly identify the translational and rotational modes.

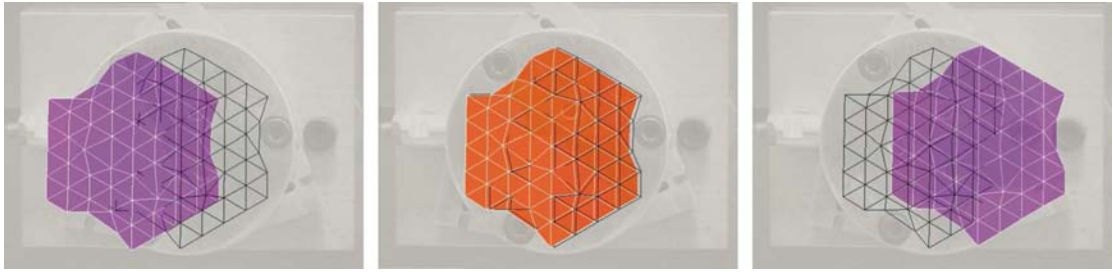


Figure 8-37 - Sequence from animation generated by PSVSoft, of the operational deflection patterns corresponding to the first translational mode, 626Hz, for the first prototype 3RRR compliant mechanism.

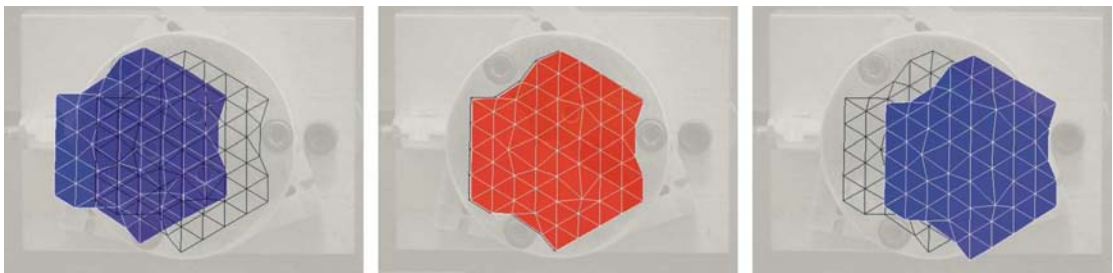


Figure 8-38 - Sequence from animation generated by PSVSoft, of the operational deflection patterns corresponding to the second translational mode, 736.5Hz, for the first prototype 3RRR compliant mechanism.



Figure 8-39 - Sequence from animation generated by PSVSoft, of the operational deflection patterns corresponding to the first rotational mode, 985.5Hz, for the first prototype 3RRR compliant mechanism.

8.5.2.2 The first prototype $XY\theta_z$ stage

Figure 8-40 shows the averaged displacement magnitude versus frequency response for all scan points in the x-axis of the $XY\theta_z$ stage. The frequencies corresponding to the natural frequencies are highlighted on the plots.

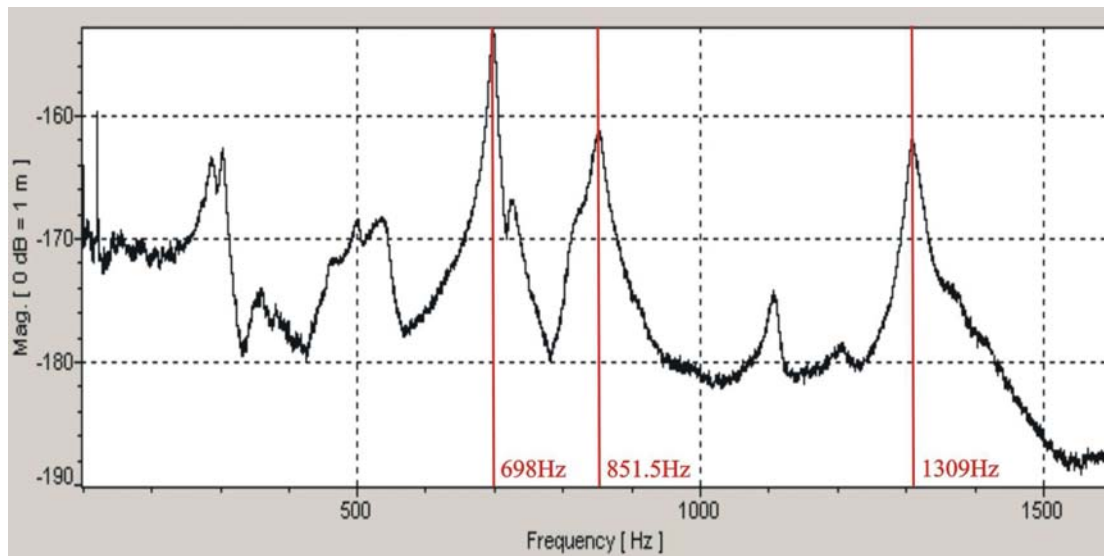


Figure 8-40 - Plot of displacement magnitude (dB) vs. frequency for the first prototype $XY\theta_z$ micro-motion stage

Figures 8-41 to 8-43 show sequences from the animation of the operational deflection patterns corresponding to the modes of vibration for the $XY\theta_z$ stage.

These clearly identify the translational and rotational modes.

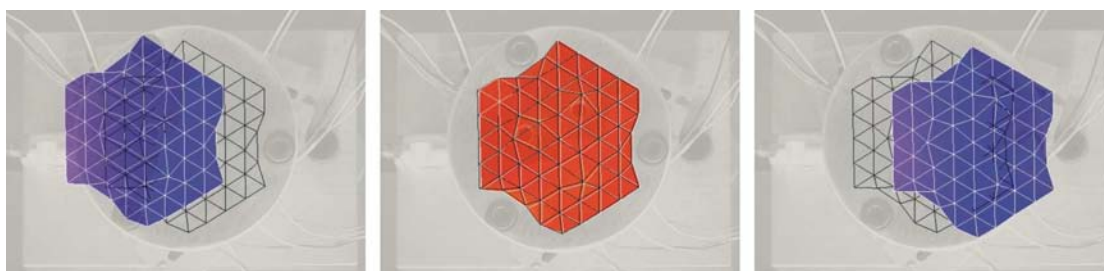


Figure 8-41 - Sequence from animation generated by PSVSoft, of the operational deflection patterns corresponding to the first translational mode, 698Hz, for the first prototype $XY\theta_z$ stage.

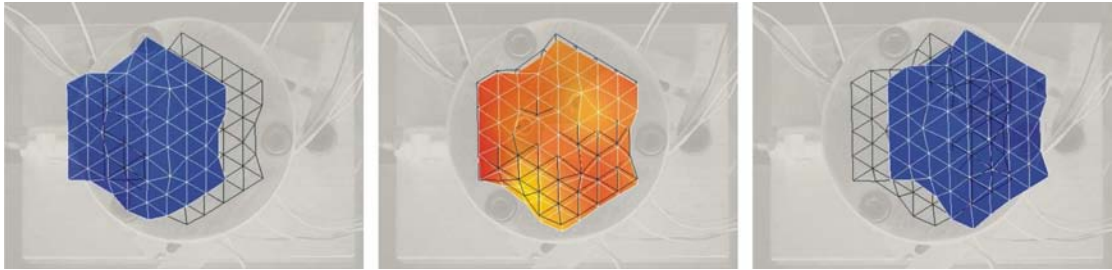


Figure 8-42 - Sequence from animation generated by PSVSoft, of the operational deflection patterns corresponding to the second translational mode, 851.5Hz, for the first prototype XYθ_z stage.



Figure 8-43 - Sequence from animation generated by PSVSoft, of the operational deflection patterns corresponding to the first rotational mode, 1309Hz, for the first prototype XYθ_z stage.

All the natural frequencies are tabulated in Table 8-9 and a comparison is given with the natural frequency prediction given by the 2-D FEM, SCHM and PRBM.

Natural Frequencies of 3RRR											
Mode	Exp	2-D FEM		SCHM				PRBM			
		ω_n	% error	$K_{Analytical}$		K_{FEA}		$K_{Analytical}$		K_{FEA}	
	ω_n	ω_n	% error	ω_n	% error	ω_n	% error	ω_n	% error	% error	
1 st Translation	626.0	660.7	-5.5	771.2	-23.2	697.4	-11.4	784.2	-25.3	707.1	-13.0
2 nd Translation	736.5	660.7	10.3	771.2	-4.7	697.4	5.3	784.4	-6.5	707.1	4.0
1 st Rotation	985.5	1004.1	-1.9	1613.9	-63.8	1458.1	-48.0	1633.0	-65.7	1472.3	-49.4
Natural Frequencies of XYθ _z											
Mode	Exp	2-D FEM		SCHM				PRBM			
		ω_n	% error	$K_{Analytical}$		K_{FEA}		$K_{Analytical}$		K_{FEA}	
	ω_n	ω_n	% error	ω_n	% error	ω_n	% error	ω_n	% error	% error	
1 st Translation	698.0	1001.7	-43.5	1166.0	-67.0	1111.8	-59.3	1344.5	-92.6	1299.3	-86.1
2 nd Translation	850.0	1002.1	-17.9	1166.1	-37.2	1111.9	-30.8	1344.6	-58.2	1299.4	-52.9
1 st Rotation	1300.0	1509.2	-16.1	2549.4	-96.1	2423.9	-86.5	2870.7	-120.8	2769.3	-113.0

Table 8-9 – Natural frequencies for the first prototype 3RRR compliant mechanism and XYθ_z stage given by experiment, 2-D FEM, SCHM and PRBM.

8.5.2.3 Discussion

Three natural frequencies can be clearly identified for both the 3RRR compliant mechanism and $XY\theta_z$ stage from Figures 8-36 and 8-40, respectively. Comparing these two figures it can be seen that the smaller peaks at frequencies below 600Hz occur at the same frequencies. As these peaks are not affected by the piezo-actuators this indicates that these frequencies correspond to rigid-body vibrations of the support structure, or harmonics in the shaker.

From the experimental results shown in Figures 8-37 and 8-38 it can be seen that for the 3RRR compliant mechanism two translational modes are excited in the x-direction, the direction of force application. These occur at two clearly distinct frequencies. From the model predictions a translational mode at one frequency is expected. The reason for the experimentally observed bi-modal result is unclear. One of the frequencies may be due to a vibration of the support structure or a harmonic of the shaker. The 2-D FEM gives a prediction close to the first translational mode given by the experiment. The SCHM and PRBM of the 3RRR compliant mechanism give very similar predictions and are close to the experiment when K_{FEA} is used.

From the experiment result shown in Figure 8-39 the rotational mode can clearly be seen. It should be pointed out that this is a purely rotational mode with no translational motion. The 2-D FEM prediction for the rotational mode of the 3RRR compliant mechanism is very close to the experimental result. The SCHM and PRBM prediction is not very accurate due to the inaccurate modelling of the end-

effector. The predictions of both the SCHM and PRBM are closer to the experiment when K_{FEA} is used.

From Figures 8-36 and 8-40 it can be seen that the modes of the $XY\theta_Z$ stage are similar to the 3RRR compliant mechanism but shifted to higher frequencies. From Figure 8-43 it can be noted that the rotational mode now also experiences some translational movement. The models all predict that the $XY\theta_Z$ stage modes occur at significantly higher frequencies than given by the experimental results. This suggests that either the piezo-actuator model is inaccurate, or that the un-modelled preload compliance has a significant effect. The 2-D FEM gives the prediction of translational and rotational mode frequency closest to the experimental result. For both the translational and rotational modes the SCHM gives a prediction closer to the experiment than the PRBM. Both the models give a better prediction of the translational mode than the rotational mode, due to inaccurate modelling of the end-effector. Both models give a prediction closer to the experiment when K_{FEA} is used.

8.5.2.4 The second prototype 3RRR compliant mechanism

Figure 8-44 shows the averaged displacement magnitude versus frequency response for all scan points in the x-axis of the 3RRR compliant mechanism. The frequencies corresponding to the natural frequencies are highlighted on the plots.

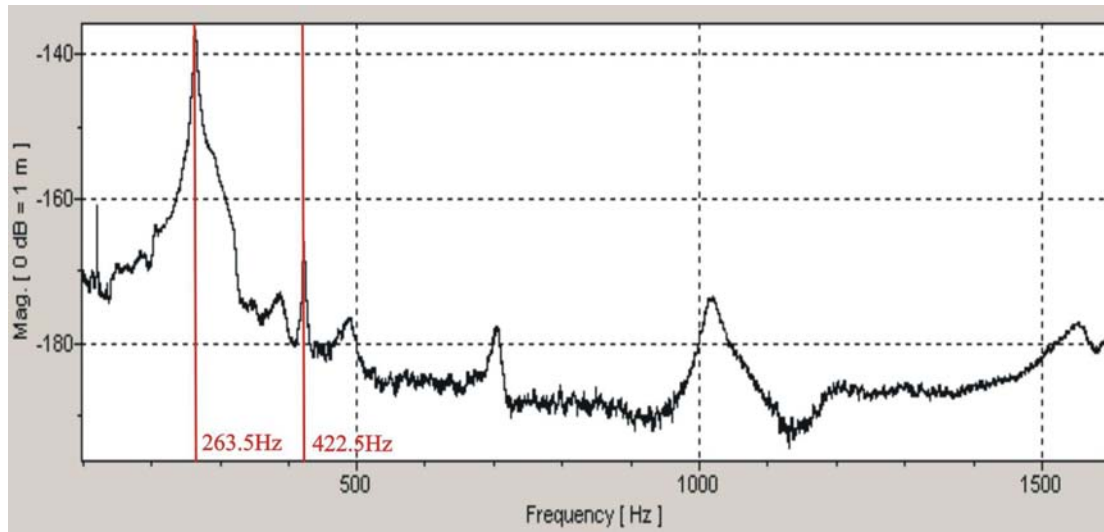


Figure 8-44 - Plot of displacement magnitude (dB) vs. frequency for the second prototype 3RRR compliant mechanism.

Figures 8-45 to 8-46 show sequences from the animation of the operational deflection patterns corresponding to the modes of vibration for the 3RRR compliant mechanism. These clearly identify the translational and rotational modes.

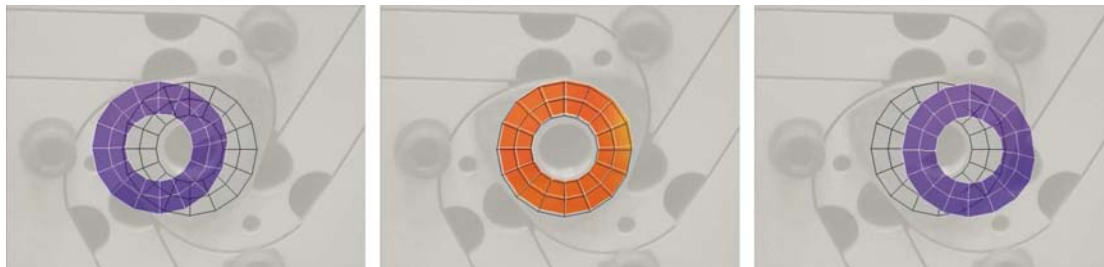


Figure 8-45 - Sequence from animation generated by PSVSoft, of the operational deflection patterns corresponding to the first translational mode, 263.5 Hz, for the second prototype 3RRR compliant mechanism.

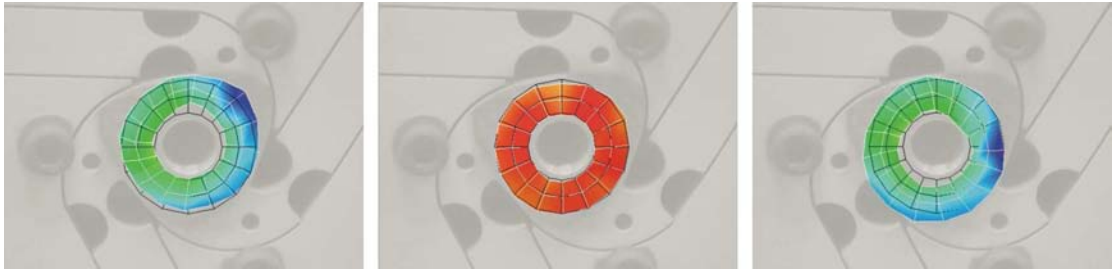


Figure 8-46 - Sequence from animation generated by PSVSoft, of the operational deflection patterns corresponding to the first rotational mode, 422.5Hz, for the second prototype 3RRR compliant mechanism.

8.5.2.5 The second prototype $XY\theta_z$ stage

Figure 8-47 shows the displacement magnitude frequency response for the average of the scan points in the x-axis of the $XY\theta_z$ stage. The frequencies corresponding to the natural frequencies are highlighted on the plots.

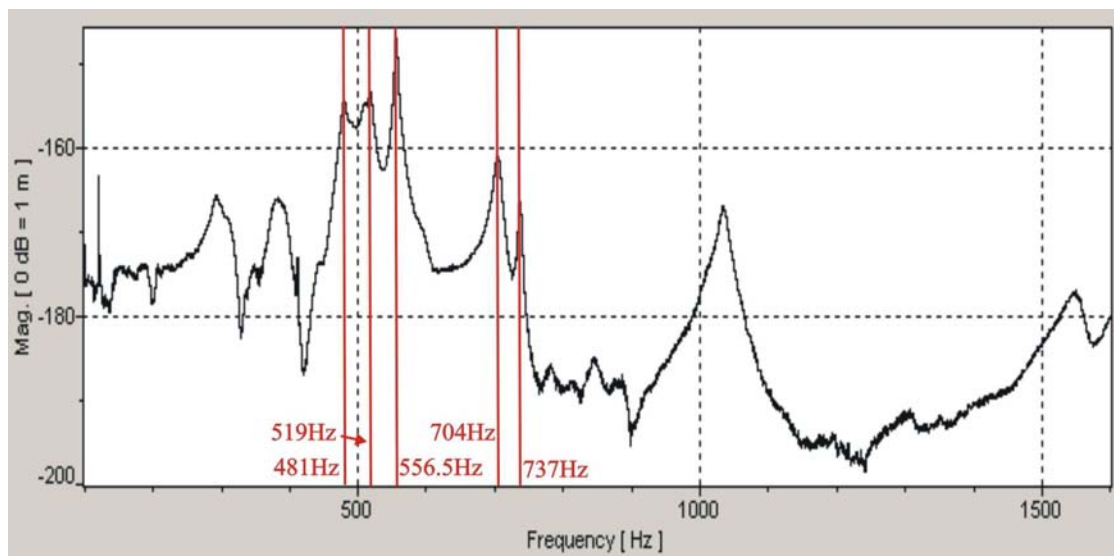


Figure 8-47 - Plot of displacement magnitude (dB) vs. frequency for the second prototype $XY\theta_z$ micro-motion stage.

Figures 8-48 to 8-52 show sequences from the animation of the operational deflection patterns corresponding to the modes of vibration for the $XY\theta_z$ stage. These clearly identify the translational and rotational modes.

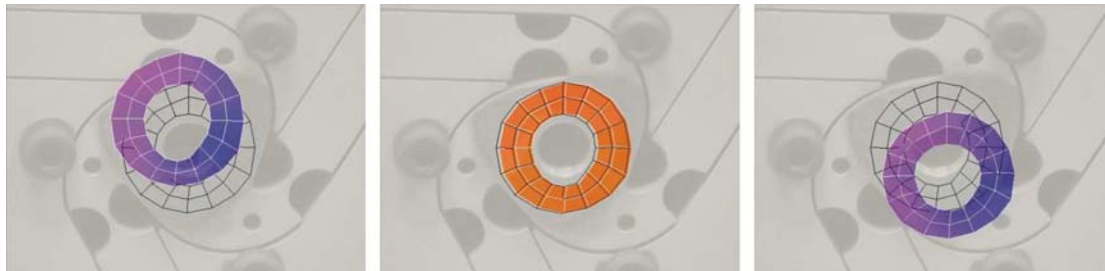


Figure 8-48 - Sequence from animation generated by PSVSoft, of the operational deflection patterns corresponding to the first translational mode, 481Hz, for the second prototype $XY\theta_z$ stage.

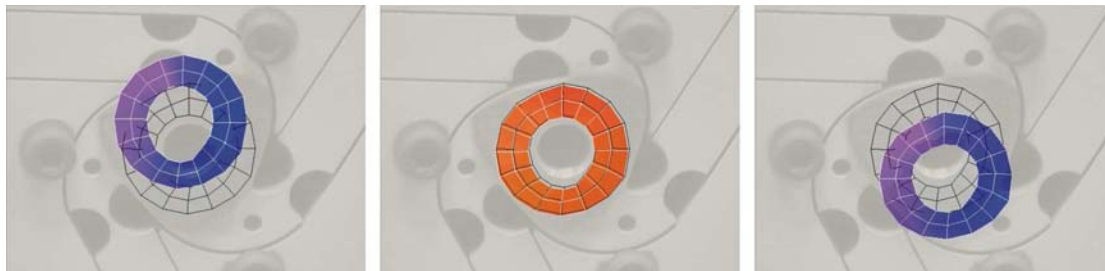


Figure 8-49 - Sequence from animation generated by PSVSoft, of the operational deflection patterns corresponding to the second translational mode, 519Hz, for the second prototype $XY\theta_z$ stage

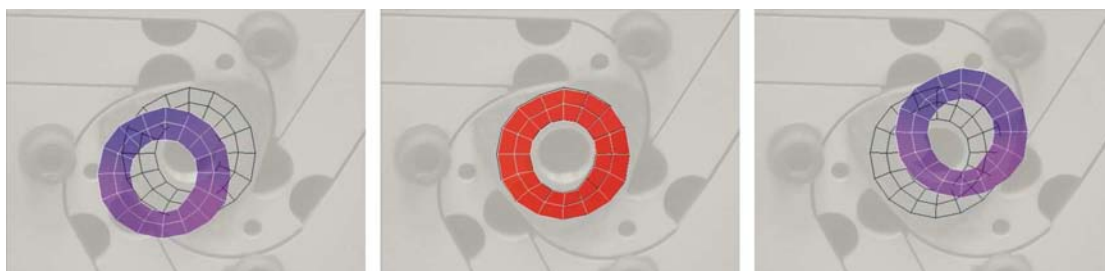


Figure 8-50 - Sequence from animation generated by PSVSoft, of the operational deflection patterns corresponding to the third translational mode, 556.5Hz, for the second prototype $XY\theta_z$ stage

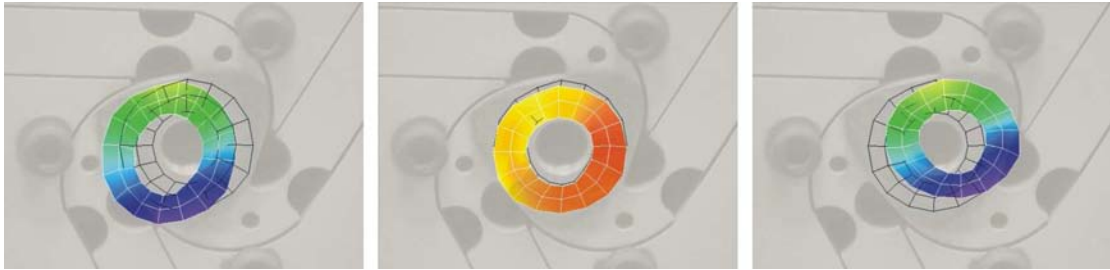


Figure 8-51 - Sequence from animation generated by PSVSoft, of the operational deflection patterns corresponding to the first rotational mode, 704Hz, for the second prototype $XY\theta_z$ stage

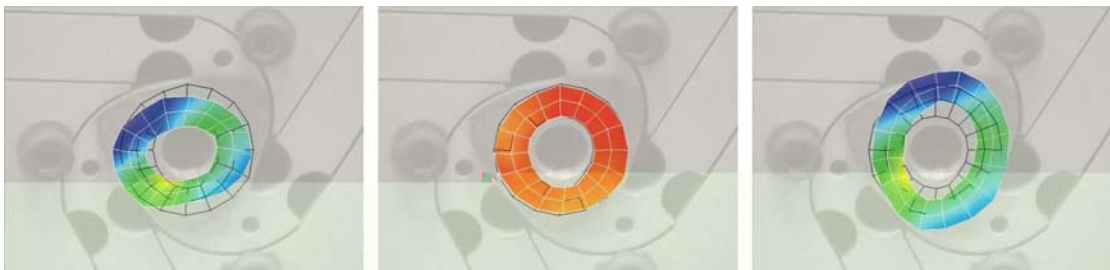


Figure 8-52 - Sequence from animation generated by PSVSoft, of the operational deflection patterns corresponding to the second rotational mode, 737Hz, for the second prototype $XY\theta_z$ stage

All the natural frequencies are tabulated in Table 8-10 and a comparison is given with the natural frequency prediction given by the 2-D FEM, SCHM and PRBM.

Natural Frequencies of 3RRR Compliant Mechanism											
Mode	Exp	2-D FEM		SCHM				PRBM			
			%	$K_{Analytical}$		K_{FEA}		$K_{Analytical}$		K_{FEA}	
	ω_n	ω_n	error	ω_n	error	ω_n	error	ω_n	error	ω_n	error
1st Translation	263.5	260.5	1.2	278.7	-5.8	256.8	2.5	281.6	-6.9	258.6	1.9
1st Rotation	422.5	426.9	-1.0	475.9	-12.6	448.8	-6.2	478.0	-13.1	450.0	-6.5
Natural Frequencies of $XY\theta_z$ Stage											
Mode	Exp	2-D FEM		SCHM				PRBM			
			%	$K_{Analytical}$		K_{FEA}		$K_{Analytical}$		K_{FEA}	
	ω_n	ω_n	error	ω_n	error	ω_n	error	ω_n	error	ω_n	error
1st Translation	481.0										
2nd Translation	519.0	630.1	-21.4	641.0	-23.5	633.1	-22.0	896.6	-72.8	889.9	-71.5
3rd Translation	556.5	656.5	-18.0	665.1	-19.5	657.6	-18.2	944.0	-69.6	937.6	-68.5
1st Rotation	704.0										
2nd Rotation	737.0	865.9	-17.5	955.7	-29.7	943.8	-28.1	1294.4	-75.6	1284.7	-74.3

Table 8-10 - Natural frequencies for the second prototype 3RRR compliant mechanism and $XY\theta_z$ stage given by the experiment, 2-D FEM, SCHM and PRBM.

8.5.2.6 Discussion

Two natural frequencies can clearly be identified for the 3RRR compliant mechanism from Figure 8-44, while four natural frequencies can be identified for the $XY\theta_Z$ stage from Figure 8-47. Comparing these two figures it can be seen that the two peaks at approximately 120Hz and 1050Hz occur in both plots, indicating that these frequencies correspond to rigid-body vibrations of the support structure, or harmonics in the shaker.

From the experimental result shown in Figure 8-45 it can be seen that for the 3RRR compliant mechanism one translational mode is excited in the x-direction, the direction of force application. The 2-D FEM gives a prediction very close to the experiment. The SCHM and PRBM of the 3RRR compliant mechanism give very similar predictions and are close to the experiment when K_{FEA} is used.

From the experiment result shown in Figure 8-46 the rotational mode can clearly be seen. It should be pointed out that this is a purely rotational mode with no translational motion. The 2-D FEM prediction for the rotational mode of the 3RRR compliant mechanism is very close to the experimental result. The SCHM and PRBM predictions again give very similar results and are much more accurate when K_{FEA} is used. The rotational mode prediction given by the SCHM and PRBM is not as accurate as the translational mode prediction, due to the inaccurate modelling of the end-effector.

The modes of the $XY\theta_Z$ stage are very different to the 3RRR compliant mechanism. Rather than one translational and one rotational mode, there are three translational and two rotational modes. All modes occur at higher frequencies than the 3RRR compliant mechanism modes. From Figures 8-48 to 8-50 it can be seen that the translational modes all occur in different directions to the direction of excitation. From Figure 8-51 it can be seen that the first rotational mode also experiences significant translational motion. An explanation for these results is that the piezo-actuators cause the stage to have asymmetric stiffness. Therefore unexpected vibrational modes are introduced.

The models all predict that the $XY\theta_Z$ stage modes occur at significantly higher frequencies than given by the experimental results. This suggests that either the piezo-actuator model is inaccurate, or that the un-modelled preload compliance has a significant effect.

As discussed in Chapter 7, the models of the $XY\theta_Z$ stage give two translational modes, at different frequencies. This is due to the asymmetry caused by the manufacturing error, which causes one piezo-actuator to be positioned differently to the others. The 2-D FEM gives the predictions for both translational and rotational natural frequencies closest to the experiment. The SCHM gives predictions for the translational modes similar to the 2-D FEM, particularly when K_{FEA} is used. The SCHM prediction for the rotational mode is significantly less accurate than the 2-D FEM. The PRBM gives very different predictions to both the 2-D FEM and SCHM for translational and rotational natural frequencies.

8.5.3 Experimental procedure to determine the static-coupling

Static-coupling was discussed in Chapter 4. It describes the interference between actuators caused by the transmission of forces through the mechanism from one input-link to another. To experimentally determine the static-coupling, an input voltage was applied to piezo-actuator 2 so that it applied the input force, F_{in} , to the compliant mechanism input-link. Piezo-actuator 2 was driven through its maximum range and the input-link displacements ΔD_2 , ΔD_1 and ΔD_3 were recorded. From this data static-coupling 1/2 and static-coupling 2/3 can be determined using equations (8.7) and (8.8).

$$\text{Static-coupling } 1/2 = \Delta D_1 / \Delta D_2 \quad (8.7)$$

$$\text{Static-coupling } 3/2 = \Delta D_3 / \Delta D_2 \quad (8.8)$$

The static-coupling was determined for both the 3RRR compliant mechanism and the $XY\theta_z$ micro-motion stage. A different procedure was used to record the displacements for each case. The experimental static-coupling was then compared to the static-coupling predicted by the 2-D FEM, SCHM and PRBM.

8.5.3.1 3RRR compliant mechanism

Piezo-actuator 2 was the only piezo-actuator to be in contact with the compliant mechanism, by tightening the preload mechanism. The other piezo-actuators had their preload mechanisms released so that they were not in contact with the compliant mechanism. The displacement of input-link 2, ΔD_2 , was measured using

the strain gauges bonded to piezo-actuator 2. The displacement of input-link 1, ΔD_1 and input-link 3, ΔD_3 , was measured using the fibre-optic sensor using the same approach used for the strain gauge calibration, as discussed in section 8.3.4.

8.5.3.2 XY θ_z micro-motion stage

All three piezo-actuators were in contact with the compliant mechanism, by tightening their preload mechanisms. The displacement of all the input-links ΔD_1 , ΔD_2 and ΔD_3 , was measured using the strain gauges bonded to piezo-actuator 1, 2 and 3, respectively. These strain-gauges had been calibrated using the calibration procedure discussed previously.

8.5.3.3 Static-coupling results

8.5.3.4 The first prototype

Plots of displacements ΔD_1 , ΔD_2 and ΔD_3 , and static-coupling 1/2 and static-coupling 3/2 are given in Figure 8-53. The mean static-coupling was calculated for each case and is given in Table 8-11. The experimental coupling can be compared to the coupling predicted by the 2-D FEM, SCHM and PRBM which is also given in Table 8-11.

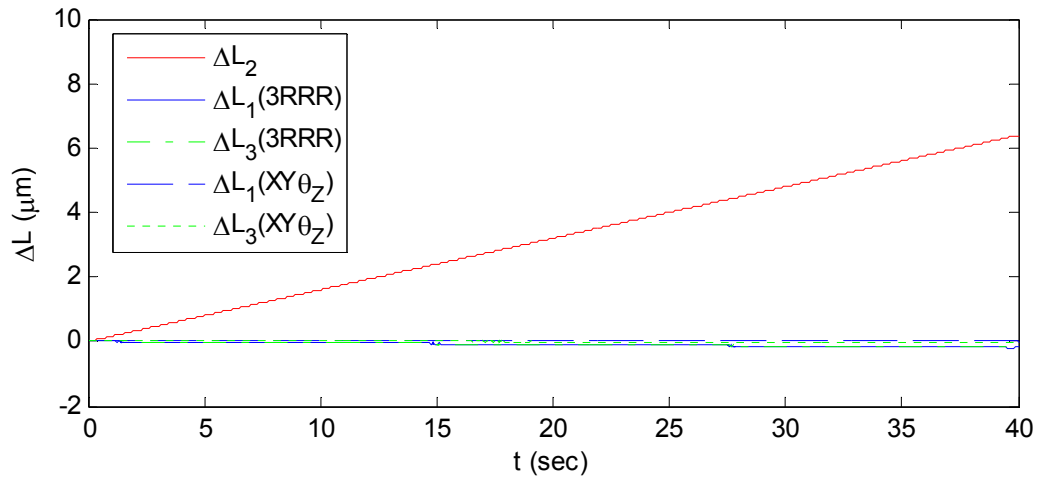


Figure 8-53 - Plots of ΔD_1 , and ΔD_3 generated due to coupling when an input displacement is applied by ΔD_2 .

3RRR compliant mechanism	Experiment	2-D FEM	SCHM	PRBM
Static-coupling 2/1	-0.031	-0.010	-0.010	-0.024
Static-coupling 2/3	-0.030	-0.010	-0.010	-0.024
XYθ_z micro-motion stage	Experiment	2-D FEM	SCHM	PRBM
Static-coupling 2/1	-0.0015	-0.002	-0.003	-0.009
Static-coupling 2/3	-0.0035	-0.002	-0.003	-0.009

Table 8-11 - Static-coupling of the first prototype 3RRR compliant mechanism and XYθ_z stage.

8.5.3.5 Discussion

From Table 8-11 it can be seen that the experimental results and model predictions for the static-coupling of the 3RRR compliant mechanism and XYθ_z stage are of the same sign and order. For the 3RRR compliant mechanism, the experiment results show coupling 2/1 and coupling 3/1 to be almost identical, as expected. The PRBM gives a prediction of 3RRR compliant mechanism coupling closer to the experiment than the other two models. This is unexpected. For the XYθ_z stage the experiment results show coupling 2/1 and coupling 3/1 to be different. This is unexpected as well

and likely to be due to uneven adjustment of the preload. The 2-D FEM or SCHM give the prediction of $XY\theta_Z$ stage coupling closest to the experiment, depending on which coupling is considered.

8.5.3.6 The second prototype

Plots of displacements ΔD_1 , ΔD_2 and ΔD_3 , and static-coupling 1/2 and static-coupling 3/2 are given in Figure 8-54. The mean static-coupling was calculated for each case and is given in Table 8-12. The experimental coupling can be compared to the coupling predicted by the 2-D FEM, SCHM and PRBM which is also given in Table 8-12.

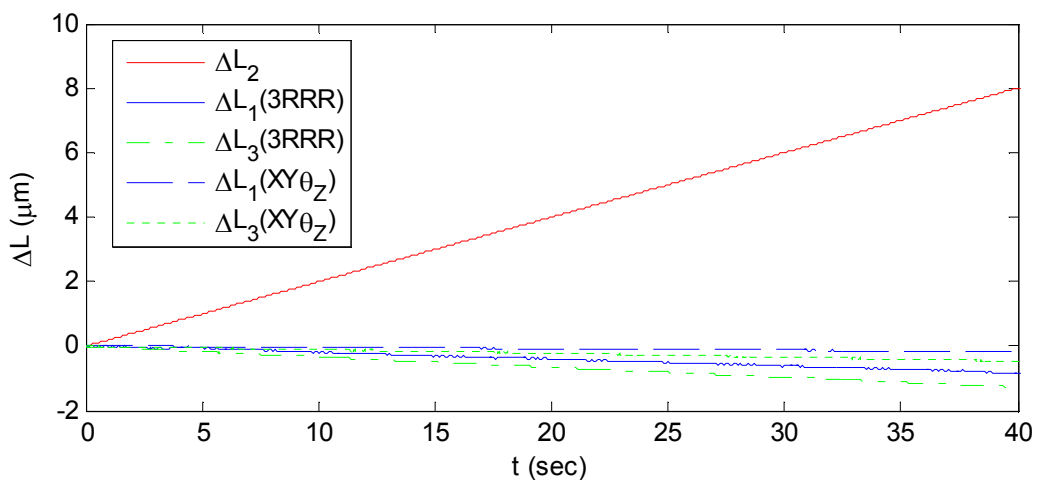


Figure 8-54 - Plots of ΔD_1 , and ΔD_3 generated due to coupling when an input displacement is applied by ΔD_2 .

3RRR compliant mechanism	Experiment	2-D FEM	SCHM	PRBM
Static-coupling 2/1	-0.103	-0.154	-0.154	-0.169
Static-coupling 2/3	-0.158	-0.142	-0.141	-0.154
XYθ_z micro-motion stage	Experiment	2-D FEM	SCHM	PRBM
Static-coupling 2/1	-0.022	-0.015	-0.012	-0.016
Static-coupling 2/3	-0.056	-0.014	-0.013	-0.018

Table 8-12 – Static-coupling of the second prototype 3RRR compliant mechanism and XY θ_z Micro-Motion Stage.

8.5.3.7 Discussion

From Table 8-12 it can be seen that the experimental results and model predictions for the static-coupling of the 3RRR compliant mechanism and XY θ_z stage, are of the same sign and order. For both the 3RRR compliant mechanism and XY θ_z stage, the experiment results show coupling 1/2 and coupling 3/2 to be different. This is expected, due to the manufacturing error causing the piezo-actuator locations to be different. However, the models all predict that coupling 1/2 should be greater than coupling 3/2, where as the experimental results show coupling 3/2 to be greater than coupling 1/2. In addition, the experimental couplings differ by a greater amount than the model predictions. The PRBM gives a prediction of 3RRR compliant mechanism and XY θ_z stage coupling closer to the experiment than the other two models, which is also unexpected. The reason for these discrepancies is not clear; although it is likely they could be due to errors in the experimental results. The calibration using the fibre-optic sensor introduces non-linearity, as mentioned in section 8.4.3.1, which may have a significant impact when measuring the small displacements generated by the static-coupling. Further investigation of the problem is needed.

Chapter

9 Conclusions and Future Work

This chapter summarises the work presented in this thesis, highlights the contributions to the current knowledge and presents suggestions for future work.

9.1 Aims of this study

This study had two broad aims. Firstly, the study aimed to thoroughly investigate methods to model the 3RRR compliant mechanism and the $XY\theta_Z$ micro-motion stage, consisting of compliant mechanism and piezo-actuators. The intention was to determine how accurately each model could predict the kinematic and dynamic behaviour of the $XY\theta_Z$ stage so that appropriate modelling methods could be clearly identified. The models were also to be compared on a basis of computational efficiency so that the modelling method most suited to parametric study and optimisation could be determined.

The second aim of this study was to use the most appropriate model in parametric study and optimisation. The parametric study intended to identify the relationship between stage parameters and output characteristics, so that the design space of the stage could be better understood. The parametric study was conducted using a number of different models, so that the differences between them could be identified. The knowledge gained in the parametric study could then be used to aid the optimal design process. An $XY\theta_Z$ stage was required for an application in a Scanning Electron Microscope (SEM) and the optimal design process was to be used to design an appropriate 3RRR compliant mechanism to be used in this $XY\theta_Z$ stage.

Theoretical work presented was to be validated by experimental results.

9.2 Summary of the work presented in this thesis

A thorough review of the current literature was conducted. This gave an overview of micro-motion stages using compliant mechanisms with flexure hinges and identified the methods that have been developed to model compliant mechanisms. Previous stages using the 3RRR compliant mechanism were highlighted and the advantages of this topology of compliant mechanism was outlined. The modelling of piezo-actuators was also discussed and the interaction between the piezo-actuator and compliant mechanism was highlighted. Several micro-motion stage models that have incorporated the piezo-actuator model were identified and discussed. The optimisation of micro-motion stages was then discussed. This review identified gaps in the current knowledge to be investigated in this study. It was found that only three different designs of 3RRR (or similar) compliant mechanism had been used in micro-

motion stage designs. In the design of these compliant mechanisms several modelling methods had been applied, but no study had been conducted to compare these methods. None of these models had included the piezo-actuator. A parametric study or optimal design procedure had not been conducted for the 3RRR compliant mechanism, although Ryu (1997) had used optimisation techniques in designing a similar mechanism. Therefore, the relationship between mechanism parameters and output characteristics of a stage using the 3RRR compliant mechanism was not understood.

In this thesis three compliant mechanism modelling methods were presented. Firstly, a linear analytical method was presented to derive the Pseudo-Rigid-Body-Model (PRBM) of the 3RRR compliant mechanism. Secondly, 2-D Finite-Element-Model (FEM) was presented. Thirdly, a numerical method, using analytical equations to predict the planar degrees-of-freedom compliance of the flexure hinges, was presented. This was termed the Simple-Compliant-Hinge-Model (SCHM). The 2-D FEM, SCHM and PRBM were used to model a single flexure hinge, a four-bar linkage and a 3RRR compliant mechanism. The stiffnesses of a number of single flexure hinges, predicted by the models, were compared. The stiffness and natural frequency of the four-bar linkage, predicted by the models was compared, and a comparison was also given with the four-bar linkage models presented by Ryu (1997). The 2-D FEM, SCHM and PRBM of a 3RRR compliant mechanism were then compared, taking consideration of the Jacobian, input stiffness, natural frequencies and static-coupling. The translational and rotational modes of vibration

were clearly identified, and the static-coupling was defined. The computational efficiency of the 3RRR compliant mechanism models were also compared.

A linear piezo-actuator model was then incorporated into the 3RRR compliant mechanism models to give more complete $XY\theta_Z$ stage models. These models were then used to investigate the workspace area of the $XY\theta_Z$ stage. The reachable and maximum constant-orientation workspace areas were identified and clearly described. The workspace areas predicted by the 2-D FEM, SCHM and PRBM were then compared. The natural frequency and static-coupling of the $XY\theta_Z$ stage predicted by the models was also compared.

The SCHM and PRBM of the 3RRR compliant mechanism, and a SCHM of the $XY\theta_Z$ stage were used in a parametric study, which considered all geometric, link and flexure hinge parameters. The output characteristics considered in this study were reachable workspace width, maximum end-effector rotation, natural frequency and static-coupling. The results of this study provided guidelines to assist with the optimal design. The results also highlight the different trends predicted by the different models.

An optimal design approach was then outlined and applied, using the SCHM of the $XY\theta_Z$ stage. The stage was designed to be used in a SEM and needed to satisfy a number of size constraints, while the desired natural frequency and static-coupling imposed further constraints. The objective set was to maximise the constant-orientation workspace. A prototype of the optimal stage design was then manufactured. This satisfied the size constraints and fitted nicely into the SEM.

However, a manufacturing error was found that caused the performance of the stage to be sub-optimal. The SCHM model of the prototype stage design was then compared to a 2-D FEM and a PRBM.

Experiments were carried out to determine the kinematic and dynamic characteristics of both of the prototype $XY\theta_Z$ stages. The results were used to validate the model results.

9.3 Results

From the study of the single-flexure hinges it was found that the SCHM predictions differ significantly from the 2-D FEM depending on the hinge geometry. It is suggested that this difference is due to the limited accuracy of the analytical equations. These results highlight that the accuracy of the SCHM and PRBM of the compliant mechanisms is limited by the accuracy of the analytical equations. However, detailed experimental comparison is needed to demonstrate how accurate the 2-D FEM and the analytical equations really are.

The SCHM and the 2-D FEM of the four-bar linkage give very similar results for stiffness in the x-axis if the FEA determined stiffness terms, K_{FEA} , are used. If the analytical equations, $K_{analytical}$, are used the stiffness differs to the 2-D FEM by a similar amount to the difference between the $K_{analytical}$ and K_{FEA} of the single flexure hinge. The stiffness predicted by the models of the four-bar linkage in the y-axis is significantly different regardless of the stiffness terms used, which is thought to be

due to different predictions of the link compliance. The PRBM prediction is further from the 2-D FEM than the SCHM. The SCHM gives very similar results to Ryu's method [Ryu, 1997], if the links are modelled as rigid.

Comparing the models of the two 3RRR compliant mechanism prototypes several observations can be made. The experimental results demonstrated that the 2-D FEM gives predictions of the kinematics and natural frequency that are very close to the experiment result, and are the most accurate of the three models. This verifies that the 2-D FEM is a suitable benchmark for comparison of the other models. For both prototypes the SCHM gives predictions of the kinematic characteristics that are close to the experimental results, which verifies the usefulness and reliability of the SCHM. The PRBM gives predictions of the kinematic characteristics furthest from the experiment results, and can be very inaccurate depending on the particular configuration of the mechanism. However, for both prototypes the PRBM and SCHM give a similar prediction of the natural frequency, which is close to the experimental results if K_{FEA} is used.

The accuracy of the static-coupling predictions is harder to confirm, due to the likelihood of errors in the experimental results.

Comparing the computational efficiency of the 2-D FEM, SCHM and PRBM it was found that the SCHM and PRBM can be built, meshed and solved in approximately $1/9^{\text{th}}$ of the time for the 2-D FEM. Therefore, the SCHM and PRBM are far more computationally efficient.

The $XY\theta_Z$ stage models give predictions of both the kinematic and dynamic behaviour that is significantly different to the 3RRR compliant mechanism models. This shows the importance of including the piezo-actuator model. The experimental results for the workspace width, natural frequency and static-coupling of the $XY\theta_Z$ stages demonstrates the same trends predicted by the models, but the results differ very significantly to the predictions given by the models. The 2-D FEM and the SCHM give very similar results, while the PRBM gives significantly different results.

The results of the parametric study highlight several important points. Firstly, the PRBM and SCHM of the 3RRR compliant mechanism predict different trends in the kinematic behaviour. As the SCHM has been demonstrated to give more reliable accuracy than the PRBM, this suggests that the SCHM should be used in parametric studies and optimisation, rather than the PRBM, which will not give reliable results. Secondly, the SCHMs of the 3RRR compliant mechanism and $XY\theta_Z$ stage, predicted similar trends, but gave different values for the output characteristics. This suggests that if the $XY\theta_Z$ stage design must meet specific constraints or objectives, then the 3RRR compliant mechanism model alone will not give an adequate prediction to ensure a suitable design. The $XY\theta_Z$ stage model should be used in preference.

The parametric study also demonstrated numerous trends that may help the stage designer to develop a design, or help to simplify the optimisation process.

The SCHM model was used in the optimal design, to give a computationally efficient solution, and the parameter values were constrained using information from the parametric study. This allowed for fast convergence to an optimal design. The optimally designed prototype was then demonstrated to meet all the size constraints, provide the desired performance requirements and deliver a relatively large maximum constant-rotation workspace.

9.4 Conclusions

The important conclusions that can be drawn from these results are that:

- The 2-D FEM gives reliable and accurate predictions of both kinematic and dynamic behaviour of the 3RRR compliant mechanism, and is therefore an appropriate benchmark for comparison with the other models.
- The SCHM is less accurate than the 2-D FEM, but can still give reliable and reasonably accurate predictions of the kinematic and dynamic behaviour of the 3RRR compliant mechanism.
- Due to its relative accuracy and computational efficiency the SCHM is well suited for use in parametric study and optimal design of the 3RRR compliant mechanism.
- The PRBM cannot be relied upon to give accurate predictions of the kinematic behaviour, for all configurations of 3RRR compliant mechanism. However, it can give relatively accurate predictions of the natural frequency.

- The kinematic behaviour trends predicted by the PRBM in the parametric study differ significantly to those predicted by the SCHM. Therefore, it is not suited for use in parametric study or optimisation, if kinematic characteristics are of concern.
- The accuracy of both the SCHM and PRBM depends on the accuracy of the analytical equations used to determine the flexure hinge stiffness.
- The piezo-actuator model should be included to give a more accurate $XY\theta_Z$ stage model as it has a very significant effect on the stage performance. However, the modelling of the piezo-actuator needs to be implemented carefully to give useful results.
- To satisfy specific constraints and requirements of the $XY\theta_Z$ stage the parametric study and optimisation should use a complete $XY\theta_Z$ stage model.
- The parametric study has given some understanding of how the 3RRR compliant mechanism parameters affect the output performance of the $XY\theta_Z$ stage.
- The optimal design process has been demonstrated to work effectively.

9.5 Contributions to current knowledge

The work presented in this thesis has made several contributions to the current knowledge:

- A method was presented to derive a linear analytical pseudo-rigid-body-model of the 3RRR compliant mechanism.
- A method was presented to construct a computationally simple, yet relatively accurate, 3RRR compliant mechanism model in ANSYS. This model represents the flexure hinges as multi-degree-of-freedom joints with stiffness determined using commonly used analytical equations. This method of construction could be applied to any planar compliant mechanism.
- This work has given a clear indication of the accuracy and usefulness of three modelling methods, to predict the kinematic and dynamic behaviour of the 3RRR compliant mechanism.
- A method to include the piezo-actuator into the 3RRR compliant mechanism has been presented and its accuracy and usefulness has been demonstrated.
- The static-coupling of the 3RRR compliant mechanism has been discussed in detail and a design approach to reduce this has been presented.

- The workspace of the $XY\theta_Z$ stage using the 3RRR compliant mechanism has been investigated in depth and the different regions of the workspace have been clearly identified.
- A parametric study has been conducted providing new insight to how the 3RRR compliant mechanism parameters affect its output characteristics. This information has been shown to be useful to aid the optimal design of a stage using the 3RRR compliant mechanism.

9.6 Recommendations for future work

The accuracy of the SCHM is limited by the accuracy of the analytical equations used to determine K_b , K_x and K_y . Therefore, the model could be improved by using more accurate equations, or some other method to accurately determine the flexure hinge stiffness.

There is an unexpected result given by the SCHM of the first prototype 3RRR compliant mechanism. The Jacobian given by the SCHM using the FEA stiffness terms differs to the 2-D FEM and experiment more than the Jacobian given by the SCHM using the analytical equations. This is the opposite of what is expected. There may be some small error in either, the FEA used to give the hinge stiffness, or the SCHM. This should be investigated.

The SCHM method could be extended to six degrees-of-freedom so that out-of-plane motions can also be considered. It could then also be applied to spatial mechanisms.

The end-effector could be modelled more accurately in the SCHM and PRBM, particularly for the first prototype case. This would improve the prediction of the rotational mode natural frequency.

The $XY\theta_z$ stage models give predictions further from the experiment than the 3RRR compliant mechanism models. This suggests some problems with the $XY\theta_z$ stage models which need to be further investigated. Possible causes may be un-modelled effects due to uneven preload adjustment or un-modelled compliance introduced by the preload mechanism. Furthermore, the interface between the piezo-actuator and compliant mechanism may need to be modelled differently, perhaps as an un-bonded contact surface or the piezo-actuator model may need to be improved.

The experimental static-coupling differed significantly from the model predictions. It is not clear whether this is due to the models, or to the experiment. Further investigation of this problem is needed.